Multimode vibrational dynamics and orientational effects in fluorescence-encoded infrared spectroscopy. II. Analysis of early-time signals

Lukas Whaley-Mayda,[1] Abhirup Guha,[1] and Andrei Tokmakoff[1, a)]

Department of Chemistry, James Franck Institute, and Institute for Biophysical Dynamics, The University of Chicago, Chicago, Illinois 60637, USA

(Dated: 13 October 2023)

Developing fluorescence-encoded infrared (FEIR) vibrational spectroscopy for single-molecule applications requires a detailed understanding of how the molecular response and external experimental parameters manifest in the detected signals. In the previous paper of this series we introduced a nonlinear response function theory to describe vibrational dynamics, vibronic coupling, and transition dipole orientation in FEIR experiments with ultrashort pulses. In this second paper, we apply the theory to investigate the role of intermode vibrational coherence, the orientation of vibrational and electronic transition dipoles, and the effects of finite pulse durations in experimental measurements. We focus on measurements at early encoding delays—where signal sizes are largest and therefore of most value for single-molecule experiments, but where many of these phenomena are most pronounced and can complicate the appearance of data. We compare experiments on coumarin dyes with finite-pulse response function simulations to explain the time-dependent behavior of FEIR spectra. The role of the orientational response is explored by analyzing polarization-dependent experiments and their ability to resolve relative dipole angles in the molecular frame. This work serves to demonstrate the molecular information content of FEIR experiments, and develop insight and guidelines for their interpretation.

[a)] Author to whom correspondence should be addressed: tokmakoff@uchicago.edu

I. INTRODUCTION

The ability to probe the vibrations of single molecules offers a direct view into chemical structure and interaction free of the averaging inherent in conventional ensemble measurements. While an array of single-molecule vibrational techniques utilizing near-field optical effects have been established to study molecules near metallic surfaces or nanostructures,[1–5] methods that can be applied to bulk environments like free solution have only more recently begun to be developed.[6–8] One such approach is fluorescence-encoded infrared (FEIR) spectroscopy, which encodes vibrational excitation on the ground state into the molecule's fluorescence emission intensity, facilitating single-molecule sensitivity.[9] FEIR experiments employ ultrashort pulses to selectively and sequentially excite the molecule's vibrational and electronic transitions, and are therefore time-resolved measurements sensitive to vibrational dynamics during the inter-pulse delays. A thorough understanding of how these dynamics influence the time-dependence of FEIR experiments is critical for interpreting data and designing measurements to most optimally yield the desired molecular information.

FEIR experiments use a pair of broadband IR pulses separated by delay τ_{IR} to excite the vibrations of interest, followed after a variable encoding delay τ_{enc} by an electronically pre-resonant visible pulse to selectively bring the molecule to its fluorescent excited state. Fourier transformation of the resulting fluorescence intensity along τ_{IR} produces an FEIR vibrational spectrum, which evolves in τ_{enc}. Paper I of this series developed a nonlinear response function description of such three-pulse FEIR experiments, describing how the τ_{enc}-dependence of spectra is governed by contributions from the excited vibrational populations undergoing relaxation as well as from the coherent evolution of superpositions of excited states—i.e. the concerted motion along multiple vibrational coordinates. These coherence contributions are a hallmark of ultrafast experiments with broadband excitation covering multiple transitions, and therefore have the potential to be ubiquitous in FEIR measurements on multimode systems.

The vibrational population response produces intuitive absorptive bands in the spectra, each with magnitude proportional to the squared product of the i^{th} vibration's transition dipole moment μ_{i0} and the Franck-Condon (FC) factor $\langle 0^e | 1_i^g \rangle$ describing its coupling to the $g \rightarrow e$ electronic transition. This magnitude is further scaled by a geometric factor dependent on the relative dipole orientation of the vibrational and electronic transitions, manifesting in experimental polarization dependencies with an anisotropy governed by the second Legendre polynomial of a two-point dipole correlation function—a form common to third-order spectroscopies of coupled transitions, e.g. that of a cross-peak in a two-dimensional (2D) spectrum. On the other hand, the coherent response produces phase-twisted lineshapes connecting pairs of vibrational resonances, with phase evolving during τ_{enc} to produce beating signatures. The amplitude of a coherence pathway depends on the product of the transition dipoles and FC factors for both vibrations, $\mu_{i0}\mu_{j0}\langle 0^e|1_i^g\rangle\langle 0^e|1_j^g\rangle$, and can have positive or negative sign. The orientational factor for a coherence is similarly more complex, depending on the multiple angular variables describing the orientation of the two vibrations relative to the electronic transition, and also has variable sign.

The interference of population and coherence contributions can lead to complicated and non-intuitive spectra, particularly when many vibrational modes are excited, resulting in multiple coherences evolving at different beat frequencies with variably signed amplitudes sensitive to vibronic coupling and dipole orientation. This situation is most pronounced at early encoding delays before the vibrational coherence has dephased. At the same time, the overall signal size is invariably largest at these early delays, as the excited populations have not had time to significantly relax. Therefore, working at early τ_{enc} is likely a practical necessity for single-molecule or otherwise high-sensitivity applications.

In this paper we deal with the encoding-delay and polarization-dependent phenomenology of multimode FEIR signals in the early-time region. Focusing our analysis on early-time signals also limits the influence of more complicated vibrational relaxation behavior, notably intramolecular vibrational energy relaxation (IVR),[10–12] allowing us to apply the simple homogeneous-limit expressions for the response function developed in Paper I. Earlier picosecond IR-UV/Vis double-resonance fluorescence experiments—the conceptual predecessors of FEIR spectroscopy—identified IVR as being responsible for signal generation at long delays, where the encoding step no longer samples the initially excited vibrational levels but rather involves transitions from a “hot” distribution of excitation in lower frequency FC-active modes.[13,14] In FEIR spectra at longer τ_{enc} we observe a re-weighting of band intensities consistent with IVR, although further work is needed to fully understand these effects.[15]

In addition to the dynamic molecular response, the spectral and temporal pulse characteristics can also significantly impact the appearance of data. This is especially true at early times, where convolving the system response with the pulse’s finite temporal profiles has the largest effect on the τ_{enc}-dependent shape of signals, and data from within the pulse overlap region is potentially polluted by misordered light-matter interactions and other undesired contributions. Specifically, the problem of where the largest signal is located along τ_{enc}, which is of obvious interest for achieving the highest detection sensitivity, is highly dependent on both the interference of population and coherence pathways as well as finite-pulse effects. For example, Fig. 1 shows two-pulse FEIR transients measured from a variety of coumarin molecules. As described in Paper I, the two-pulse signal represent the magnitude of the total FEIR spectrum integrated over the vibrational frequency axis at each τ_{enc} value. There are distinct variations in the shape of the signals, including steepness of the rising edge, location of the signal maximum, and character of coherent beating (or apparent lack thereof). Notably, in some cases the signal peaks beyond the extent of the pulse-overlap region, while others peak near $\tau_{\mathrm{enc}} = 0$ ps. Understanding these differences, and to what extent the FEIR spectra are interpretable at their brightest, requires an appreciation of the role played by finite-pulse effects.

Assuming the impulsive limit when modelling ultrafast experiments—i.e. taking the pulses to be infinitely short compared to the system dynamics encoded in the response function—is for the most part a convenience that simplifies the problem, rather than a good physical approximation. Some of the most apparent finite-pulse effects are caused by the pulses' finite spectral bandwidth, which effectively windows the system response in the frequency domain and thereby distorts spectra,[17–21] or their finite duration, which modifies the apparent system dynamics measured in the time domain.[22–25] These two types of effects are in general connected by a Fourier transform relation, and occur simultaneously in a measurement. Perhaps less intuitive are effects involving distortions due to non-constant spectral phase, i.e. when pulses are not transform-limited.[26–28] Another class of artifacts emerges from the presence of "improperly" time-ordered light-matter interactions, most notably occurring when pulses overlap and the desired sequentiality of interaction cannot be enforced. Some examples are the perturbed free-induction decay contribution and "coherence spike" in transient absorption and 2D spectra,[29–32] or various other distortions to absorptive 2D spectra from the spurious mixing of rephasing, non-rephasing, and double-quantum coherence pathways.[20,33–37]

Coherently-detected nonlinear experiments are also often affected by other signal contributions not originating from the response of the system of interest, for example arising instead from the solvent or sample cell substrates. These contributions are usually non-resonant with the incident fields and occur during pulse overlap, where they can overwhelm the desired signal. Some common examples include cross-phase modulation of the probe field,[38] and multi-photon absorption or stimulated Raman scattering from the solvent and/or windows.[39,40] As these processes

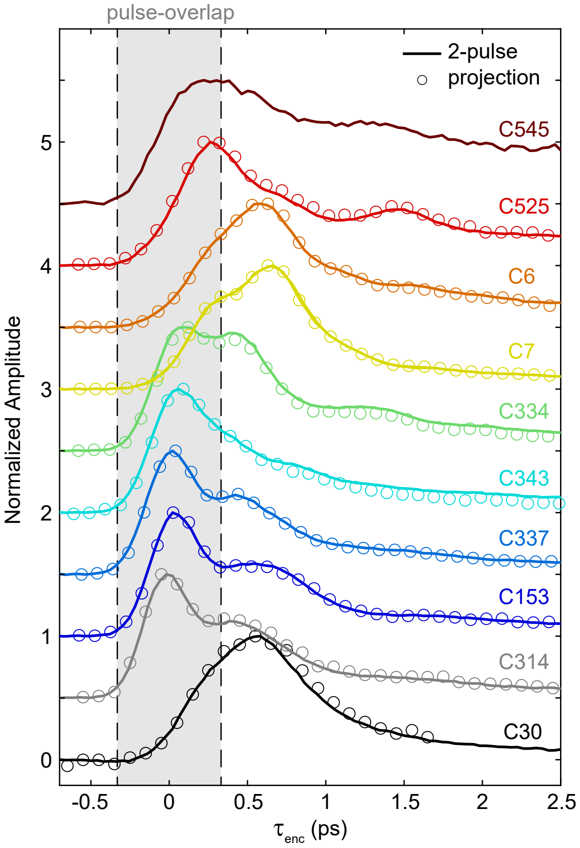

FIG. 1. Two-pulse FEIR signals measured with identical pulse characteristics and *ZZZZ* polarization for 10 coumarin dyes (experiments described in Ref. 16). The independently measured projection of the τ_{enc}-dependent FEIR spectrum onto the τ_{enc}-axis is overlayed to demonstrate the projection-slice relationship (spectra shown in Sec. S6 of the supplementary material). The τ_{enc}-dependent spectrum was not measured for C545. The 1/e^2 full-width (667 fs) of the pulse-overlap region is indicated by the grayed-out box. Traces are normalized to their respective maxima and offset vertically for clarity.

are not described by the response function of the system in question, they present an additional layer of complexity in modelling data within the pulse-overlap region. It is often claimed that action-based techniques, specifically those employing fluorescence detection, are immune to these non-resonant pulse-overlap artifacts because the fluorescence signal comes unambiguously from the spectroscopic system being targeted.[41–45] While this ability to selectively sample the system does preclude many of the pulse-overlap artifacts mentioned above and is an important advantage of fluorescence-detected techniques, it is still possible for undesired processes to influence the system's target excited population—and hence fluorescence signal—during pulse overlap. One important example is multi-photon excitation proceeding through virtual states, i.e. that is non-resonant with the real intermediate system states of spectroscopic interest. In FEIR spectroscopy, vibrationally-nonresonant IR + visible two-photon absorption is an example of such a pulse-overlap artifact that can contribute to early-time data, and will be discussed in our analysis.

Understanding finite-pulse effects is also important for exploring avenues to maximize single-molecule FEIR efficiencies through optimal pulse design. The primary importance of maximizing overall efficiency alters the fundamental strategy in FEIR excitation from that of conventional ultrafast spectroscopies, which typically seek to approach the impulsive limit with the shortest pulses to directly measure the unadulterated system response function. In contrast, an FEIR excitation scheme that optimizes the excitation rate per molecule at the expense of imprinting the pulse characteristics into the data would in principle be desirable, provided that the resulting signal can still be interpreted to reveal the sought after molecule information.

This paper explores the role of vibrational coherence, finite-pulse effects, and orientational response in early-time FEIR signals through a comparison of experimental data with response function simulations. We address bulk experiments on coumarin dyes largely described previously in Ref. 16, and adopt a descriptive approach aimed at cataloging τ_{enc}-dependent behavior and orientational effects through demonstrative calculations. This paper is organized as follows. Section II describes the experimental and computational methods. Section III analyzes many of most important effects of finite pulses through simulations on a model two-mode system. In Sec. IV we analyze the role of vibrational coherence in measurements on coumarin 6 (C6), which have been especially significant for the development of FEIR spectroscopy as they were used for our previous demonstration of single-molecule sensitivity.[9] In these experiments the coumarin ring vibrations being probed have roughly parallel transition dipoles, so the orientational response does not need to be accounted for the model the signals. Section V discusses the polarization-dependence of the FEIR signal, first for the simplest case of a single-mode system given by the spectrally-isolated nitrile stretching mode of coumarin 337 (C337). Then the orientational response of a more complicated multimode system consisting of the high-frequency ring modes and pair of carbonyl stretches of coumarin 343 (C343) is analyzed, and the ability of FEIR anisotropy to measure the relative vibrational transition dipole angles is discussed.

II. METHODOLOGY

A. FEIR experiments and temporal instrument response characterization

The FEIR data analyzed in this paper originates from the experiments described in Ref. 16, with the exception of the C337 nitrile measurements in Sec. V A, and further details on the instrumentation can also be found in Refs. 9 and 15. Here we briefly describe aspects of the experimental methodology relevant to τ_{enc}-dependent measurements. IR pulses are generated by an optical parametric amplifier (OPA) pumped with a 1 MHz repetition-rate Yb fiber laser (Coherent Monaco 1035-40),[46] and sent through a Mach-Zehnder interferometer to produce a collinear pulse-pair with controllable delay τ_{IR}. The visible encoding pulse (ω_{vis} = 19360 cm^{-1} = 516.5 nm) is generated by doubling the fiber laser fundamental and passed through a delay line to set and control the encoding delay τ_{enc}. The linear polarization of the IR pulse out of the OPA is left unadjusted, while the linear polarization of the encoding pulse is rotated by a half-wave plate to control the relative pulse polarization angle Θ (defined in Paper I).

The IR pulse-pair and visible encoding pulse are delivered into a home-built microscope where they are focused into the sample in a collinear, counter-propagating geometry using a $\sim$0.7 numerical aperture (NA) ZnSe aspheric lens and 0.8 NA air objective, respectively. The sample consists of a 1 mm thick $\mathrm{CaF_2}$ window on the IR (bottom) side, a 50 μm solution layer defined by a PTFE spacer, and either a 175 μm glass or 150 μm $\mathrm{CaF_2}$ coverslip on the visible (top) side. Fluorescence is collected by the air objective, separated from the visible encoding beam by appropriate filters, and focused onto a single-photon avalanche photodiode with its small active area serving as a confocal aperture. The probed region of solution is defined by the visible confocal volume, which is contained within the order of magnitude larger IR focus. The total fluorescence intensity is given by a photon count rate corrected for pile-up error, and the FEIR signal is found by subtracting off the constant background from visible excitation alone.[16] A description of how the signal from a three-pulse FEIR experiment is processed into a spectrum is given in Sec. S3.

The IR pulse duration was characterized by interferometric autocorrelation in $\mathrm{AgGaS_2}$ at the sample position (Sec. S5.1). Measurements on C6 and C343 use an IR pulse centered at ω_{IR} = 1620 cm^{-1} with FWHM bandwidth $\Delta\omega_{\mathrm{IR}}$ = 135-140 cm^{-1} and mildly-chirped duration (FWHM intensity profile) of $\tau_{p,\mathrm{IR}}$ = 230 fs (calculated transform-limited duration of 105-110 fs). For measurements on the C337 nitrile the IR pulse is tuned to ω_{IR} = 2235 cm^{-1} with FWHM bandwidth

$\Delta\omega_{\mathrm{IR}}$ = 105 cm^{-1} and duration of $\tau_{p,\mathrm{IR}}$ = 180 fs, which is closer to the transform-limited duration of 140 fs.

The visible pulse duration and temporal instrument response function (IRF) are characterized by measuring the intensity cross-correlation of the IR and visible pulses in the sample. This is achieved by taking advantage of fluorescence excited by vibrationally-nonresonant IR + visible two-photon absorption (TPA), and is described in detail in Secs. S4 and S5.2. The TPA signal maps out the pulse-overlap region in τ_{enc}, and is extended over the IR pulse's spectral profile on the frequency axis of an FEIR spectrum. The visible pulse duration is backed out of the measured IRF duration τ_{cc} with knowledge of the IR pulse duration from the relation $\tau_{cc} = \sqrt{\tau_{p,\mathrm{IR}}^2 + \tau_{p,\mathrm{vis}}^2}$, yielding $\tau_{p,\mathrm{vis}}$ = 315 fs.

The peak of the TPA signal along τ_{enc} formally defines the location of τ_{enc} = 0, and therefore can be used to set timing. Ideally, a fluorescent dye that satisfies the FEIR resonance condition $\omega_{\mathrm{IR}} + \omega_{\mathrm{vis}} = \omega_{eg}$ but has no vibrations within the IR bandwidth is selected for generating a TPA signal to characterize the IRF and set timing for experiments. This procedure is adopted for the C337 nitrile experiments in Sec. V A, using C343 as the non-resonant TPA sample (Sec. S5.2). However, we have so far been unable to find a suitable TPA dye for experiments with ω_{IR} < 1800 cm^{-1}, as C=C ring stretches are ubiquitous in organic dyes. Operationally, we therefore set τ_{enc} = 0 for the FEIR measurements at ω_{IR} = 1620 cm^{-1} with reference to the maximum of the C6 two-pulse signal, which we define to occur at τ_{enc} = 600 fs based on response function calculations discussed below in Sec. IV C.

In practice, the proper assignment of time zero for τ_{enc} is also made difficult by the counter-propagating experimental geometry, which couples the relative timing of the IR and visible pulses to longitudinal position along the optical axis. Therefore τ_{enc} timing is sensitive to the overall index profile of the sample, as this determines the effective pathlengths seen by the IR and visible pulses on their way to the confocal volume. Care must be taken to ensure that the solution index, thickness, and depth of the probe volume below the coverslip are consistent between measurements intended to share common τ_{enc} timing. The uncertainty in timing between different experiments (e.g. the various two-pulse transients in Fig. 1) is $\sim$100 fs, which reflects the repeatability from sample to sample likely dominated by variations in solution-layer thickness.

The FEIR measurements on C6 and C343 were performed in acetonitrile-d3 solution at 100 μM concentration, while those on C337 were performed in dimethylformamide (DMF) solution at 100 μM concentration.

B. Numerical finite-pulse response function calculations

Incorporating the effects of finite pulses into a response function calculation presents two main challenges: (1) accounting for all possible time-orderings of light-matter interactions supported by the (potentially overlapping) pulses at any given set of inter-pulse delays, and (2) evaluating the multiple time-convolution integrals of the pulse electric fields against the response function. Our approach is described in detail in Sec. S1. Briefly, to address the first aspect of the problem we employ a set of pulse-specific interaction time variables introduced by Jonas and co-workers to separate the different time-ordered contributions to the signal.[47] The relatively small number of pathways that contribute under the unique resonance conditions of FEIR spectroscopy greatly simplifies this mixed time-ordering situation during pulse-overlap.

Next, we use a numerical Monte Carlo integration procedure to evaluate the four nested convolution integrals of Eq. 8 in Paper I for computing the target population giving rise to the three-pulse signal $F_{12}(\tau_{\mathrm{IR}}, \tau_{\mathrm{enc}})$. The two-pulse signal is calculated from the same expression by setting τ_{IR} = 0. The calculation employs the rotating wave approximation (RWA), and the response function is expressed in the homogeneous limit with the RWA-conjugate electric field phase factors directly incorporated. The pulse electric fields are initially specified in the frequency domain and their time-domain envelopes are evaluated numerically by FFT. The complex envelope of the three-pulse signal is calculated in a fully-rotating frame with respect to the IR center frequency ω_{IR} to facilitate maximal under-sampling of the τ_{IR} delay. For each combination of inter-pulse delays τ_{IR} and τ_{enc}, N Monte Carlo samples of the four integration variables are drawn from independent Gaussian distributions mimicking the field envelopes. The range of each variable's distribution is truncated at 5 times the envelope FWHM of the field facilitating the interaction. We use $N = 2 \times 10^7$ to 5×10^7 samples, and spectra are calculated by FFT from the complex three-pulse signal with τ_{IR} scanned from 0 to 5 ps in 50 fs steps. Section S3 demonstrates that the C_3 pathways do not survive the convolution integrals, and therefore only the C_1 and C_2 pathways are calculated.

All calculations in the main text use the same pulse characteristics, which are chosen to roughly represent those in the experiments on C6 and C343, and are given Gaussian spectra for simplicity (no calculations are performed to model the C337 nitrile experiment). The visible encoding pulse is centered at ω_{vis} = 19360 cm^{-1} with FWHM of $\Delta\omega_{\mathrm{vis}}$ = 46.7 cm^{-1}, producing a transform-limited pulse duration of $\tau_{p,\mathrm{vis}}$ = 315 fs intended to match the experimentally measured pulse duration. The

IR field is centered at ω_{IR} = 1620 cm^{-1} with FWHM $\Delta\omega_{\mathrm{IR}}$ = 140 cm^{-1}. The resulting transform-limited IR pulse duration is $\tau_{p,\mathrm{IR}}$ = 105 fs, and applying a second-order spectral phase (group delay dispersion) of γ_2 = -7800 fs^2 roughly reproduces the experimental pulse duration of 230 fs (Fig. S23). We use transform-limited pulses in the calculations presented in the main text, but describe the effects of this amount of dispersion, which are relatively minor, in Sec. S12.

C. Electronic structure calculations

Electronic structure calculations on the ground and first excited states were performed with density functional theory (DFT) and time-dependent density functional theory (TD-DFT), respectively. The calculations employed the B3LYP functional with 6-31G(d,p) basis set, and ground and excited state geometry optimization and normal mode analysis were carried out in the Gaussian09 package (Revision B.0124) using a polarizable continuum model to account for the solvent (acetonitrile for C6 and C343, dimethylformamide for C337). Frequency calculations were performed on both optimized geometries to determine the vibrational normal modes. The ground state vibrational transition dipole moments were computed from the derivatives of the molecular dipole moment along the respective ground state normal mode coordinates. The electronic transition dipole moments were computed from single-point energy calculations of the first excited state using TD-DFT on the geometry-optimized ground state.

FC wavefunction overlap integrals were calculated using *FCClasses* (version 2.1) developed by Santoro and co-workers.[48,49] We used *FCClasses* to obtain the dimensionless displacements of the optimized excited state minimum relative to the ground state minimum along the normal mode coordinates, and the Duschinsky matrix to compute the FC factors $\langle 0^e | 1_i^g \rangle$ using the relationships outlined in Ref. 50. This method accounts for displacements, frequency changes, and Duschinsky mixing of the normal modes between the ground and excited states. In this work, the normal mode frequency, transition dipole, and FC factor calculations are used to assign vibrational spectra and obtain parameters for the response function simulations that qualitatively demonstrate how features in experimental FEIR data can be seen to arise from the molecular response. A study of how predictive these electronic structure methods are for quantitative aspects of FEIR signal strength will be presented elsewhere.

III. FINITE-PULSE EFFECTS IN A SIMULATED TWO-MODE SYSTEM

A. Model system

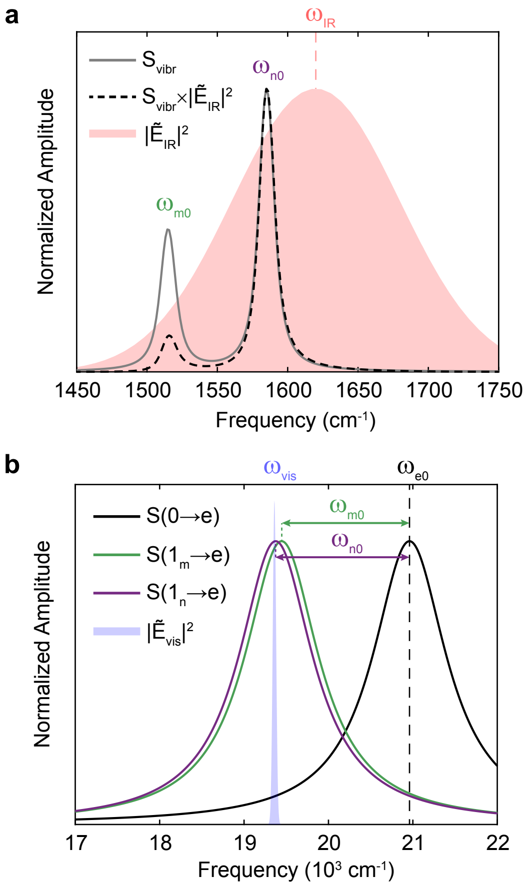

FIG. 2. Spectral characteristics of the two-mode model system and its FEIR resonance conditions. (a) FEIR activity spectrum S_{vibr}, IR pulse spectrum $|\tilde{E}_{\mathrm{IR}}|^2$, and their product. (b) Lineshapes of the encoding transitions $S(1_m \rightarrow e)$ and $S(1_n \rightarrow e)$ for mode m and n, respectively, and the bare 0-0 electronic transition $S(0 \rightarrow e)$. The visible pulse spectrum $|\tilde{E}_{\mathrm{vis}}|^2$ is overlayed.

In this section we examine the impact of finite pulses in the simulated FEIR spectroscopy of a system of two coupled vibrations. Since a two-mode system is the minimal case that exhibits vibrational coherence, this model system captures many of the features common to multimode FEIR experiments. Paper I treated the phenomenology of two-mode FEIR signals in the impulsive limit. Building on that discussion, we demonstrate the most important finite-pulse effects, including the windowing of vibrational spectra by the finite IR bandwidth, the distortion of coherence evolution in τ_{enc}, and the resulting consequences to the interference between population and co-

Mode	ω_{i0} (cm^{-1})	μ_{i0}	$\langle 0^e \vert 1_i^g \rangle$	$\Gamma_{i0}^{-1} = \Gamma_{ii}^{-1}$ (fs)	Γ_{ei}^{-1} (fs)
m	1515	$1/\sqrt{2}$	0.1	1000	10
n	1585	1	0.1	1000	10

TABLE I. Response function parameters for the two-mode model system. The singly-excited vibrational states are indexed by $i = m, n$ and the intermode coherence dephasing is set to Γ_{mn}^{-1} = 500 fs.

herence contributions. We will restrict our analysis to transform-limited pulses. We will ignore the orientational response, which in the limit of slow orientational dynamics only acts to re-weight pathway amplitudes.

Figure 2 depicts the model system and its resonance conditions, which are chosen to reflect a situation commonly encountered in the coumarin experiments where modes differ both in their FEIR activity and coverage by the IR pulse spectrum. Table III A lists the molecular parameters in the response function. The two modes have a frequency difference of 70 cm^{-1}, which produces a coherence period of 476.5 fs. The modes are lifetime broadened with identical linewidths, and we set the FEIR activity, i.e. the squared product of the vibrational transition moment μ_{i0} and FC factor $\langle 0^e|1_i^g\rangle$, of the lower frequency mode m to be half that of mode n. We note that μ_{i0} and $\langle 0^e|1_i^g\rangle$ always appear multiplied together in the response function, and as we are not interested in calculating absolute signal levels, only the relative FEIR activity between modes is meaningful. Therefore, here and in all other calculations the μ_{i0} are defined scaled relative to the largest and the electronic transition moment μ_{eg} is set to unity. The FC factors are set to have the same sign, so the resulting coherence will be positively signed as discussed in Paper I. Figure 2(a) plots the vibronic FEIR activity spectrum S_{vibr}, defined as the linear IR absorption spectrum with each vibrational resonance weighted by the square of its FC factor. This spectrum reflects the FEIR activity of each mode and is formally equivalent to the impulsive FEIR spectrum at τ_{enc} = 0 with all coherence pathways removed. The resulting IR spectral coverage is such that the weaker mode falls in the low-frequency wing of the pulse spectrum. This difference in intensity of the IR spectrum $|\tilde{E}_{\mathrm{IR}}|^2$ over each mode is evident by comparing S_{vibr} with the product $S_{\mathrm{vibr}} \times |\tilde{E}_{\mathrm{IR}}|^2$.

Figure 2(b) shows the lineshapes of the encoding transitions for each mode as well as the bare 0-0 electronic transition for reference, although this latter transition does not play any role in the calculation. The dephasing time of each of these transitions is set to 10 fs, which results in a Lorentzian FWHM of 1062 cm^{-1} that is over an order of magnitude broader than the visible encoding pulse spectrum ($\Delta\omega_{\text{vis}} = 46.7$ cm^{-1}). The resonance conditions are set with respect to the bare electronic transition so that $\omega_{e0} = \omega_{\text{IR}} + \omega_{\text{vis}}$. Given the breadth of the encoding transitions' lineshapes, the difference in their degree of resonance with the visible pulse spectrum is negligible under these conditions.

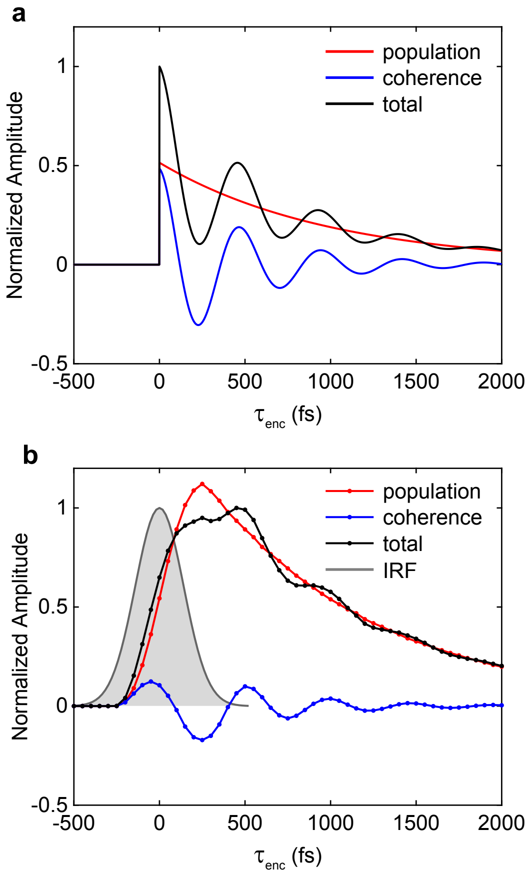

FIG. 3. Two-pulse FEIR signal from the two-mode system in (a) the impulsive limit and (b) with finite pulses. In both cases the total signal (black) is normalized to its maximum value, and the population (red) and coherence (blue) components add up to reproduce the total signal amplitude. The IRF is shown in (b) for reference.

B. Two-pulse signal

We first demonstrate the impact of the finite pulses on the system's two-pulse FEIR signal. Figure 3(a) shows the total signal as well as its decomposition into population and coherence contributions in the impulsive limit. The coherence dephasing time has been set at Γ_{mn}^{-1} = 500 fs, and the positively-signed coherence leads to constructive interference with the population contribution at τ_{enc} = 0 fs. Figure 3(b) shows the same signal and its population and coherence components from the finite-pulse calculation. The IRF with duration $\tau_{cc} = \sqrt{\tau_{p,\text{IR}}^2 + \tau_{p,\text{vis}}^2}$ = 332 fs is shown for reference. Perhaps the most apparent effect of the finite pulses is to reduce the amplitude of the coherence pathways relative to the population pathways, leading to a strong suppression of the beating in the total signal. This can be understood by considering the finite duration of the IRF as a low-pass convolution filter which preferentially washes away the high-frequency variations along τ_{enc}.[51] This suppression is particularly strong over the first half-cycle of the coherence phase occurring during pulse overlap. The result of the interference from the weakened coherence pathways is that the total signal peaks with the first recurrence of the coherence phase at $\tau_{\text{enc}} \sim 500$ fs, which is well beyond the decay of the IRF.

C. FEIR spectrum

Next, we analyze the effects of finite pulses on the FEIR spectrum, and particularly its evolution in τ_{enc}. Figure 4 compares the impulsive and finite-pulse τ_{enc}-dependent FEIR spectra and their respective population and coherence contributions. Starting with the impulsive limit, we note that the smaller FEIR activity of mode m leads to a slightly deeper relative coherent modulation over ω_{m0} compared to ω_{n0}, as can be seen in Figs. 4(a) and (g). This occurs because, whereas the population response of each mode is determined by its FEIR activity (Fig. 4(b)), the coherent response is determined by the "mixed" activity $\mu_{m0}\mu_{n0}\langle 0^e|1_m^g\rangle\langle 0^e|1_n^g\rangle$ and is therefore always equal over both resonances (Fig. 4(c)). The total spectrum at ω_{m0} correspondingly has a larger fractional coherence contribution than at ω_{n0}, and therefore a more pronounced modulation.

With finite pulses the reduction in amplitude of the coherence contribution seen in the two-pulse signal is also strongly apparent in the spectra (note the additional $\times 3$ scaling in Fig. 4(f)), as required by the projection-slice relation. However, the manner in which the coherence and population amplitudes are modified along the vibrational frequency axis are importantly different. Namely, a comparison of Figs. 4(e) and (b) shows that the mode m population feature is suppressed relative to that of mode n due to the lower IR spectral intensity at its location in the wing of the pulse spectrum. However, the amplitudes of the coherence pathways are still equal over both modes outside of the pulse overlap region (cf. Figs. 4(f) and (c)). The result is that the frac-

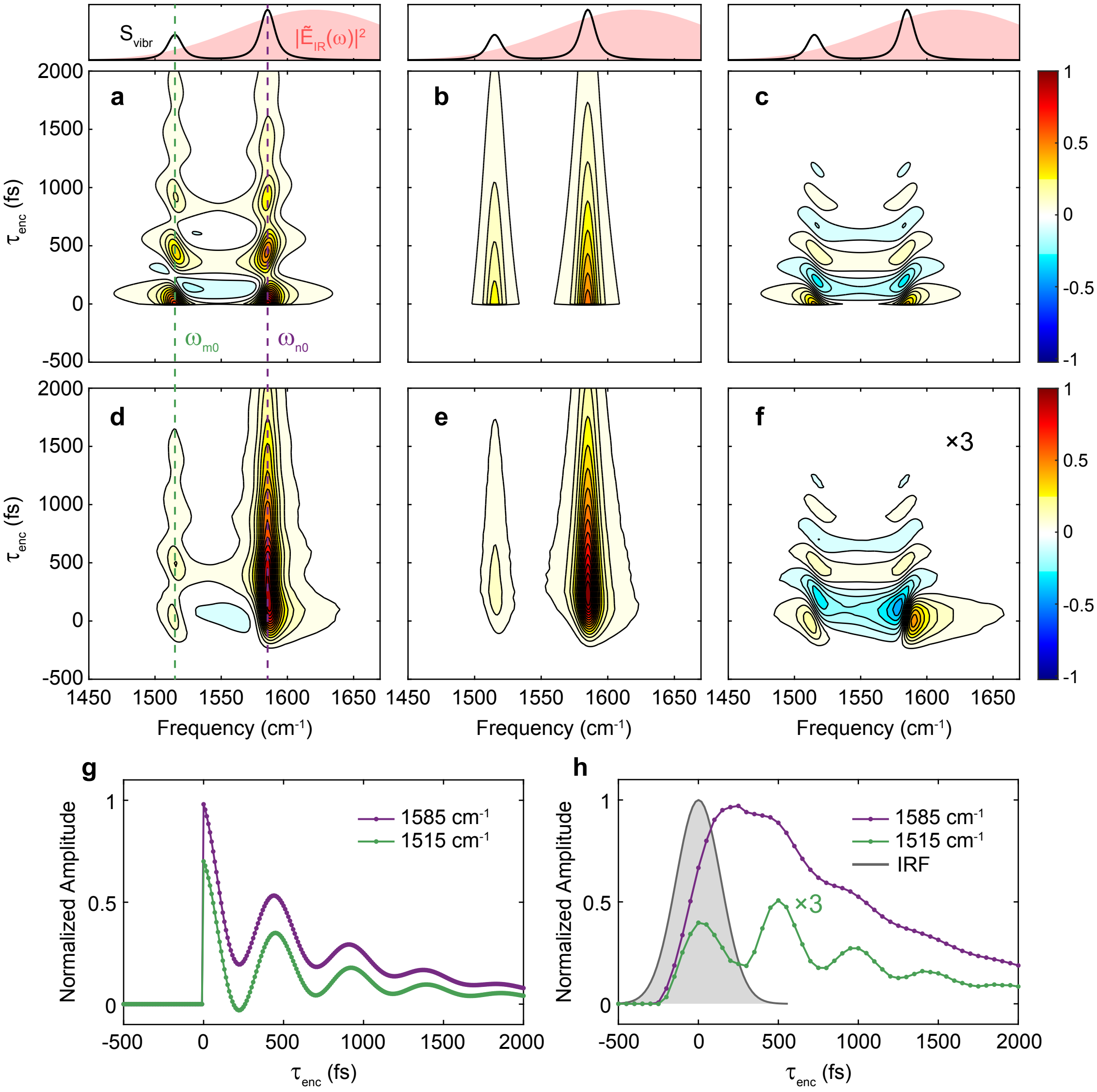

FIG. 4. Comparison of the impulsive and finite-pulse τ_{enc}-dependent FEIR spectrum for the two-mode system. Impulsive limit (a) total spectrum, (b) population contribution, and (c) coherence contribution. The upper panels plot the FEIR activity spectrum S_{vibr} and IR pulse spectrum $|\tilde{E}_{\mathrm{IR}}|^2$ for reference. (d)-(f) show the analogous quantities as (a)-(c) for the finite-pulse case. In both cases the total spectrum is normalized to its maximum value, and the population and coherence components are plotted on the same scale. Contouring spacing is set at 6.7%. Panel (f) has been additionally scaled by a factor of 3 for better visualization of the small amplitude. (g) and (h) show slices through the two vibrational resonances ω_{m0} = 1515 cm^{-1} and ω_{n0} = 1585 cm^{-1} for the impulsive and finite-pulse τ_{enc}-dependent spectra, respectively. The IRF is included in (h), and the 1515 cm^{-1} trace has also been scaled by a factor of 3.

tional coherence contribution in the total spectrum over the lower-frequency band is even further amplified relative to that in the impulsive limit, producing the much deeper coherent modulation in the τ_{enc}-slice along ω_{m0} compared to that along ω_{n0} (Fig. 4(h)).

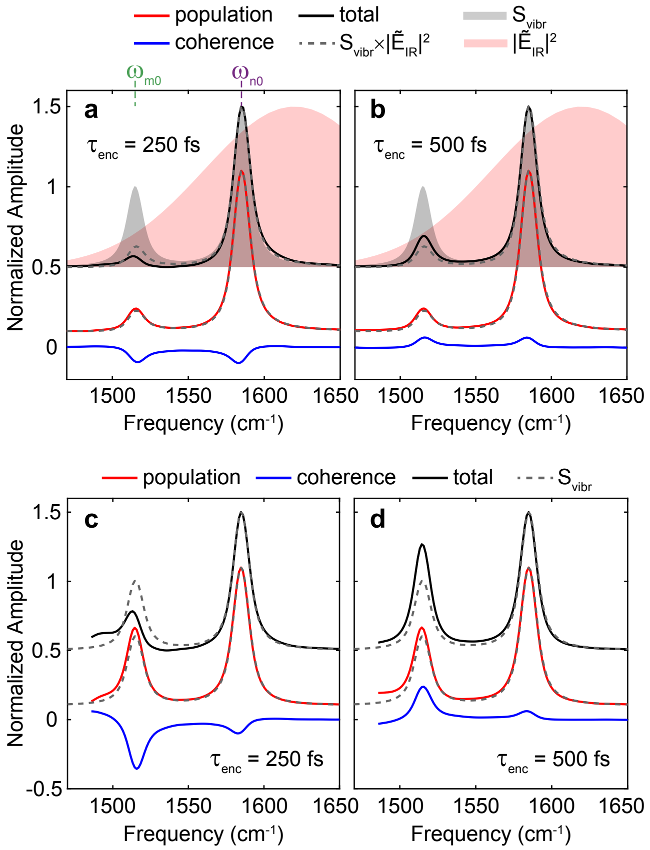

FIG. 5. Effect of IR spectral filtering and pump-normalization on FEIR spectra for the two-mode system. Finite-pulse FEIR spectra (black) at (a) τ_{enc} = 250 fs and (b) τ_{enc} = 500 fs including the decomposition into population (red) and coherence (blue) contributions (spectra and population component vertically offset for clarity). The IR pulse spectrum $|\tilde{E}_{\mathrm{IR}}|^2$ (red fill) and IR-vibronic spectrum S_{vibr} (gray fill) are plotted behind the total spectrum, while their product $S_{\mathrm{vibr}} \times |\tilde{E}_{\mathrm{IR}}|^2$ (dashed gray) is overlayed on both the total spectrum and population contribution. (c) τ_{enc} = 250 fs and (d) τ_{enc} = 500 fs pump-normalized FEIR spectra with decomposition into population and coherence components. S_{vibr} (dashed gray) is plotted over the total spectrum and population component.

D. Spectral filtering and pump-normalization

The spectral filtering effect of the finite IR bandwidth is examined in more detail in Fig. 5. The finite-pulse FEIR spectrum and its population and coherence contributions are shown at encoding delays corresponding to a coherence phase of $\phi_{mn} \sim \pi$ (τ_{enc} = 250 fs, Fig. 5(a)) and $\phi_{mn} \sim 2\pi$ (τ_{enc} = 500 fs, Fig. 5(b)). In both cases, the population response is simply windowed by the IR pulse spectrum, as can be seen by the nearly perfect overlay of the population contribution on $S_{\text{vibr}} \times |\tilde{E}_{\text{IR}}|^2$. This straightforward spectral reshaping of the population features is in line with the intuitive double-resonance absorption picture for FEIR excitation—namely, the magnitude of response at a given vibrational frequency is simply scaled by the IR intensity at that frequency. On the other hand, the excitation of vibrational coherence is non-local in frequency in that it depends on the IR pump intensity over both resonances. As a result, the coherence amplitude remains equal and symmetric over both bands, as evident in Figs. 5(a) and (b). In general, this state of affairs holds for any pair of vibrations with arbitrary transform-limited pulses outside the pulse-overlap region. Within IR/Vis pulse overlap additional distortions appear, for example leading to the enhancement of the coherence amplitude near the center of the IR spectrum evident in Fig. 4(f). Additionally, the population features are subject to an IR detuning-dependent phase distortion (producing the barely noticeable band-asymmetry near $\tau_{\text{enc}} = 0$ evident in the lowest contour in Fig. 4(e)), which is discussed further in Sec. S2. The differing ways in which pulse spectra filter population and coherence pathways is a generic phenomenon in ultrafast experiments, and has been described in 2D spectroscopy.[17,34,52]

Because the IR pulse spectrum reshapes the FEIR response in the frequency domain, it would appear reasonable to pump-normalize the data, i.e. divide the FEIR spectrum by the IR pump spectrum used in the measurement

$$S_{\text{pnorm}}(\omega, \tau_{\text{enc}}) = \frac{S(\omega, \tau_{\text{enc}})}{|\tilde{E}_{\text{IR}}(\omega)|^2}. \tag{1}$$

Figures 5(c) and (d) show the pump-normalized FEIR spectra and their population and coherence components corresponding to panels (a) and (b), respectively. In light of the discussion in the previous paragraph, this pump-normalization procedure correctly "undoes" the spectral windowing of the population pathways (outside of pulse overlap), but incorrectly treats the coherence pathways. Specifically, while the pump-normalized population contribution overlays onto S_{vibr}, pump-normalizing the coherence contribution artificially inflates its amplitude over the weaker ω_{m0} band in the wing of the IR spectrum. When the coherence phase is negative absorptive ($\phi_{mn} \sim \pi k$ for integer k and positively-signed coherence) as in Fig. 5(c), the result is an apparent suppression of the weaker mode's amplitude compared to S_{vibr}. Conversely, on the positive absorptive side of the coherence cycle ($\phi_{mn} \sim 2\pi k$), the weak mode's amplitude is exaggerated, as in Fig. 5(d).

It is important to note that the presence of vibrational coherence will always complicate the correspondence between a multimode FEIR spectrum and the ideal FEIR activity spectrum S_{vibr}, even in the impulsive limit. However, as this analysis shows, the effect of the IR pulse spectrum can further complicate the apparent strength of a given resonance through the different way in which population and coherence pathways are affected. For example, a naive assessment of the relative FEIR activity of modes m and n based on their relative peak band intensities from the pump-corrected spectra in Figs. 5(c) or (d) would alternately underestimate the activity of mode m by 56%, or overestimate it by 54%, respectively. We will not consider pump-normalized FEIR spectra in our analysis of experiments in the remainder of the paper. In situations were it is possible to separate the population and coherence contributions, i.e. by way of Fourier transformation along τ_{enc},[53] the isolated population-only spectrum may in principle be pump-corrected by Eq. 1, although phase distortions to the population response within IR/Vis pulse-overlap (Sec. S2) may complicate this separation procedure and will not be removed.

IV. IMPACT OF VIBRATIONAL COHERENCE IN THE FEIR SPECTROSCOPY OF C6

A. Experimental IR spectrum and simulated model system

In this section we analyze experimental FEIR signals from the high frequency ring modes of C6 with the aid of descriptive response function calculations. C6 is an important model system that we have used previously to benchmark the sensitivity limits of FEIR detection.[9,16,54] However, we have so far not discussed in detail the τ_{enc}-dependent behavior of these FEIR measurements. Interestingly, the signal in these experiments is especially well-suited to high-sensitivity detection, because the FEIR spectrum exhibits intuitive absorptive features at the encoding delay of peak brightness (τ_{enc} = 0.6 ps, see Fig. 1). Here we show how vibrational coherence and finite-pulse effects conspire to produce these beneficial τ_{enc}-dependent characteristics.

Figure 6 shows the experimental FTIR absorption spectrum of C6 with DFT-calculated ground-state normal mode frequencies and intensities overlayed. The experimental FEIR measurements can be adequately described by considering only the three most intense bands, labelled in order of descending frequency as ν_{R1} (experimental frequency 1616 cm^{-1}), ν_{R2} (1586 cm^{-1}), and ν_{R3} (1515 cm^{-1}). Based on the DFT calculation we assign these three bands to various in-plane ring

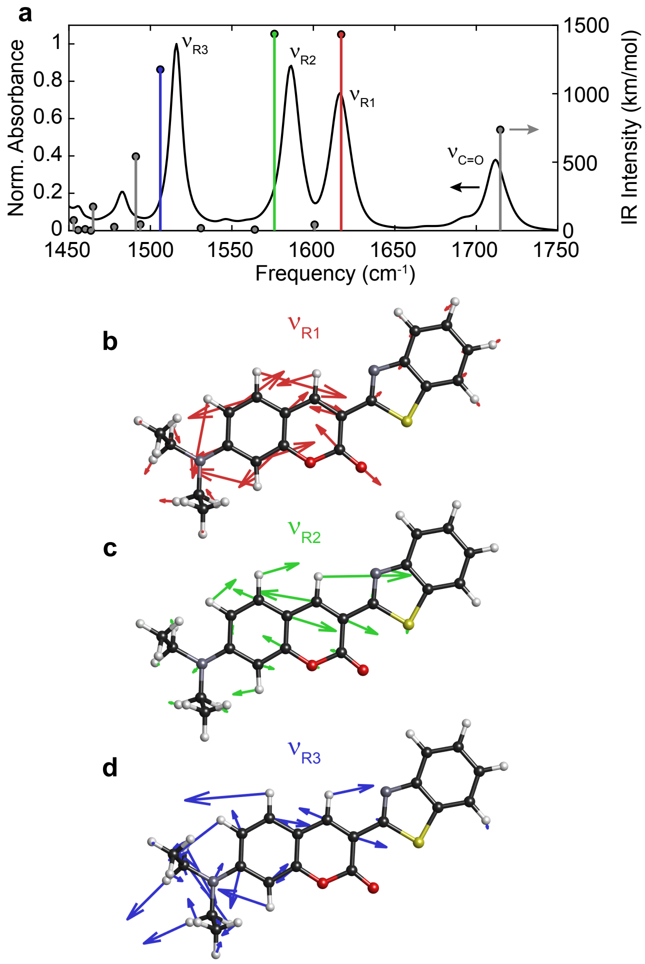

FIG. 6. C6 experimental FTIR absorption spectrum and normal modes calculated by DFT. (a) Solvent-subtracted and normalized FTIR absorption (left y axis) with frequencies and intensities of DFT-calculated normal modes (right y axis) overlayed. The calculated frequencies have been scaled by a factor of 0.973 for convenient visualization. The three normal modes involved in the FEIR calculation ν_{R3}, ν_{R2}, ν_{R1}, are assigned in (a), and their atomic displacements are shown with the same color-coding in (b)-(d), respectively. The displacement vectors are normalized to the largest in each normal mode.

vibrations of the coumarin core, for which normal mode atomic displacement vectors are shown in Figs. 6(b)-(d). The mode ν_{R3} also has substantial contributions from bending motions of the diethylamino substituent. The DFT-calculated transition dipole vectors of these three ring modes are all aligned roughly parallel to the $S_0 \rightarrow S_1$ electronic transition dipole (Fig. S18). The band at 1712 cm^{-1} in experiment corresponds to the lactone carbonyl stretch $\nu_{\mathrm{C=O}}$, but is not sufficiently FEIR active to contribute significantly to the measurement with the IR pump spectrum used, and will not be included in the calculation.

Mode	ω_{10} (cm^{-1})	μ_{10}	$\langle 0^e \vert 1^g \rangle$	$\Gamma_{10}^{-1} = \Gamma_{11}^{-1}$ (fs)
ν_{R3}	1515	0.945	0.137	1178
ν_{R2}	1586	1	0.266	935
ν_{R1}	1616	0.961	-0.094	846

TABLE II. Response function parameters for the C6 calculation. The vibrational transition moments are defined relative to ν_{R2}. The intermode coherence dephasing between each pair of fundamentals is set to Γ_{ij}^{-1} = 400 fs.

The experiments are performed in *ZZZZ* polarization, however, we only calculate the vibronic response as the roughly parallel transition dipoles produce a uniform orientational contribution across every pathway. The relevant parameters for the response function are listed in Table II. The fundamental frequencies ω_{10}, vibrational transition moments μ_{10}, and dephasings Γ_{10}^{-1} are taken from Lorentzian fits to the respective bands in the FTIR spectrum (Sec. S7), and vibrational population relaxation is set by assuming lifetime broadening. We use the DFT-calculated values of the FC factors. There are three pairs of intermode vibrational coherences, and we set the dephasing time for each to 400 fs. As in Sec. III, the dephasing time of the encoding transitions are all set to Γ_{e1}^{-1} = 10 fs, and we use the same transform-limited pulses satisfying $\omega_{e0} = \omega_{\mathrm{IR}} + \omega_{\mathrm{vis}}$.

B. Encoding-delay dependence of the FEIR spectrum and two-pulse signal

The overall comparison of experimental and calculated τ_{enc}-dependent FEIR signals is shown in Figs. 7 and 8. Figs. 7(a) and (d) compare the coverage of the vibrational resonances by the IR pulse spectrum in the experiment and model calculation, respectively. Both the model's linear IR absorption spectrum S_{IR} and FEIR activity spectrum S_{vibr} are shown to indicate the differing FC activity of the modes.

We start by identifying some of the most salient features of the experimental signals. Figure 7(b) shows the full τ_{enc}-dependent FEIR spectrum, with slices taken along the frequencies of the three bands plotted in Fig. 7(c). Overall, the response is dominated the ν_{R2} mode. Coherent modulation is strongly apparent over the ν_{R3} band, but less obvious on the other two resonances.

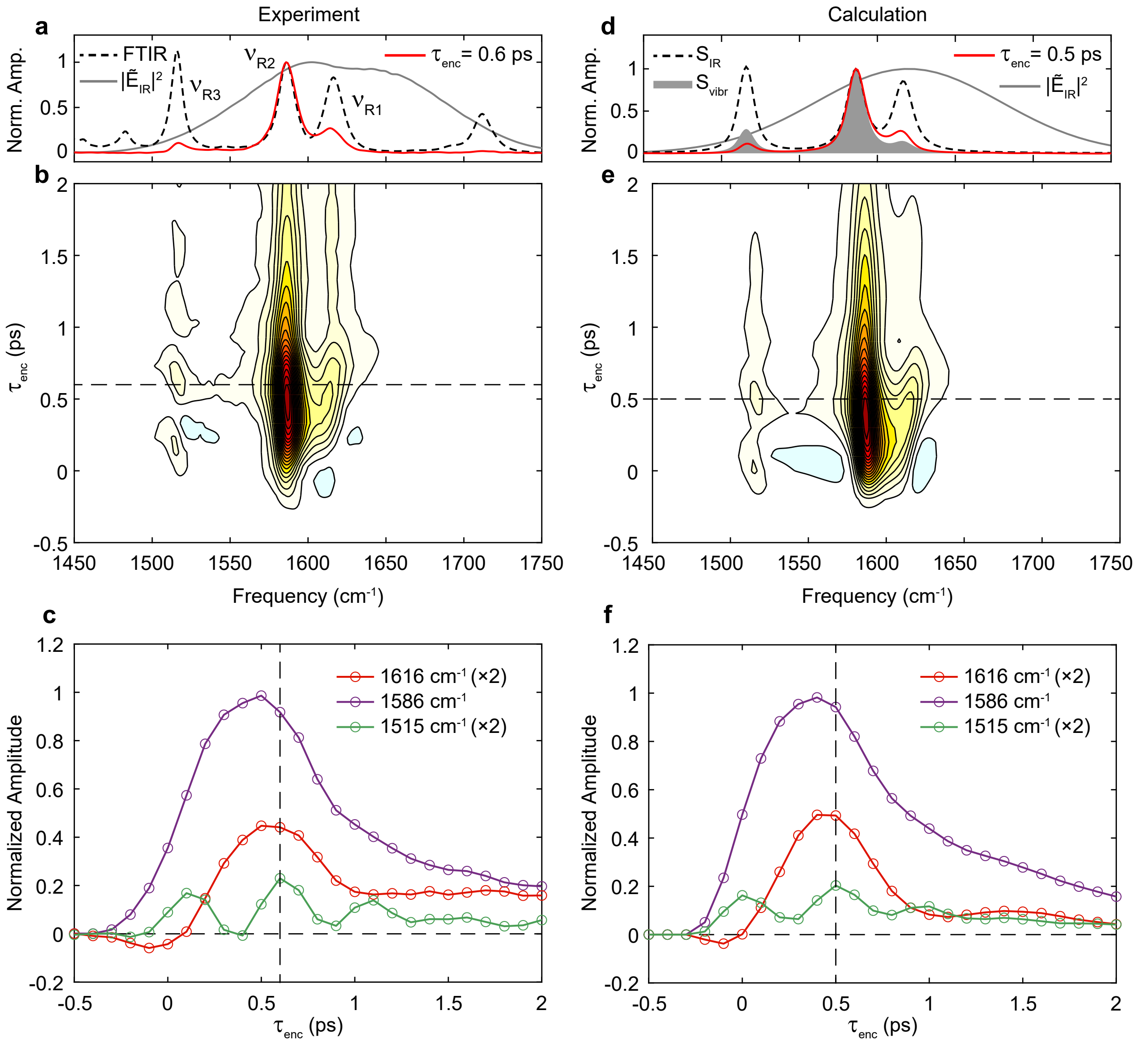

FIG. 7. Comparison of (a)-(c) experimental and (d)-(f) calculated τ_{enc}-dependent FEIR spectra of C6. (a) Experimental FTIR spectrum (dashed black), IR pulse spectrum (gray), and FEIR spectrum at τ_{enc} = 0.6 ps (red). (b) Experimental τ_{enc}-dependent FEIR spectrum. (c) Slices along the three vibrational mode frequencies ν_{R1} (1616 cm^{-1}), ν_{R2} (1586 cm^{-1}), and ν_{R3} (1515 cm^{-1}). Dashed lines in (b) and (c) indicate τ_{enc} = 0.6 ps. Panels (d)-(f) show the calculated signals analogous to those in (a)-(c), where τ_{enc} = 0.5 ps has been used instead. Contour spacing for both surfaces (b) and (e) is set at 5%. In (c) and (f) the ν_{R1} and ν_{R3} traces have been scaled up by a factor of 2 for more convenient visualization.

Figure 8(a) shows the experimental two-pulse signal. The τ_{enc}-projection of the surface in Fig. 7(b) has been superimposed to demonstrate the projection-slice relationship between these two measurements. The two-pulse signal exhibits very little obvious beating, although subtle features in its τ_{enc}-dependent shape are visible. Notably, this signal is peaked at $\tau_{\text{enc}} \sim 0.6$ ps—safely beyond the pulse-overlap region as shown in Fig. 1. At this encoding delay, the bands in the FEIR spectrum (Fig. 7(a)) have essentially absorptive lineshapes that closely match those in the FTIR spectrum, although their relative amplitudes are reweighed by the differing vibronic activities. Taken together, these characteristics, i.e. an intuitive spectrum at maximum signal strength, make this system an ideal example case for demonstrating high sensitivity FEIR vibrational detection, hence its use in Refs. 9, 16, and 54.

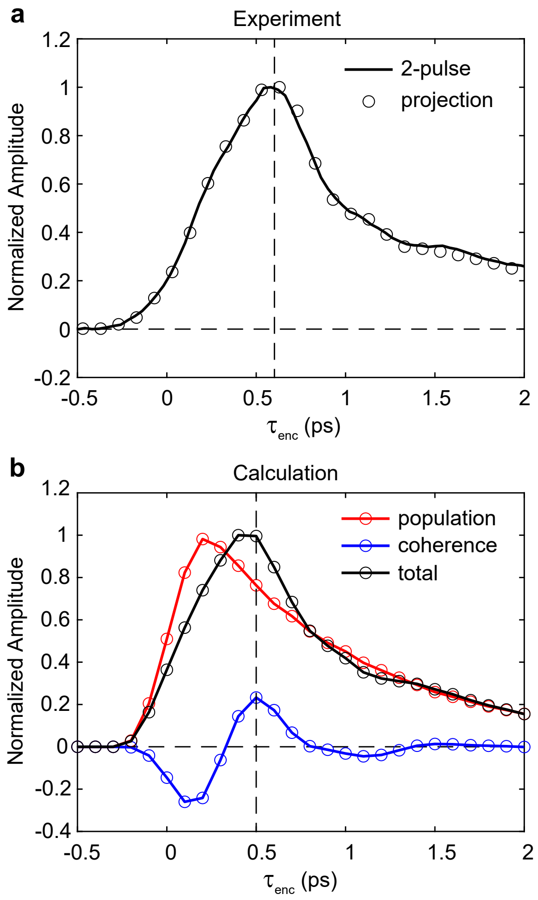

FIG. 8. Comparison of experimental and calculated two-pulse signals from C6. (a) Experimental two-pulse signal (solid) and τ_{enc}-projection of the spectrum (circles). (b) Calculated two-pulse signal (black) and its decomposition into population (red) and coherence (blue) contributions. Vertical dashed lines indicate τ_{enc} = 600 and 500 fs in (a) and (b), respectively.

To gain insight into the origin of these features we turn to the calculated signals, shown in Figs. 7(d)-(f) and Fig. 8(b). The three-mode model with finite pulses succeeds in qualitatively capturing the τ_{enc}-dependence of the spectrum and two-pulse transient across the entire early-time region including pulse overlap. Overall, the observed behavior can be seen to originate from the dominant FEIR activity of the ν_{R2} mode (modelled activities appearing in ratio ν_{R3}:ν_{R2}:ν_{R1} = 0.24:1:0.12), the signs of the coherences, and the coverage by the IR pulse spectrum. Because ν_{R2} has a much larger FEIR activity than ν_{R1} and ν_{R3}, the amplitudes of the ν_{R2}-ν_{R1} and ν_{R2}-ν_{R3} coherences are significant relative to the ν_{R1} and ν_{R3} population features, but only minor contributions relative to the strong ν_{R2} population band. The relative signs of the FC factors—$(+,+,-)$ for (ν_{R3},ν_{R2},ν_{R1})—are such that the ν_{R2}-ν_{R3} coherence is positively signed, while the ν_{R2}-ν_{R1} coherence is negatively signed. The ν_{R1}-ν_{R3} coherence is negligible in comparison due to the small FEIR activities of the modes involved. The signature of the positive ν_{R2}-ν_{R3} coherence is seen in the appearance of the first oscillatory peak of the ν_{R3} band near τ_{enc} = 0 ps (Figs. 7(e)-(f)). On the contrary, the negative ν_{R2}-ν_{R1} coherence results in a shallow negative dip along the ν_{R1} mode near τ_{enc} = 0 ps, followed by a first maximum near τ_{enc} = 0.5 ps (roughly half of the $\sim$1.1 ps coherence period). This slow coherence evolution—with a period longer than its dephasing time so that not quite a full cycle is apparent—makes the ν_{R1} band appear to "grow in" with a delay, which could possibly lead to an incorrect interpretation of the data in terms of vibrational energy transfer. The negative sign of the ν_{R2}-ν_{R1} coherence is a thus a dominant factor in shaping the early-time spectrum, which can be further appreciated by comparing against the poor experimental match of an otherwise identical simulation with this sign flipped (Fig. S19).

A more detailed view of these interferences as well as the effect of finite pulses is presented in Fig. 9, which shows the population and coherence decomposition of the calculated impulsive and finite-pulse spectra. The frequency differences between the modes, $\omega_{R2} - \omega_{R3}$ = 71 cm^{-1} and $\omega_{R1} - \omega_{R2}$ = 30 cm^{-1}, are such that $\omega_{R2} - \omega_{R3} \approx 2(\omega_{R1} - \omega_{R2})$. This approximate frequency-difference relation between the mode pairs, together with their oppositely-signed coherences, produces a striking coincidental alignment of their coherence phases. Specifically, the location of the negative ν_{R2}-ν_{R1} coherence's first maximum near $\tau_{\text{enc}} \sim$ 0.5 ps (coherence phase $\phi_{ij} \sim \pi$) roughly coincides with the positive ν_{R2}-ν_{R3} coherence's first recurrence ($\phi_{ij} \sim 2\pi$). As a result, the total coherence lineshape is essentially positive absorptive across all modes at this encoding delay, which can be seen in Figs. 9(c) and (f). The finite-pulse amplitude of the ν_{R2}-ν_{R3} coherence is greatly reduced relative to that of ν_{R2}-ν_{R1} (evident in Fig. 9(f)) through both spectral windowing by the IR pulse as well as the τ_{enc} convolution filter effect. Applying the γ_2 = -7800 fs^2 second-order dispersion to chirp the IR pulse out to the experimentally-measured duration produces slightly better agreement with the shape of the experimental τ_{enc}-dependent spectrum,

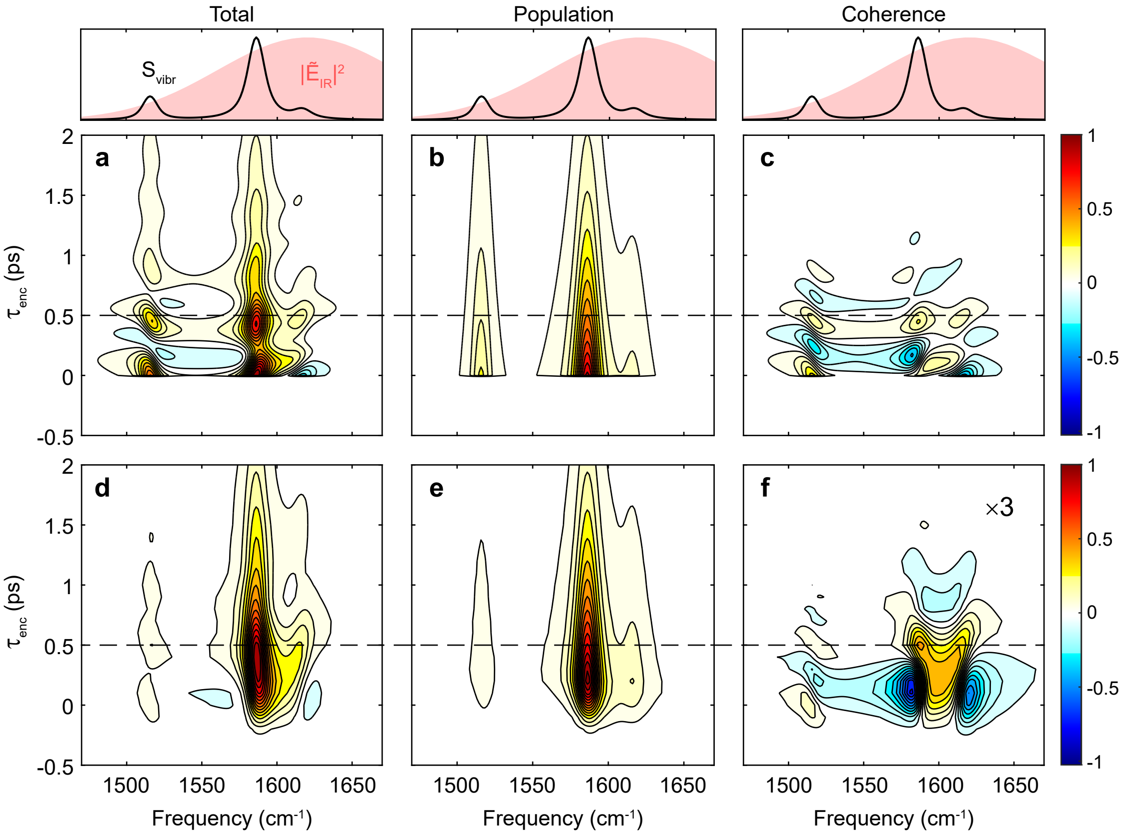

FIG. 9. Comparison of the calculated (a)-(c) impulsive and (d)-(f) finite-pulse $\tau_{\rm enc}$-dependent spectra for the C6 model. Impulsive limit (a) total spectrum, (b) population contribution, and (c) coherence contribution. The upper panels plot the IR pulse spectrum overlayed on the IR-vibronic spectrum $S_{\rm vibr}$. (d)-(f) show the analogous quantities as (a)-(c) for the finite-pulse case. In both cases the total spectrum is normalized to its maximum value, and the components are plotted on the same scale. In all cases the contour spacing is set at 6.7%. Panel (f) has been additionally scaled by a factor of 3 for better visualization of the small amplitude.

notably with a minor delay of the $\nu_{\rm R3}$ coherence beating (Fig. S25).

The combined effect of the interference between these coherences and the population response are therefore seen to give rise to the convenient features of the C6 response mentioned above. Namely, the peaking of the $\nu_{\rm R1}$ and $\nu_{\rm R2}$ bands near $\tau_{\rm enc}$ = 0.4-0.5 ps in the calculation is due to alternating destructive and constructive interference of their negatively-signed coherence's $\phi_{ij} = 0$ minimum ($\tau_{\rm enc} \sim 0$ ps) and $\phi_{ij} = \pi$ maximum ($\tau_{\rm enc} \sim 0.5$ ps) with the population response, respectively. As these two resonances together make up the majority of the overall response under these IR pump conditions, the two-pulse signal is correspondingly peaked near $\tau_{\rm enc} \sim 0.5$ ps in simulation as well. In fact, as shown in Fig. 8(b), roughly 20% of the total FEIR signal at its maximum is due to coherence. The fact the all three modes then exhibit absorptive lineshapes at this encoding delay is due to the approximate alignment of coherence phases resulting from the chance frequency-difference relationship $\omega_{\mathrm{R2}} - \omega_{\mathrm{R3}} \approx 2(\omega_{\mathrm{R1}} - \omega_{\mathrm{R2}})$. We note that the τ_{enc} Fourier transform approach to separating population and coherence contributions introduced in Ref. 53 cannot be successfully applied to these FEIR experiments, as the frequency content of the coherence beating is not cleanly separated from that of the population decay (notably for the ν_{R2}-ν_{R1} coherence). This is also the case for the measurements on C343 analyzed in Sec. V B.

C. Assessment of experimental τ_{enc} = 0 assignment

The overall qualitative agreement between the early-time τ_{enc}-dependence of the experimental and calculated signals supports our assignment of τ_{enc} = 0 in experiment. However, a more careful comparison reveals a discrepancy of ~100-150 fs in timing between the calculation and experiment, e.g. evident by the relative offset between the maxima of two-pulse signals in Figs. 8(a) and (b) as well as the τ_{enc}-dependent spectra in Fig. 7. On the side of the calculation, one contribution to the discrepancy is our use of transform-limited Gaussian pulses, of which the IR is notably shorter (~105 fs) than the chirped and spectrally non-Gaussian IR pulse in experiment (~230 fs). Simulations using chirped IR pulses with durations matched to those in experiment further delay the two-pulse signal peak by ~70 fs and produce better overall agreement with the τ_{enc} evolution of the spectrum (Figs. S24 and S25 in the supplementary material), but do not fully account for the timing discrepancy. Another possible contribution is from the highly idealized nature of our homogeneous-limit three-mode model, whose parameters have not been allowed to vary to optimize the fit against the FEIR experiment. On the other hand, this discrepancy is also within the instrumental uncertainty in τ_{enc} timing from sample to sample and could therefore represent an error in our experimental τ_{enc} = 0 assignment.

V. POLARIZATION DEPENDENCE AND ORIENTATIONAL EFFECTS

A. Polarization-dependent response of a single-mode system: C337 nitrile stretch

We begin our demonstration of orientational effects in FEIR spectroscopy by analyzing polarization-dependent experiments on the simplest case of a single-mode system. As the FEIR signal is entirely composed of population response free of vibrational coherence, its orientational contribution is governed by the simpler two-dipole orientational correlation functions and we can more clearly evaluate the predictions of the theoretical description in Paper I. For this purpose, the nitrile stretch vibration of C337 shown in Fig. 10(a) is a convenient choice of model system, as the vibrational resonance is spectrally isolated as well as being a local mode that has an intuitive transition dipole orientation within the molecule. As calculated by DFT, the nitrile's transition dipole is oriented nearly anti-parallel to the $S_0 \rightarrow S_1$ electronic transition dipole, forming an angle of $\theta = 172^\circ$. The electronic transition dipole falls roughly along a line connecting the electron-donating amino substituent with the electron-withdrawing nitrile, consistent with the charge-transfer character of the transition.[55,56] This orientation of the electronic transition dipole within the coumarin core is roughly conserved in DFT calculations of the coumarins studied in this work.

Figure 10(b) shows the nitrile's FTIR absorption spectrum and τ_{enc}-dependent FEIR spectrum for *ZZZZ* polarization. During pulse overlap, the FEIR signal is contaminated by a TPA signal extended along the IR pulse spectrum. Interestingly, within the TPA feature at τ_{enc} = 0 ps the nitrile band appears as a fully dispersive resonance resembling a Fano lineshape.[57] This phase distortion is not accounted for by the pulse-overlap induced phase artifact mentioned in Sec. III and discussed in Sec. S2, which would have an oppositely-signed twist. A possible explanation might involve coupling of the IR-vibrational resonance to the molecule's polarizability. This dispersive feature fully decays with the IRF, and by $\tau_{\text{enc}} > 0.5$ ps an intuitive absorptive lineshape matching that of the FTIR spectrum is present, indicative of pure population response.

The experimental polarization-dependence of the two-pulse FEIR signal at τ_{enc} = 1 ps is shown in Figure 10(c). This dependence is well fit by the form $a\cos^2\Theta + b$ predicted by the theory in Paper I. The fit produces an anisotropy of r = 0.29, which corresponds to a relative angle of θ = 154° by Eq. 34 of Paper I, and is somewhat lower than r = 0.39 predicted using the DFT-calculated relative angle θ = 172°. One potential explanation for this discrepancy on the experimental side is the effect of impure linear polarization, and possibly out-of-plane components of the IR and visible fields resulting from the high numerical aperture focusing in the FEIR microscope.[58,59] Further characterization of this effect would be necessary to ensure quantitative anisotropies can be reliably measured.

The two-pulse signals in *ZZZZ* and *ZZYY* polarization and resulting anisotropy decay are shown in Figure 10(e). The pulse-overlap TPA signal produces the large spike at τ_{enc} = 0 ps in both polarizations, and the amplitude of the ensuing true FEIR response is significantly smaller.

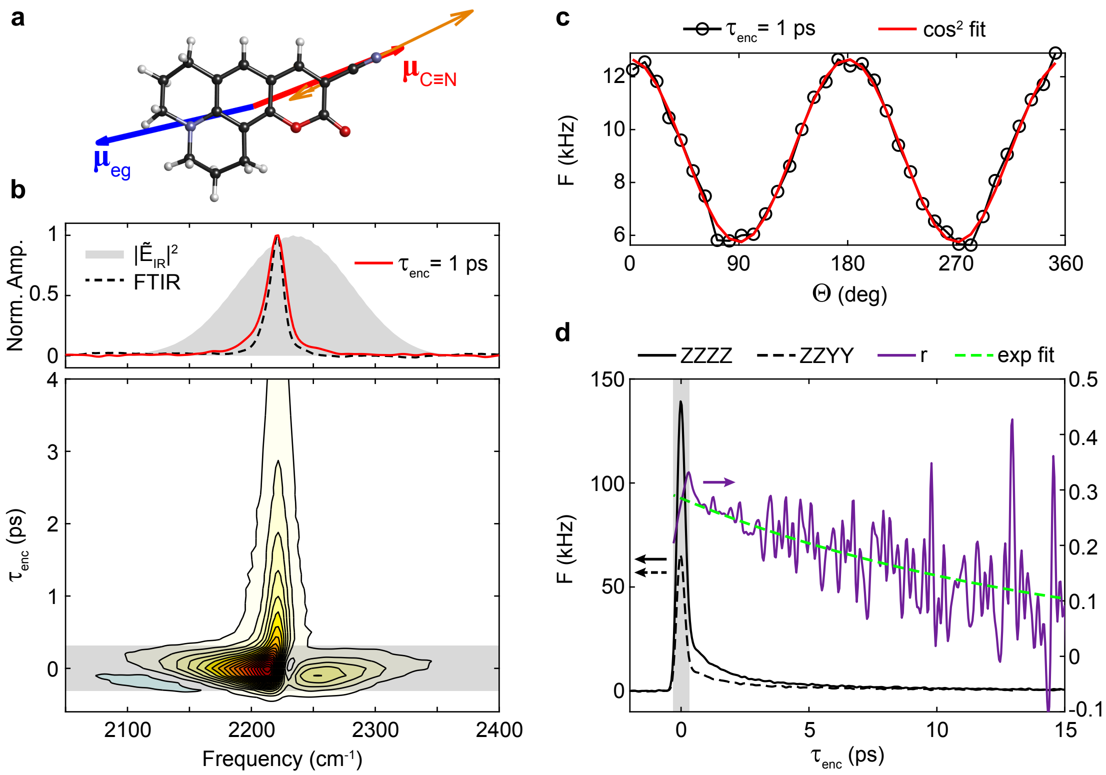

FIG. 10. Polarization-dependent FEIR signals from the C337 nitrile stretch. (a) DFT optimized ground-state structure of C337, showing the atomic displacement vectors associated with the nitrile stretch (orange), its transition dipole unit vector (red), and the $S_0 \rightarrow S_1$ electronic transition dipole unit vector (blue). (b) Top panel: *ZZZZ* FEIR spectrum at $\tau_{\rm enc}$ = 1 ps (red) and pump-scaled FTIR spectrum (dashed black) of the nitrile stretch mode. The IR pump spectrum is overlayed in gray. Bottom panel: $\tau_{\rm enc}$-dependent FEIR spectrum with the pulse overlap region ($1/e^2$ full-width) indicated by a grayed-out box. Contour spacing is set at 5%. (c) Polarization-dependence of the background-subtracted two-pulse FEIR signal at $\tau_{\rm enc}$ = 1 ps (black circles) fit by the model $a\cos^2\Theta + b$ (red). (d) Left y axis: two-pulse FEIR signal (F, expressed as a photon count rate) in *ZZZZ* (solid black) and *ZZYY* (dashed black) polarization, with the pulse overlap region grayed-out. Right y axis: anisotropy (solid purple) calculated from the two-pulse signals, with an exponential fit with no offset parameter (dashed green). The two-pulse measurements in (d) use a slightly higher visible intensity that that in (c), resulting in the slightly higher count rate.

The anisotropy decay is fit to a single exponential with decay constant of $\tau_r = 15 \pm 3$ ps, although this time constant should be treated as highly approximate due to the limited scan range and noisy anisotropy signal. For the orientational relaxation of a spherical rotor with rotational diffusion constant $D_{\rm rot}$ this time constant is given by $\tau_r = (6D_{\rm rot})^{-1}$.[60–62] The measured FEIR anisotropy decay timescale is consistent with reorientation times of coumarins and similarly-sized chromophores in simple polyatomic solvents measured by various time-resolved anisotropy methods.[63–65] Given these timescales, neglecting the effects of orientational dynamics is therefore a reasonable approximation at early encoding delays.

B. Orientational effects in a multimode system: polarization-dependent spectra of C343

1. *Orientational contributions to vibrational coherence*

Polarization-dependence has the potential to be especially useful in the FEIR spectroscopy of multimode systems, where measuring the relative orientation of the multiple vibrations can aid in their assignment, alleviate spectral congestion, and provide more powerful structural insight. However, the presence of vibrational coherence with its more complicated orientational dependencies can also potentially complicate the extraction of molecular-frame angles from early-time measurements. To investigate the impact of orientational effects in the coherent response and the ability of anisotropy to inform orientational assignments, we examine experimental and simulated polarization-dependent FEIR spectra of C343.

C343 presents a more complex vibrational spectrum, shown in Fig. 11(a), with six modes covered within the IR pulse bandwidth. Based on the DFT calculation (normal mode displacements shown in Fig. S20), we assign the four lowest-frequency bands to ring modes (ν_{R1} - ν_{R4}), while the bands at 1673 cm^{-1} and 1739 cm^{-1} are dominated by stretching of the lactone carbonyl (ν_{lac}) and the carboxyl carbonyl (ν_{carb}), respectively. Figure 11(b) shows the DFT-calculated orientations of the transition dipoles for each vibration and the $\mathrm{S}_0 \rightarrow \mathrm{S}_1$ electronic transition overlayed on the optimized ground-state structure. All the transition dipoles are essentially co-planar within the conjugated coumarin core (Fig. S20), so the orientational response can be fully characterized by the collection of relative angles θ between the electronic transition dipole and each vibrational transition dipole (Table III). Furthermore, the co-planar three-dipole orientational correlation functions (Eq. 32 in Paper I) can be used for the coherence pathways. Overall, this system represents an illustrative test case for demonstrating orientational effects, as a variety of different transition dipole directions are present, including the geometrically intuitive and distinct local-mode carbonyl stretches ν_{lac} and ν_{carb}.

Parameters for the response function calculation are determined in a similar manner to Sec. IV

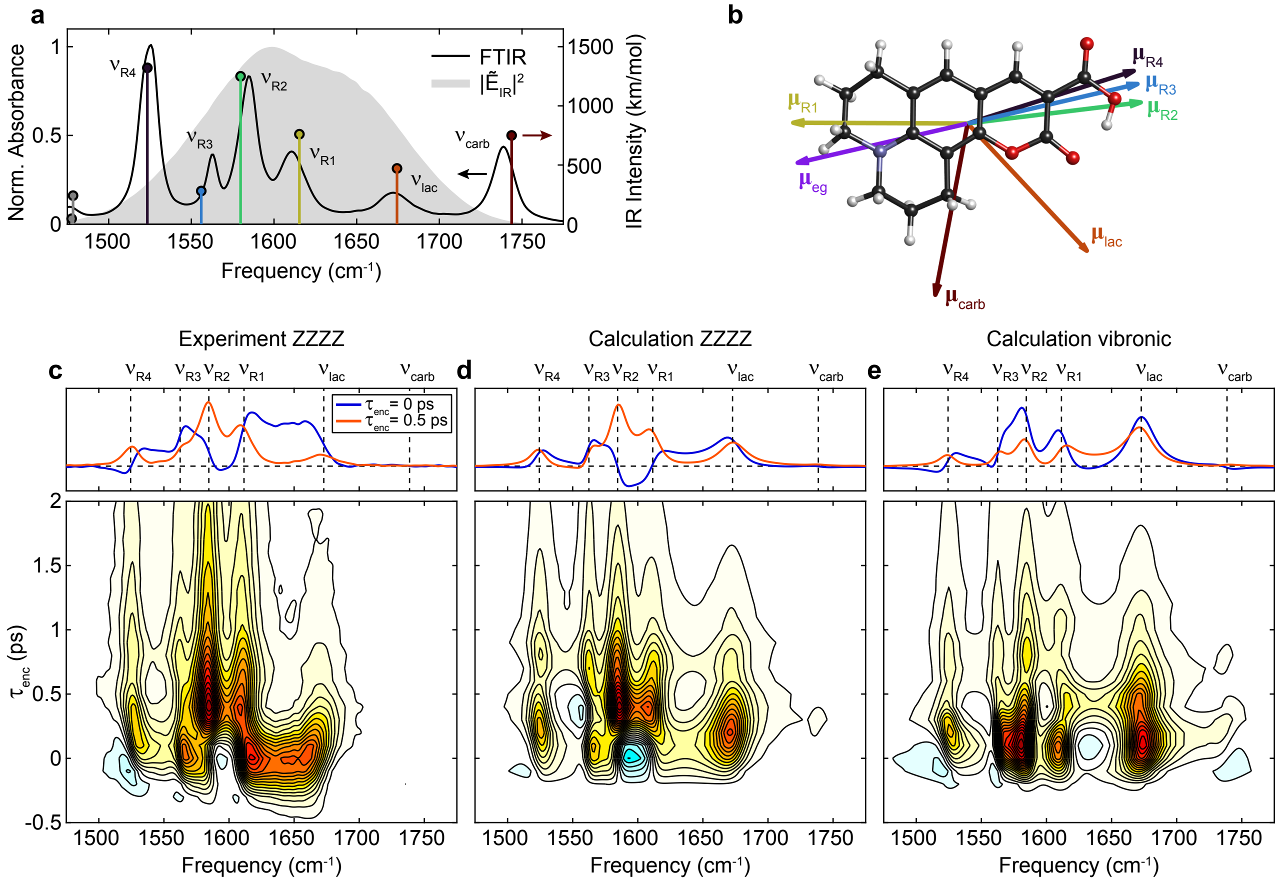

FIG. 11. Orientational effects controlling the interference of coherence and population features in C343. (a) C343 FTIR absorption spectrum (left y axis) with DFT-calculated normal mode frequencies (scaled by 0.985) and intensities (right y axis). The IR pulse spectrum used for the FEIR measurement is overlaid. (b) DFT-calculated transition dipole unit vectors for each vibrational mode and the electronic transition superimposed over the optimized ground-state structure. (c) Experimental *ZZZZ*, (d) calculated *ZZZZ*, and (e) calculated vibronic-only τ_{enc}-dependent FEIR spectra. Contouring is set at 5% intervals. The upper panels show FEIR spectra at $\tau_{\mathrm{enc}} = 0$ ps (blue) and $\tau_{\mathrm{enc}} = 0.5$ ps (orange), with a horizontal dashed line indicating the zero level. Vertical dashed lines indicate ω_{10} for each mode in Table III.

using the experimental FTIR spectrum to extract IR intensities and linewidths, and are summarized in Table III. The magnitudes of the FC factors are adjusted slightly from their DFT-calculated values (Sec. S10) to better match experiment, but their signs are left unchanged. The relative vibrational-electronic dipole angles θ described above are taken as is from the DFT calculation. We use the same transform-limited pulses as before in Secs. III and IV.

Figures 11(c)-(e) compare the experimental *ZZZZ*, calculated *ZZZZ*, and calculated vibronic-

Mode	ω_{10} (cm^{-1})	μ_{10}	$\langle 0^e \vert 1^g \rangle$	$\Gamma_{10}^{-1} = \Gamma_{11}^{-1}$ (fs)	θ (deg)
ν_{R4}	1524	1	0.075	868	175
ν_{R3}	1563	0.398	0.075	1566	178
ν_{R2}	1585	0.892	-0.075	827	174
ν_{R1}	1612	0.683	-0.085	630	13
ν_{lac}	1673	0.536	-0.25	442	120
ν_{carb}	1739	0.696	0.06	744	66

TABLE III. Response function parameters for the C343 calculation. The vibrational transition moments are defined relative to ν_{R4}. The intermode coherence dephasing between each pair of fundamentals is set to Γ_{ij}^{-1} = 300 fs.

only τ_{enc}-dependent FEIR spectrum. At early τ_{enc} the experimental FEIR spectrum has a complicated and non-intuitive structure due to interferences produced by the many coherence pathways. In particular, the spectrum at $\tau_{\mathrm{enc}} = 0$ ps bears little resemblance to the absorptive features in the FTIR spectrum, with a striking “hole” in between ν_{R2} and ν_{R1}, a ridge connecting ν_{R1} and ν_{lac}, and nearly every resonance exhibiting severe phase twists. By $\tau_{\mathrm{enc}} = 0.5$ ps the features are largely absorptive with only minor phase modulation persisting until $\sim$1 ps, and each resonance can be more or less straightforwardly mapped to one in the FTIR spectrum (ν_{carb} is not visible within the contouring of Fig. 11(c)).

The importance of the orientational response in shaping the early-time data can be appreciated by contrasting the quality of match against experiment for the calculated *ZZZZ* (Fig. 11(d)) and vibronic-only (Fig. 11(e)) spectra. The *ZZZZ* calculation qualitatively captures the complex features near $\tau_{\mathrm{enc}} = 0$ ps, including the hole between ν_{R2} and ν_{R1} and the ridge connecting ν_{R1} and ν_{lac}. In contrast, the vibronic-only calculation bears little resemblance to the experiment, with a completely different pattern of peaks within the first few hundred fs. Importantly, both calculations employ identical FC factors, whose set of relative signs evidently do not account for the pattern of interfering coherences on their own. As shown in Sec. S11, the orientational factors for the coherence pathways play the major role in reshaping the spectrum, largely caused by sign changes produced by the opposing dipole direction of ν_{R1} relative to the other ring modes. The orientational response of the population features also re-weights the relative band intensities, which is evident for $\tau_{\mathrm{enc}} > 0.5$ ps where the coherence has significantly dephased.

Although the *ZZZZ* simulation qualitatively captures the full τ_{enc}-evolution of the experimental spectrum, a discrepancy exists in the amplitude within pulse-overlap that could be indicative of a minor TPA artifact in the experiment. This is evident at $\tau_{\mathrm{enc}} = 0$ ps in experiment by the larger magnitude of ridge between ν_{R1} and ν_{lac} and less negative hole between ν_{R2} and ν_{R1}, which is consistent with the addition of a broad positive feature spanning the IR spectrum. Employing a chirped IR pulse in the simulation further improves the agreement with experiment, notably by capturing the slightly delayed grow-in of low-frequency vs. high-frequency resonances (Fig. S25 in the supplementary material).

2. *Determining vibrational dipole orientation with polarization anisotropy*

Next we demonstrate the degree to which anisotropy can be used to extract the θ angles between each vibrational dipole and the electronic transition. Figure 12 shows the FEIR spectra at $\tau_{\mathrm{enc}} = 0.5$ ps in both *ZZZZ* and *ZZYY* polarizations, along with the resulting spectral anisotropy r calculated from Eq. 33 in Paper I. Anisotropy values are only interpretable in terms of individual θ angles in the absence of coherence, which, although much reduced at this encoding delay, is still present in the spectrum. The anisotropy exhibits distinct variations over the spectrum, and we record values for each mode by averaging over the respective bands indicated in Fig. 12.

The resulting anisotropies and corresponding angles (Eq. 34 in Paper I) are summarized in Table IV along with those from the DFT calculation. Qualitatively, these anisotropies and extracted angles show reasonable agreement with the calculation, although as discussed in Section V A, the experimental anisotropies do not achieve the highest values near 0.4, here predicted for the ring modes $\nu_{\mathrm{R1-R4}}$. Additionally, the presence of residual coherence at $\tau_{\mathrm{enc}} = 0.5$ ps likely causes small variations in the anisotropies from their population response values.

Despite these potential complications the spectral anisotropy measurements provide qualitatively useful structural insight. For example, if the frequency ordering of the two carbonyls ν_{carb} and ν_{lac} was not known ahead of time by DFT calculation, the difference in their measured anisotropies combined with chemical intuition about how the C=O bonds should be oriented

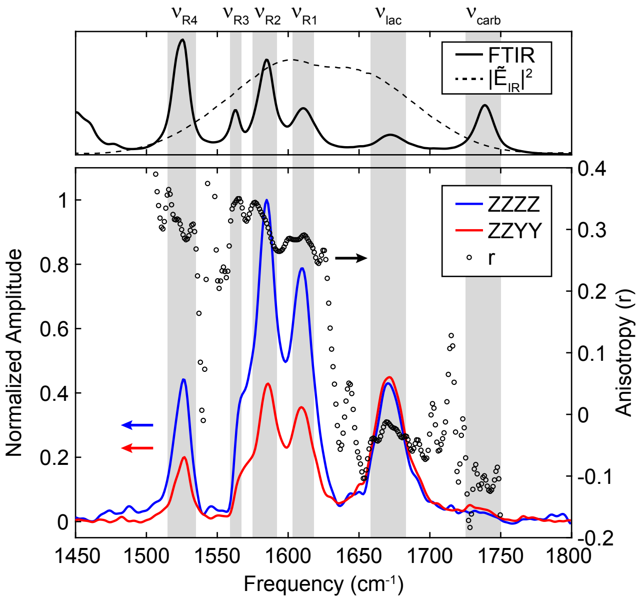

FIG. 12. C343 *ZZZZ* and *ZZYY* FEIR spectra and anisotropy at $\tau_{\mathrm{enc}} = 0.5$ ps. Top panel: FTIR spectrum with the IR pulse spectrum used in the FEIR measurements overlaid. Bottom panel: FEIR spectra (left y axis) in *ZZZZ* (blue) and *ZZYY* (red) polarizations, and the anisotropy (right y axis, black circles). The *ZZZZ* and *ZZYY* spectra are commonly normalized to the brightest feature in the *ZZZZ* spectrum. The gray bands indicate the regions the anisotropy is averaged over to produce the values in Table IV. We note that these measurements used a slightly red-shifted IR spectrum relative to that in Fig. 11.

against the electronic transition in the molecule would lead us to correctly assign ν_{lac} as the lower frequency of the two bands. Additionally, these measurements demonstrate how pulse polarization could be used as a control variable to preferentially select the response of a particular vibration. Specifically, in this case the relative strength of ν_{lac} can be amplified while suppressing the ring modes by using *ZZYY* polarization, which could be potentially beneficial for experiments seeking to use this mode as a vibrational probe of local environment.

VI. CONCLUSIONS

In this work, we have analyzed the features of τ_{enc}- and polarization-dependent FEIR spectra in the early-time region and discussed how they arise from the underlying dynamic molecular response and experimental pulse characteristics. The nonlinear response function framework developed in Paper I of this series and augmented here by numerical finite-pulse convolution is suc-

Mode	r (exp)	r (calc)	θ (exp)	θ (calc)
ν_{R4}	0.31	0.40	157°	175°
ν_{R3}	0.34	0.40	162°	178°
ν_{R2}	0.31	0.39	158°	174°
ν_{R1}	0.28	0.37	26°	13°
ν_{lac}	-0.03	-0.05	122°	120°
ν_{carb}	-0.12	-0.10	68°	66°

TABLE IV. Experimental ($\tau_{\mathrm{enc}} = 0.5$ ps, from Fig. 12) and calculated (population response) FEIR anisotropy and relative transition dipole angles for the vibrations in C343. The choice of reporting θ vs. $\pi - \theta$ for angles extracted from experimental anisotropies was made to best correspond to the calculated angles.

cessful in capturing essentially all of the τ_{enc}-dependent behavior of experimental FEIR signals. At early τ_{enc}, multimode FEIR experiments with short pulse excitation are characterized by the presence of vibrational coherence, which can interfere with the vibrational population response to create complicated spectra often difficult to interpret at face value. Our analysis provides a guide to understanding these spectra and the molecular information they contain.

Finite pulse spectra and durations influence the population and coherence contributions in different ways, and can deceptively re-weight bands in a spectrum depending on the choice of encoding delay. The relative sign of a pair of vibrations' FC factors controls the sign of their intermode coherence amplitude, which plays a prominent role in the appearance of spectra at the earliest τ_{enc}. This critical sign can be further influenced by the dipole orientation of the two vibrations against the electronic transition. Taken together, these characteristics make vibrational coherence signatures in FEIR extremely sensitive to the geometric details of vibronic coupling and dipole orientation, although the extraction and utility of this information in practice requires further investigation.

When coherence has dephased, interpreting FEIR spectra is much more straightforward. In this regime the band intensities are simply proportional to FEIR activities of the individual modes, and polarization-dependent experiments provide a means to measure the relative orientation of each vibration's transition dipole against that of the electronic transition. This orientational information can help assign multimode spectra and in general provides an additional spectroscopic handle for probing chemical structure and intermolecular interactions.

Applications of FEIR spectroscopy to single-molecule experiments are likely to employ short encoding delays where signal sizes are largest. In these scenarios the photon budget is limited, and the richness and complexity of the FEIR data investigated here, although potentially insightful, could represent complicating factors. While using short pulses to pump and encode vibrations within their picosecond lifetimes is one of the central design principles for FEIR spectroscopy, our current experiments use significantly shorter pulses than this principle necessarily dictates. Modified approaches to FEIR excitation that employ slightly longer pulses, e.g. lifetime matched to individual modes,[8] to more straightforwardly map vibrational absorption to emitted fluorescence photons are especially interesting to consider, and could be readily assessed with the theoretical and computational methods presented here.

SUPPLEMENTARY MATERIAL

See the supplementary material for details on the finite-pulse response function calculations, lineshape distortions during pulse overlap, processing steps for obtaining spectra from three-pulse experiments, description of TPA artifacts, temporal pulse and IRF characterization, τ_{enc}-dependent FEIR spectra for the coumarin series in Fig. 1, DFT-calculated dipole orientational and normal modes of C6 and C343, vibrational parameter extraction from FTIR spectra, simulated FEIR spectra of C6 with altered FC factor signs, and the effect of IR pulse dispersion in simulated FEIR data.

ACKNOWLEDGEMENTS

This work was supported by a grant from the National Science Foundation (CHE-2155027). We thank Seung Yeon Lee for helpful comments on the manuscript.

AUTHOR DECLARATIONS

Conflict of interest

The authors have no conflicts to disclose.

Author contributions

Lukas Whaley-Mayda: Conceptualization (equal); Methodology (lead); Formal analysis (lead); Visualization (lead); Writing - original draft preparation (lead). Writing - review and editing (equal). **Abhirup Guha**: Methodology (supporting); Formal analysis (supporting); Writing - review and editing (equal). **Andrei Tokmakoff**: Conceptualization (equal); Funding acquisition (lead); Supervision (lead), Writing - review and editing (equal).

DATA AVAILABILITY

The data that support the findings of this study are available from the corresponding author upon reasonable request.

REFERENCES

[1] K. Kneipp, Y. Wang, H. Kneipp, L. T. Perelman, I. Itzkan, R. R. Dasari, and M. S. Feld, "Single molecule detection using surface-enhanced Raman scattering (SERS)," Phys. Rev. Lett. **78**, 1667–1670 (1997).

[2] S. Nie and S. R. Emory, "Probing single molecules and single nanoparticles by surface-enhanced Raman scattering," Science **275**, 1102–1106 (1997).

[3] G. Haran, "Single-molecule Raman spectroscopy: A probe of surface dynamics and plasmonic fields," Acc. Chem. Res. **43**, 1135–1143 (2010).

[4] F. S. Ruggeri, B. Mannini, R. Schmid, M. Vendruscolo, and T. P. J. Knowles, "Single molecule secondary structure determination of proteins through infrared absorption nanospectroscopy," Nat. Commun. **11**, 1–9 (2020).

[5] B. Choi, G. Jeong, H.-H. Shin, and Z. H. Kim, "Molecular vibrational imaging at nanoscale," J. Chem. Phys. **156**, 160902 (2022).

[6] H. Xiong and W. Min, “Combining the best of two worlds: Stimulated Raman excited fluorescence,” J. Chem. Phys. **153**, 210901 (2020).

[7] Q. Yu, Z. Yao, H. Zhang, Z. Li, Z. Chen, and H. Xiong, “Transient stimulated Raman excited fluorescence spectroscopy,” J. Am. Chem. Soc. **145**, 7758–7762 (2023).

[8] H. Wang, D. Lee, Y. Cao, X. Bi, J. Du, K. Miao, and L. Wei, “Bond-selective fluorescence imaging with single-molecule sensitivity,” Nat. Photonics **17**, 846–855 (2023).

[9] L. Whaley-Mayda, A. Guha, S. B. Penwell, and A. Tokmakoff, “Fluorescence-encoded infrared vibrational spectroscopy with single-molecule sensitivity,” J. Am. Chem. Soc. **143**, 56 (2021).

[10] T. Elsaesser and W. Kaiser, “Vibrational and vibronic relaxation of large polyatomic molecules in liquids,” Annu. Rev. Phys. Chem. **42**, 83–107 (1991).

[11] J. C. Owrutsky, D. Raftery, and R. M. Hochstrasser, “Vibrational relaxation dynamics in solutions,” Annu. Rev. Phys. Chem. **45**, 519–555 (1994).

[12] D. J. Nesbitt and R. W. Field, “Vibrational energy flow in highly excited molecules: role of intramolecular vibrational redistribution,” J. Phys. Chem. **100**, 12735–12756 (1996).

[13] F. Wondrazek, A. Seilmeier, and W. Kaiser, “Ultrafast intramolecular redistribution and intermolecular relaxation of vibrational energy in large molecules,” Chem. Phys. Lett. **104**, 121–128 (1984).

[14] A. Seilmeier and W. Kaiser, “Ultrashort intramolecular and intermolecular vibrational energy transfer of polyatomic molecules in liquids,” in *Ultrashort Laser Pulses: Generation and Applications*, edited by W. Kaiser (Springer Berlin Heidelberg, Berlin, Heidelberg, 1993) pp. 279–317.

[15] L. Whaley-Mayda, *Fluorescence-Encoded Infrared Spectroscopy for Single-Molecule Vibrational Investigation in Solution*, Ph.D. thesis, University of Chicago (2022).

[16] L. Whaley-Mayda, A. Guha, and A. Tokmakoff, “Resonance conditions, detection quality, and single-molecule sensitivity in fluorescence-encoded infrared vibrational spectroscopy,” J. Chem. Phys. **156**, 174202 (2022).

[17] S. M. Gallagher Faeder and D. M. Jonas, “Two-dimensional electronic correlation and relaxation spectra: Theory and model calculations,” J. Phys. Chem. A **103**, 10489–10505 (1999).

[18] R. Tempelaar, A. Halpin, P. J. M. Johnson, J. Cai, R. S. Murphy, J. Knoester, R. J. D. Miller, and T. L. C. Jansen, “Laser-limited signatures of quantum coherence,” The Journal of Physical Chemistry A **120**, 3042–3048 (2016).

[19]F. V. de A. Camargo, L. Grimmelsmann, H. L. Anderson, S. R. Meech, and I. A. Heisler, "Resolving vibrational from electronic coherences in two-dimensional electronic spectroscopy: The role of the laser spectrum," Phys. Rev. Lett. **118**, 033001 (2017).

[20]V. Perlík, J. Hauer, and F. Šanda, "Finite pulse effects in single and double quantum spectroscopies," J. Opt. Soc. Am. B **34**, 430–439 (2017).

[21]T. N. Do, M. F. Gelin, and H.-S. Tan, "Simplified expressions that incorporate finite pulse effects into coherent two-dimensional optical spectra," J. Chem. Phys. **147**, 144103 (2017).

[22]T. Joo, Y. Jia, J. Yu, M. J. Lang, and G. R. Fleming, "Third-order nonlinear time domain probes of solvation dynamics," J. Chem. Phys. **104**, 6089–6108 (1996).

[23]K. Ohta, D. S. Larsen, M. Yang, and G. R. Fleming, "Influence of intramolecular vibrations in third-order, time-domain resonant spectroscopies. II. Numerical calculations," J. Chem. Phys. **114**, 8020–8039 (2001).

[24]D. A. Farrow, A. Yu, and D. M. Jonas, "Spectral relaxation in pump–probe transients," J. Chem. Phys. **118**, 9348–9356 (2003).

[25]M. Yang, "Effect of finite pulse duration in three pulse photon echo experiments: Numerical comparison of 3PEPS and S3PE," Chem. Phys. Lett. **467**, 304–308 (2009).

[26]P. F. Tekavec, J. A. Myers, K. L. M. Lewis, F. D. Fuller, and J. P. Ogilvie, "Effects of chirp on two-dimensional Fourier transform electronic spectra," Opt. Express **18**, 11015–11024 (2010).

[27]D. Polli, D. Brida, S. Mukamel, G. Lanzani, and G. Cerullo, "Effective temporal resolution in pump-probe spectroscopy with strongly chirped pulses," Phys. Rev. A **82**, 053809 (2010).

[28]C. L. Smallwood, T. M. Autry, and S. T. Cundiff, "Analytical solutions to the finite-pulse Bloch model for multidimensional coherent spectroscopy," J. Opt. Soc. Am. B **34**, 419–429 (2017).

[29]P. Hamm, "Coherent effects in femtosecond infrared spectroscopy," Chem. Phys. **200**, 415–429 (1995).

[30]S. Yan, M. T. Seidel, and H.-S. Tan, "Perturbed free induction decay in ultrafast mid-IR pump–probe spectroscopy," Chem. Phys. Lett. **517**, 36–40 (2011).

[31]A. L. Dobryakov, S. A. Kovalenko, and N. P. Ernsting, "Coherent and sequential contributions to femtosecond transient absorption spectra of a rhodamine dye in solution," J. Chem. Phys. **123**, 044502 (2005).

[32]P. Brosseau, H. Seiler, S. Palato, C. Sonnichsen, H. Baker, E. Socie, D. Strandell, and P. Kambhampati, "Perturbed free induction decay obscures early time dynamics in two-dimensional electronic spectroscopy: The case of semiconductor nanocrystals," The Journal of Chemical Physics

158, 084201 (2023).

[33] J. D. Hybl, Y. Christophe, and D. M. Jonas, "Peak shapes in femtosecond 2D correlation spectroscopy," Chem. Phys. **266**, 295–309 (2001).

[34] B. Cho, M. K. Yetzbacher, K. A. Kitney, E. R. Smith, and D. M. Jonas, "Propagation and beam geometry effects on two-dimensional Fourier transform spectra of multilevel systems," The Journal of Physical Chemistry A **113**, 13287–13299 (2009).

[35] P. Kjellberg, B. Brüggemann, and T. o. Pullerits, "Two-dimensional electronic spectroscopy of an excitonically coupled dimer," Phys. Rev. B **74**, 024303 (2006).

[36] D. Paleček, P. Edlund, E. Gustavsson, S. Westenhoff, and D. Zigmantas, "Potential pitfalls of the early-time dynamics in two-dimensional electronic spectroscopy," J. Chem. Phys. **151**, 024201 (2019).

[37] P. A. Rose and J. J. Krich, "Automatic Feynman diagram generation for nonlinear optical spectroscopies and application to fifth-order spectroscopy with pulse overlaps," J. Chem. Phys. **154**, 034109 (2021).

[38] K. Ekvall, P. van der Meulen, C. Dhollande, L.-E. Berg, S. Pommeret, R. Naskrecki, and J.-C. Mialocq, "Cross phase modulation artifact in liquid phase transient absorption spectroscopy," J. Appl. Phys. **87**, 2340–2352 (2000).

[39] M. Lorenc, M. Ziolek, R. Naskrecki, J. Karolczak, J. Kubicki, and A. Maciejewski, "Artifacts in femtosecond transient absorption spectroscopy," Appl. Phys. B: Lasers and Optics **74**, 19–27 (2002).

[40] I. Gdor, T. Ghosh, O. Lioubashevski, and S. Ruhman, "Nonresonant Raman effects on femtosecond pump–probe with chirped white light: Challenges and opportunities," J. Phys. Chem. Lett. **8**, 1920–1924 (2017).

[41] S. Mueller, S. Draeger, X. Ma, M. Hensen, T. Kenneweg, W. Pfeiffer, and T. Brixner, "Fluorescence-detected two-quantum and one-quantum–two-quantum 2D electronic spectroscopy," J. Phys. Chem. Lett. **9**, 1964–1969 (2018).

[42] M. Schröter, T. Pullerits, and O. Kühn, "Using fluorescence detected two-dimensional spectroscopy to investigate initial exciton delocalization between coupled chromophores," J. Chem. Phys. **149**, 114107 (2018).

[43] O. Kühn, T. Mančal, and T. Pullerits, "Interpreting fluorescence detected two-dimensional electronic spectroscopy," J. Phys. Chem. Lett. **11**, 838–842 (2020).

[44] P. Malý, J. Lüttig, S. Mueller, M. H. Schreck, C. Lambert, and T. Brixner, "Coherently and fluorescence-detected two-dimensional electronic spectroscopy: direct comparison on squaraine dimers," Phys. Chem. Chem. Phys. **22**, 21222–21237 (2020).

[45] P. Malý and T. Brixner, "Fluorescence-detected pump–probe spectroscopy," Angew. Chem. Int. Ed. **60**, 18867–18875 (2021).

[46] S. B. Penwell, L. Whaley-Mayda, and A. Tokmakoff, "Single-stage MHz mid-IR OPA using $LiGaS_2$ and a fiber laser pump source," Opt. Lett. **43**, 1363 (2018).

[47] S. M. Gallagher Faeder and D. M. Jonas, "Phase-resolved time-domain nonlinear optical signals," Phys. Rev. A **62**, 033820 (2000).

[48] F. Santoro, A. Lami, R. Improta, and V. Barone, "Effective method to compute vibrationally resolved optical spectra of large molecules at finite temperature in the gas phase and in solution," J. Chem. Phys. **126**, 184102 (2007).

[49] F. Santoro, "Fcclasses: A fortran 77 code," http://www.pi.iccom.cnr.it/fcclasses (2008).

[50] J. von Cosel, J. Cerezo, D. Kern-Michler, C. Neumann, L. J. G. W. van Wilderen, J. Bredenbeck, F. Santoro, and I. Burghardt, "Vibrationally resolved electronic spectra including vibrational pre-excitation: Theory and application to VIPER spectroscopy," J. Chem. Phys. **147**, 164116 (2017).

[51] D. McMorrow and W. T. Lotshaw, "The frequency response of condensed-phase media to femtosecond optical pulses: spectral-filter effects," Chem. Phys. Lett. **174**, 85–94 (1990).

[52] J. D. Hybl, A. Albrecht Ferro, and D. M. Jonas, "Two-dimensional Fourier transform electronic spectroscopy," J. Chem. Phys. **115**, 6606–6622 (2001).

[53] J. N. Mastron and A. Tokmakoff, "Fourier transform fluorescence-encoded infrared spectroscopy," J. Phys. Chem. A **122**, 554–562 (2018).

[54] L. Whaley-Mayda, S. B. Penwell, and A. Tokmakoff, "Fluorescence-encoded infrared spectroscopy: Ultrafast vibrational spectroscopy on small ensembles of molecules in solution," J. Phys. Chem. Lett. **10**, 1967–1972 (2019).

[55] K. H. Drexhage, "Structure and properties of laser dyes," in *Dye Lasers*, edited by F. P. Schäfer (Springer Berlin Heidelberg, Berlin, Heidelberg, 1973) pp. 144–193.

[56] X. Liu, J. M. Cole, P. G. Waddell, T.-C. Lin, J. Radia, and A. Zeidler, "Molecular origins of optoelectronic properties in coumarin dyes: Toward designer solar cell and laser applications," J. Phys. Chem. A **116**, 727–737 (2012).

[57] U. Fano, “Effects of configuration interaction on intensities and phase shifts,” Phys. Rev. **124**, 1866–1878 (1961).

[58] D. Axelrod, “Carbocyanine dye orientation in red cell membrane studied by microscopic fluorescence polarization,” Biophys. J. **26**, 557–573 (1979).

[59] K. Bahlmann and S. Hell, “Depolarization by high aperture focusing,” Appl. Phys. Lett. **77**, 612–614 (2000).

[60] T. Tao, “Time-dependent fluorescence depolarization and Brownian rotational diffusion coefficients of macromolecules,” Biopolymers **8**, 609–632 (1967).

[61] B. J. Berne and R. Pecora, *Dynamic light scattering: with applications to chemistry, biology, and physics* (Courier Corporation, 2000).

[62] A. Tokmakoff, “Orientational correlation functions and polarization selectivity for nonlinear spectroscopy of isotropic media. I. Third order,” J. Chem. Phys. **105**, 1–12 (1996).

[63] M. Lettenberger, F. Emmerling, N. Gottfried, and A. Laubereau, “Orientational motion of anthracene in liquid solution studied by IR/UV double-resonance spectroscopy,” Chem. Phys. Lett. **240**, 324–329 (1995).

[64] M.-L. Horng, J. A. Gardecki, and M. Maroncelli, “Rotational dynamics of coumarin 153: time-dependent friction, dielectric friction, and other nonhydrodynamic effects,” J. Phys. Chem. A **101**, 1030–1047 (1997).

[65] G. B. Dutt and S. Raman, “Rotational dynamics of coumarins: An experimental test of dielectric friction theories,” J. Chem. Phys. **114**, 6702–6713 (2001).

Supplementary Material for:

Multimode vibrational dynamics and orientational effects in fluorescence-encoded infrared spectroscopy. II. Analysis of early-time signals

Lukas Whaley-Mayda[†], Abhirup Guha[†], and Andrei Tokmakoff[†*]

[†]Department of Chemistry, James Franck Institute, and Institute for Biophysical
Dynamics, The University of Chicago, Illinois 60637, United States
[*]Corresponding Author: Email: tokmakoff@uchicago.edu

Contents

S1 Finite-pulse response function calculations **3**
- S1.1 Mixed time-ordering in the response function convolution integrals . . . 3
- S1.2 Pulse characteristics . . . 8
- S1.3 Numerical evaluation by Monte Carlo integration . . . 10
  - S1.3.1 Two-pulse signal . . . 11
  - S1.3.2 Three-pulse signal and FEIR spectrum . . . 13

S2 Lineshape distortions during pulse-overlap **14**

S3 Signal processing for three-pulse Fourier transform experiments **15**

S4 Vibrationally-nonresonant IR + visible two-photon absorption (TPA) **18**
- S4.1 Modelling TPA fluorescence in FEIR experiments . . . 18
- S4.2 Frequency-resolved TPA signal and dependence on pulse durations and IR spectral phase . . . 20
- S4.3 Presence of TPA artifacts in coumarin experiments . . . 22

S5 Temporal pulse characterization and instrument response **23**
- S5.1 IR pulse characterization by interferometric autocorrelation . . . 23
- S5.2 IR/Vis temporal pulse overlap characterized by TPA . . . 24

S6 Coumarin series τ_{enc}-dependent FEIR data with ω_{IR} = 1620 cm^{-1} **27**

S7 Fitting of C6 and C343 FTIR spectra **32**

S8 C6 DFT-calculated transition dipole orientations **32**

S9 Calculated C6 FEIR spectra with flipped ν_{R1} FC factor sign **33**

S10 C343 DFT normal modes **34**

S11 C343 coherence and population features **36**

S12 Effect of chirped IR pulses in C6 and C343 simulations. **38**

S1 Finite-pulse response function calculations

S1.1 Mixed time-ordering in the response function convolution integrals

As discussed in Paper I, calculating the final target population, and hence FEIR signal, generated by finite-duration pulses requires evaluating the multiple convolution integrals against the response function

$$\bar{N}^{(4)} \equiv \lim_{t\to\infty} N^{(4)}(t) = \int_{-\infty}^{\infty} dt_4 \int_0^{\infty} d\tau_3 \int_0^{\infty} d\tau_2 \int_0^{\infty} d\tau_1 \, R^{(4)}(\tau_3, \tau_2, \tau_1) \\ \times E(t_4)E(t_4-\tau_3)E(t_4-\tau_3-\tau_2)E(t_4-\tau_3-\tau_2-\tau_1). \tag{S1}$$

Here we have reverted to the most general case where the four fields in the product each represent the sum of all pulses, in order to allow for all possible time-orderings to contribute to the response (cf. Eq. 8 in Paper I). For simplicity of notation we have suppressed the tensorial nature of the response function and electric fields vectors.

The perturbation-theoretic delays τ_i in this expression are fully time-ordered, e.g. the τ_2 interval must always proceed the τ_1 interval etc., regardless of the sequence of the pulse envelopes. To separate the different time-ordered contributions permitted for an arbitrary set of inter-pulse delays and durations, we will recast the integration in terms of partially time-ordered "pulse-specific" light-matter interaction time variables (Figure S1).[1] First, to avoid confusion between the identities of each pulse when considering their different possible orderings, we will rename each pulse electric field in the sequence as follows: the IR pulse from the moving arm of the interferometer $E_1 \equiv E_a$, the IR pulse from the stationary arm $E_2 \equiv E_b$, and the visible encoding pulse $E_3 \equiv E_c$. The total electric field is given by

$$E(t) = E_c(t) + E_b(t+\tau_{\text{enc}}) + E_a(t+\tau_{\text{enc}}+\tau_{\text{IR}}). \tag{S2}$$

As shown in Figure S1, the pulse-specific interaction delay τ_α for $\alpha = a, b, c$ specifies the time-delay between the perturbation-theoretic light-matter interaction facilitated by pulse E_α and the final interaction with the encoding pulse E_c at time t_4. Each pulse-specific delay is causally restricted to positive values, however they can assume any relative ordering among themselves. The final interaction time t_4 is not a causally restricted interval, and occurs anywhere within the profile of E_c. The relationship between these pulse-specific interaction delays and the conventional, fully-time-ordered variables t_i and τ_i introduced early are shown in Figure S1a in the case of a well-separated, properly-ordered pulse sequence.

Two IR and two visible light-matter interactions are always required in FEIR, so the product of real-valued electric fields in Eq. S1 can be written in terms of pulse-specific delays as

$$E_c(t_4)E_c(t_4-\tau_c)E_b(t_4+\tau_{\text{enc}}-\tau_b)E_a(t_4+\tau_{\text{enc}}+\tau_{\text{IR}}-\tau_a). \tag{S3}$$

Specifically, this field product describes the three-pulse signal $F_{12}(\tau_{\text{IR}}, \tau_{\text{enc}})$ where each of the two IR pulses contributes one interaction. However, as the two IR pulses are identical copies, to calculate the two-pulse signal we can simply set $\tau_{\text{IR}} = 0$ in Eq. S3 (i.e. using Eq. 16 in Paper I). With the pulse-specific time variables, this field product handles all possible time-orderings of light-matter interactions allowed by the resonance conditions and system level structure. The task of keeping track of these different time-orderings is in turn accorded to the response function and will be tackled next.

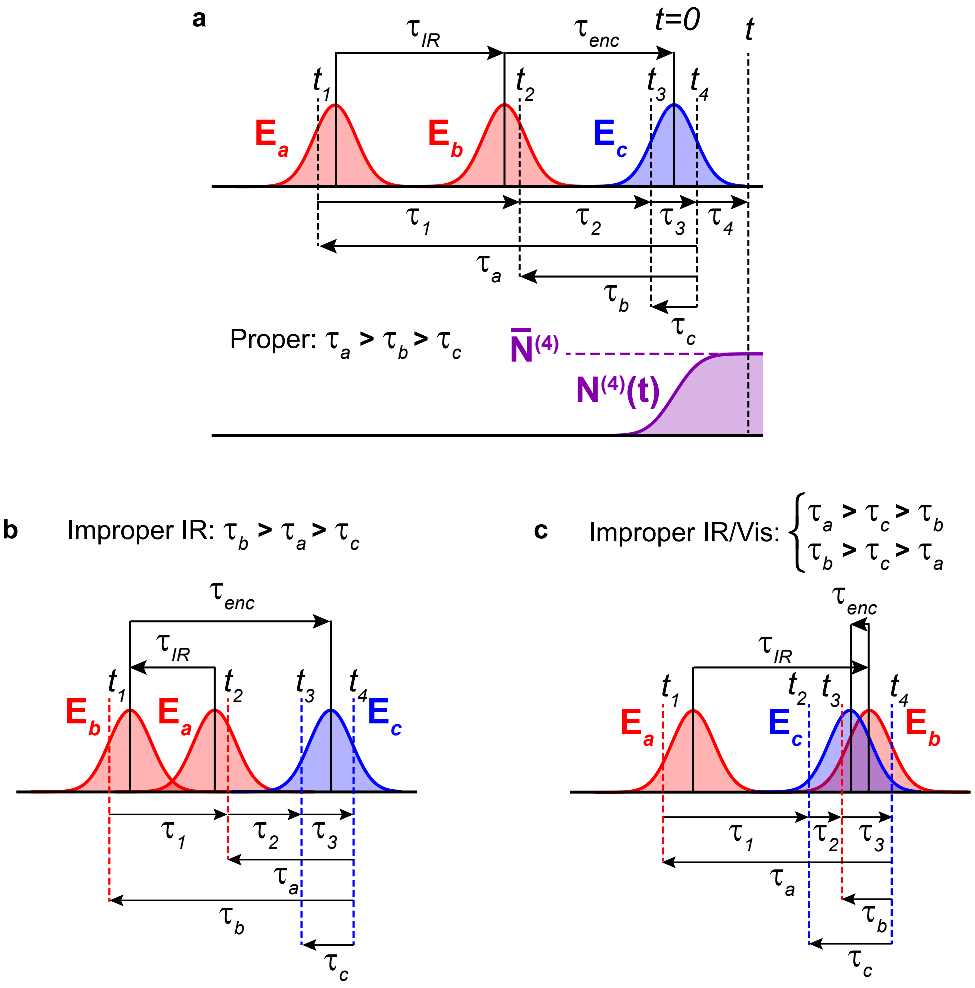

Figure S1: Pulse-specific interaction time variables τ_α and their relationship to the fully time-ordered light-matter interaction times t_i and time-delays τ_i. (a) Relationship between all sets of time variables in the properly time-ordered case $\tau_a < \tau_b < \tau_c$ with well-separated pulses obeying $\tau_{\text{IR}} > 0$ and $\tau_{\text{enc}} > 0$. (b) Improperly-ordered IR interactions $\tau_b < \tau_a < \tau_c$ with $\tau_{\text{IR}} < 0$. (c) Improperly-ordered IR-vis-IR-vis interaction when $|\tau_{\text{enc}}| < \tau_p$, where τ_p is the longer of the IR and visible pulses. Specifically shown is the case $\tau_a > \tau_c > \tau_b$ with $\tau_{\text{enc}} < 0$ and $\tau_{\text{IR}} > |\tau_{\text{enc}}|$.

To apply the rotating wave approximation (RWA) we decompose each real-valued pulse electric field into its complex positive and negative frequency components

$$E_\alpha(t) = E_\alpha^+(t) + E_\alpha^-(t), \tag{S4a}$$

$$E_\alpha^+(t) = \frac{1}{2} e_\alpha(t) e^{-i\omega_\alpha t}, \tag{S4b}$$

$$E_\alpha^-(t) = (E_\alpha^+)^*, \tag{S4c}$$

where ω_α is the center frequency, $e_\alpha(t)$ is the (in general complex) pulse envelope, and $\alpha = a, b, c$.

Specifically,

$$\omega_a = \omega_b = \omega_{\text{IR}}, \tag{S5}$$

$$\omega_c = \omega_{\text{vis}}. \tag{S6}$$

The specific characteristics of these fields, including temporal profile, spectrum, and spectral phase, are described in Section S1.2.

Expanding each real-valued field in Eq. S3 into its pair of counter-rotating complex parts via Eq. S4 yields $2^4 = 16$ terms. Our analysis of the FEIR response function in Paper I established that each pathway must involve four absorptive interactions: one bra/ket-side pair resonant with the IR and the other bra/ket-side pair resonant with the visible. As a result there are only two unique choices (up to complex conjugation) of the product of four complex fields that can contribute within the RWA, which we will term E_{I} and E_{II}:

$$\begin{aligned} E_{\text{I}}(\tau_{\text{IR}}, \tau_{\text{enc}}, t_4, \tau_c, \tau_b, \tau_a) &\equiv E_c^+(t_4)E_c^-(t_4 - \tau_c)E_b^-(t_4 + \tau_{\text{enc}} - \tau_b)E_a^+(t_4 + \tau_{\text{enc}} + \tau_{\text{IR}} - \tau_a) \\ &= e_c(t_4)e_c^*(t_4 - \tau_c)e_b^*(t_4 + \tau_{\text{enc}} - \tau_b)e_a(t_4 + \tau_{\text{enc}} + \tau_{\text{IR}} - \tau_a) \\ &\qquad \times e^{-i\omega_{\text{vis}}\tau_c} e^{i\omega_{\text{IR}}(\tau_a - \tau_b)} e^{-i\omega_{\text{IR}}\tau_{\text{IR}}}, \end{aligned} \tag{S7a}$$

$$\begin{aligned} E_{\text{II}}(\tau_{\text{IR}}, \tau_{\text{enc}}, t_4, \tau_c, \tau_b, \tau_a) &\equiv E_c^-(t_4)E_c^+(t_4 - \tau_c)E_b^-(t_4 + \tau_{\text{enc}} - \tau_b)E_a^+(t_4 + \tau_{\text{enc}} + \tau_{\text{IR}} - \tau_a) \\ &= e_c^*(t_4)e_c(t_4 - \tau_c)e_b^*(t_4 + \tau_{\text{enc}} - \tau_b)e_a(t_4 + \tau_{\text{enc}} + \tau_{\text{IR}} - \tau_a) \\ &\qquad \times e^{i\omega_{\text{vis}}\tau_c} e^{i\omega_{\text{IR}}(\tau_a - \tau_b)} e^{-i\omega_{\text{IR}}\tau_{\text{IR}}}. \end{aligned} \tag{S7b}$$

These field combinations differ in the ordering of the two oppositely-signed encoding field carriers.

The total response $\bar{N}^{(4)}(\tau_{\text{IR}}, \tau_{\text{enc}})$ is then expressed as the sum of the two real-valued contributions which result from these two field combinations

$$\bar{N}^{(4)}(\tau_{\text{IR}}, \tau_{\text{enc}}) = \bar{N}_{\text{I}}^{(4)}(\tau_{\text{IR}}, \tau_{\text{enc}}) + \bar{N}_{\text{II}}^{(4)}(\tau_{\text{IR}}, \tau_{\text{enc}}), \tag{S8a}$$

$$\begin{aligned} \bar{N}_{\text{I}}^{(4)}(\tau_{\text{IR}}, \tau_{\text{enc}}) = \int_{-\infty}^{\infty} dt_4 \int_0^{\infty} d\tau_c \int_0^{\infty} d\tau_b \int_0^{\infty} d\tau_a \\ \times S_{\text{I}}^{(4)}(\tau_c, \tau_b, \tau_a) E_{\text{I}}(\tau_{\text{IR}}, \tau_{\text{enc}}, t_4, \tau_c, \tau_b, \tau_a) + c.c., \end{aligned} \tag{S8b}$$

$$\begin{aligned} \bar{N}_{\text{II}}^{(4)}(\tau_{\text{IR}}, \tau_{\text{enc}}) = \int_{-\infty}^{\infty} dt_4 \int_0^{\infty} d\tau_c \int_0^{\infty} d\tau_b \int_0^{\infty} d\tau_a \\ \times S_{\text{II}}^{(4)}(\tau_c, \tau_b, \tau_a) E_{\text{II}}(\tau_{\text{IR}}, \tau_{\text{enc}}, t_4, \tau_c, \tau_b, \tau_a) + c.c. \end{aligned} \tag{S8c}$$

The "mixed" response functions $S_{\text{I}}^{(4)}$ and $S_{\text{II}}^{(4)}$ (explicit expressions given in Eq. S9) are piece-wise functions of the different time-orderings of pulse-specific delays that account for the switching between pathways depending on the sequentiality of field interactions. Table S1 summarizes the "recipe" for their construction in terms of the correlation functions and fully time-ordered interaction delays, while Figure S2 shows every double-sided Feynman diagram (excluding complex conjugates) contributing to $\bar{N}_{\text{I}}^{(4)}$ and $\bar{N}_{\text{II}}^{(4)}$ for the single-oscillator system discussed in Section IIIB of Paper I.

In general, there are 6 permutations for ordering the delays τ_a, τ_b, and τ_c. We will first consider the two orderings in which both IR interactions precede the visible encoding interactions. The *abc* ordering, i.e. $\tau_a > \tau_b > \tau_c$, represents the "proper" sequence of interaction which occurs for

Interaction order	RWA conjugate to E_{I}	RWA conjugate to E_{II}	τ_1	τ_2	τ_3
$\tau_a \geq \tau_b \geq \tau_c$	$C_2(\tau_3, \tau_2, \tau_1)$	$C_1(\tau_3, \tau_2, \tau_1)$	$\tau_a - \tau_b$	$\tau_b - \tau_c$	τ_c
$\tau_b > \tau_a \geq \tau_c$	$C_1^*(\tau_3, \tau_2, \tau_1)$	$C_2^*(\tau_3, \tau_2, \tau_1)$	$\tau_b - \tau_a$	$\tau_a - \tau_c$	τ_c
$\tau_a \geq \tau_c > \tau_b$	0	$C_3(\tau_3, \tau_2, \tau_1)$	$\tau_a - \tau_c$	$\tau_c - \tau_b$	τ_b
$\tau_b > \tau_c \geq \tau_a$	$C_3^*(\tau_3, \tau_2, \tau_1)$	0	$\tau_b - \tau_c$	$\tau_c - \tau_a$	τ_a
$\tau_c \geq \tau_a > \tau_b$	0	0	$\tau_c - \tau_a$	$\tau_a - \tau_b$	τ_b
$\tau_c > \tau_b > \tau_a$	0	0	$\tau_c - \tau_b$	$\tau_b - \tau_a$	τ_a

Table S1: RWA conjugated pathways for each pulse interaction order and their corresponding time arguments in terms of pulse interaction delays.

well-separated pulses with $\tau_{\mathrm{IR}} > 0$ and $\tau_{\mathrm{enc}} > 0$ (Figure S1a). Measuring Fourier transform FEIR spectra via the three-pulse signal uses one-sided time-domain data with $\tau_{\mathrm{IR}} > 0$, so this situation reflects the dominant ordering, and is the only ordering that needs to be considered in the impulsive limit. For this ordering, contribution I is comprised of rephasing pathways (C_2), while contribution II is non-rephasing (C_1). This can be seen, for example, by inspection of the diagrams in Figure S2. The *bac* ordering, i.e. the "improper IR" ordering when the stationary IR pulse E_b contributes the first interaction, dominates for $\tau_{\mathrm{IR}} < 0$ (Figure S1b). As stated above, the $\tau_{\mathrm{IR}} < 0$ range is not used when processing three-pulse data, because the τ_1 and τ_2 evolution periods are being varied simultaneously. However, the *bac* ordering does contribute to the measured signal within the IR pulse-pair overlap region when $0 < \tau_{\mathrm{IR}} \lesssim \tau_{p,a} = \tau_{p,b}$, and therefore cannot be ignored. Here the rephasing/non-rephasing identity of I and II are switched, as the ordering of the two IR interactions are reversed (Figure S2).

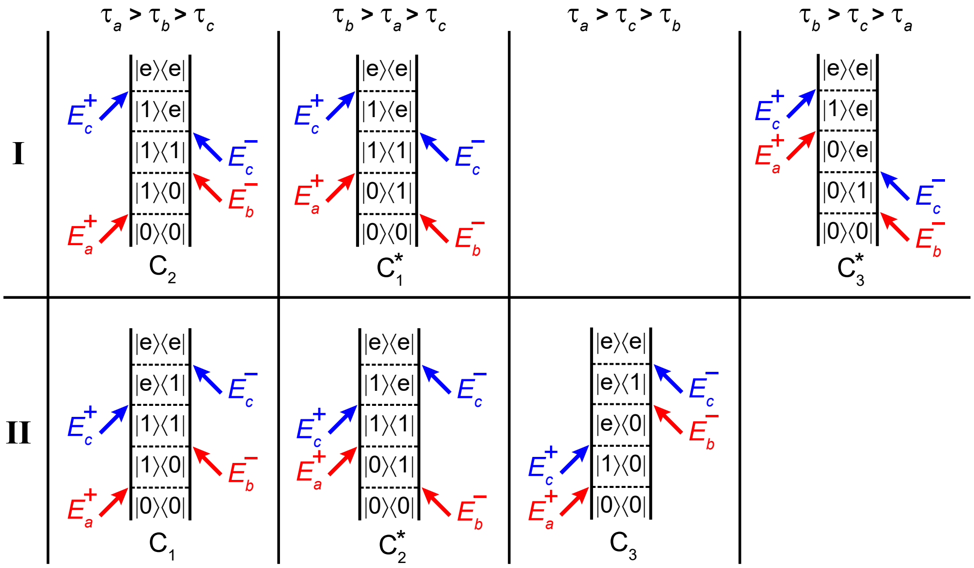

Figure S2: Diagrams (excluding complex conjugates) for all contributing orderings of light-matter interactions for a three-level system. For a generic multimode system more diagrams exist within each correlation function, but this general structure holds.

Next, we have the two mixed IR-Vis-IR-Vis orderings *acb* and *bca*. Both orderings can only occur during IR/Vis pulse overlap, i.e. for $|\tau_\mathrm{enc}| \lesssim \tau_p$ (Figure S1c). Both involve the double-quantum coherence correlation function C_3, which is a fundamentally different kind of excitation pathway compared to the proper FEIR pathways C_1 and C_2. Importantly, because the two visible interactions occur with the same pulse but are not directly sequential, the system evolution periods are no longer simply connected to the experimentally-controlled inter-pulse delays. As we will see, these contributions will generally not survive the convolution integrals under typical conditions. Finally, the orderings *cab* and *cba* involve the visible field interacting first, and therefore do not contribute under FEIR resonance conditions and can be ignored. For completeness, we give explicit expressions for the mixed response functions below:

$$S_\mathrm{I}^{(4)}(\tau_c, \tau_b, \tau_a) = \frac{1}{\hbar^4} \begin{cases} C_2(\tau_c, \tau_b - \tau_c, \tau_a - \tau_b) & \tau_a > \tau_b > \tau_c \\ C_1^*(\tau_c, \tau_a - \tau_c, \tau_b - \tau_a) & \tau_b > \tau_a > \tau_c \\ 0 & \tau_a > \tau_c > \tau_b \\ C_3^*(\tau_b, \tau_c - \tau_b, \tau_a - \tau_c) & \tau_c > \tau_a > \tau_b \\ 0 & \tau_c > \tau_a > \tau_b \\ 0 & \tau_c > \tau_b > \tau_a \end{cases}, \tag{S9a}$$

$$S_\mathrm{II}^{(4)}(\tau_c, \tau_b, \tau_a) = \frac{1}{\hbar^4} \begin{cases} C_1(\tau_c, \tau_b - \tau_c, \tau_a - \tau_b) & \tau_a > \tau_b > \tau_c \\ C_2^*(\tau_c, \tau_a - \tau_c, \tau_b - \tau_a) & \tau_b > \tau_a > \tau_c \\ C_3(\tau_b, \tau_c - \tau_b, \tau_a - \tau_c) & \tau_a > \tau_c > \tau_b \\ 0 & \tau_c > \tau_a > \tau_b \\ 0 & \tau_c > \tau_a > \tau_b \\ 0 & \tau_c > \tau_b > \tau_a \end{cases}. \tag{S9b}$$

The positive-valued integration ranges of the τ_α enforce causality, so the usual Heaviside step-functions do not need to be included.

The RWA is fully incorporated in the integrands of the I and II contributions. For example, we can see this by considering the explicit expression for contribution I

$$\begin{aligned} \bar{N}_\mathrm{I}^{(4)}(\tau_\mathrm{IR}, \tau_\mathrm{enc}) = e^{-i\omega_\mathrm{IR}\tau_\mathrm{IR}} & \int_{-\infty}^{\infty} dt_4 \int_0^\infty d\tau_c \int_0^\infty d\tau_b \int_0^\infty d\tau_a \\ & \times S_\mathrm{I}^{(4)}(\tau_c, \tau_b, \tau_a) e^{-i\omega_\mathrm{vis}\tau_c} e^{i\omega_\mathrm{IR}(\tau_a - \tau_b)} \\ & \times e_c(t_4) e_c^*(t_4 - \tau_c) e_b^*(t_4 + \tau_\mathrm{enc} - \tau_b) e_a(t_4 + \tau_\mathrm{enc} + \tau_\mathrm{IR} - \tau_a) + c.c., \end{aligned} \tag{S10}$$

and specifically examining the *abc* time-ordering where $S_\mathrm{I}^{(4)}(\tau_c, \tau_b, \tau_a) = C_2(\tau_c, \tau_b - \tau_c, \tau_a - \tau_b)$. For the three-level system discussed in Section IIIB of Paper I this correlation function oscillates as $\exp[i(\omega_{e0} - \omega_{10})\tau_c - i\omega_{10}(\tau_a - \tau_b)]$, while the complex field phase-factors oscillate as $\exp[-i\omega_\mathrm{vis}\tau_c + i\omega_\mathrm{IR}(\tau_a - \tau_b)]$. On resonance when $\omega_\mathrm{IR} \approx \omega_{10}$ and $\omega_\mathrm{vis} \approx \omega_{e0} - \omega_{10}$, these complex phase oscillations approximately cancel out, leaving behind a slowly varying function of the integration variables that therefore survives the integration.

We also note that Eq. S10 (and the analogous expression for $\bar{N}_\mathrm{II}^{(4)}(\tau_\mathrm{IR}, \tau_\mathrm{enc})$) is modulated by the

IR carrier phase $\omega_{\text{IR}}\tau_{\text{IR}}$ outside of the integrals, which reflects the interferometric excitation by the IR pulse-pair. Explicitly, we can write these expressions for $m = \text{I}$ or II as

$$\bar{N}_m^{(4)}(\tau_{\text{IR}}, \tau_{\text{enc}}) = \mathcal{N}_m^{(4)}(\tau_{\text{IR}}, \tau_{\text{enc}})e^{-i\omega_{\text{IR}}\tau_{\text{IR}}} + \left(\mathcal{N}_m^{(4)}(\tau_{\text{IR}}, \tau_{\text{enc}})\right)^* e^{i\omega_{\text{IR}}\tau_{\text{IR}}} \tag{S11a}$$

where

$$\begin{aligned}\mathcal{N}_{\text{I}}^{(4)}(\tau_{\text{IR}}, \tau_{\text{enc}}) = \int_{-\infty}^{\infty} dt_4 \int_0^{\infty} d\tau_c \int_0^{\infty} d\tau_b \int_0^{\infty} d\tau_a \\ \times S_{\text{I}}^{(4)}(\tau_c, \tau_b, \tau_a)e^{-i\omega_{\text{vis}}\tau_c}e^{i\omega_{\text{IR}}(\tau_a-\tau_b)} \\ \times e_c(t_4)e_c^*(t_4-\tau_c)e_b^*(t_4+\tau_{\text{enc}}-\tau_b)e_a(t_4+\tau_{\text{enc}}+\tau_{\text{IR}}-\tau_a)\end{aligned} \tag{S11b}$$

$$\begin{aligned}\mathcal{N}_{\text{II}}^{(4)}(\tau_{\text{IR}}, \tau_{\text{enc}}) = \int_{-\infty}^{\infty} dt_4 \int_0^{\infty} d\tau_c \int_0^{\infty} d\tau_b \int_0^{\infty} d\tau_a \\ \times S_{\text{II}}^{(4)}(\tau_c, \tau_b, \tau_a)e^{i\omega_{\text{vis}}\tau_c}e^{i\omega_{\text{IR}}(\tau_a-\tau_b)} \\ \times e_c^*(t_4)e_c(t_4-\tau_c)e_b^*(t_4+\tau_{\text{enc}}-\tau_b)e_a(t_4+\tau_{\text{enc}}+\tau_{\text{IR}}-\tau_a).\end{aligned} \tag{S11c}$$

These functions $\mathcal{N}_m^{(4)}(\tau_{\text{IR}}, \tau_{\text{enc}})$ can be interpreted as the complex analytic envelopes of the $m = \text{I}$ or II contributions to the three-pulse signal. In practice, to calculate the three-pulse signal we therefore only calculate its complex envelope,

$$\mathcal{N}^{(4)}(\tau_{\text{IR}}, \tau_{\text{enc}}) = \sum_{m=\text{I,II}} \mathcal{N}_m^{(4)}(\tau_{\text{IR}}, \tau_{\text{enc}}), \tag{S12}$$

which evolves slowly in τ_{IR} and can therefore be sampled much more sparsely. Specifically, the sampling interval only needs to be Nyquist for the difference frequency between the highest and lowest frequency features in the response. This corresponds to working in a 'fully-rotating' frame where the carrier ω_{IR} is referenced to zero.[2–4] For the two-pulse signal, $\tau_{\text{IR}} = 0$ and the envelope is real with $\bar{N}^{(4)}(\tau_{\text{enc}}) = 2\mathcal{N}^{(4)}(\tau_{\text{enc}})$.

S1.2 Pulse characteristics

We will define our pulses in the frequency domain as

$$\tilde{E}_\alpha(\omega) = A_\alpha(\omega)e^{i\Phi_\alpha(\omega)}, \tag{S13}$$

where $A_\alpha(\omega)$ and $\Phi_\alpha(\omega)$ are real-valued functions describing the spectral amplitude and phase of pulse $\alpha = a, b,$ or c, respectively. The frequency- and time-domain representations of the pulse electric fields are related by Fourier transformation

$$\tilde{E}_\alpha(\omega) = \int_{-\infty}^{\infty} E_\alpha(t)e^{i\omega t}dt, \tag{S14a}$$

$$E_\alpha(t) = \frac{1}{2\pi}\int_{-\infty}^{\infty} \tilde{E}_\alpha(\omega)e^{-i\omega t}d\omega. \tag{S14b}$$

The pulse spectrum is defined as the field's frequency-domain power spectrum

$$|\tilde{E}_\alpha(\omega)|^2 = A_\alpha(\omega)^2. \tag{S15}$$

The reality of the time-domain electric field imposes the condition

$$\tilde{E}_\alpha(\omega) = \tilde{E}^*_\alpha(-\omega), \tag{S16}$$

and for brevity in what follows we will only explicitly address the positive frequency portion. For simplicity, we will define our pulses to have Gaussian spectra with spectral bandwidth characterized by FWHM $\Delta\omega_\alpha$

$$|\tilde{E}_\alpha(\omega)|^2 = \Big(A_{\alpha,0} \exp(-2\ln(2)\,(\omega-\omega_\alpha)^2/\Delta\omega_\alpha^2)\Big)^2, \tag{S17}$$

where ω_α is the center frequency and $A_{\alpha,0}$ the spectral amplitude. The spectral phase is described by the power series expansion

$$\Phi_\alpha(\omega) = \frac{\gamma_{\alpha,2}}{2!}(\omega-\omega_\alpha)^2 + \frac{\gamma_{\alpha,3}}{3!}(\omega-\omega_\alpha)^3 + \cdots \tag{S18}$$

where $\gamma_{\alpha,2}$ and $\gamma_{\alpha,3}$ describe 2nd-order and 3rd-order dispersion, respectively. The 0th- and 1st-order terms would describe the carrier-envelope phase and a uniform temporal displacement, respectively, and are ignored.[5]

The positive frequency component $E^+_\alpha(t)$ of the time-domain field (Eq. S4) is given by the one-sided Fourier transform

$$E^+_\alpha(t) = \frac{1}{\pi}\int_0^\infty \tilde{E}_\alpha(\omega)e^{-i\omega t}d\omega, \tag{S19}$$

and is the complex analytic representation of the real time-domain electric field.[6,7] Our specific decomposition of this complex field into envelope and carrier in Eq. S4 uses the same center frequency ω_α as the spectrum. Specifically, the temporal envelope $e_\alpha(t)$ used in the simulations is calculated by

$$e_\alpha(t) = 2e^{i\omega_\alpha t}E^+_\alpha(t), \tag{S20}$$

where $E^+_\alpha(t)$ is found through numerically evaluating Eq. S19 by FFT. The temporal envelope $e_\alpha(t)$ is in general complex and can be expressed as

$$e_\alpha(t) = \mathcal{E}_\alpha(t)e^{i\phi_\alpha(t)}, \tag{S21}$$

where $\mathcal{E}_\alpha(t)$ is a real-valued temporal amplitude function and $\phi_\alpha(t)$ is a real-valued temporal phase function. Because $\mathcal{E}_\alpha(t) = 2|E^+_\alpha(t)|$, the complex analytic representation uniquely determines the temporal amplitude. However, $\phi_\alpha(t)$ is arbitrary up to an additive factor of $\omega' t$ for any shift ω', provided the carrier phase $\omega_\alpha t$ in Eq. S20 is accordingly modified by $-\omega' t$. This reflects the formally arbitrary assignment of the carrier frequency. However, it can be shown generally that defining ω_α as the mean of the $\omega > 0$ half of $|\tilde{E}_\alpha(\omega)|^2$ produces the slowest-varying complex analytic envelope $e_\alpha(t)$ in the mean-squared sense, and is therefore in some sense the 'best' choice of carrier frequency.[6,8]

If the pulse is transform-limited, i.e. the spectral phase $\Phi_\alpha(\omega) = 0$, then the temporal phase $\phi_\alpha(t) = 0$ as well, and the envelope function is real. For our Gaussian pulse spectrum this transform-limited envelope is also a Gaussian

$$e_\alpha(t) = e_{\alpha,0} \exp(-2\ln(2)\, t^2/\tau_{p,\alpha}^2), \tag{S22}$$

where the pulse duration $\tau_{p,\alpha}$ is defined as the FWHM of the intensity profile $|e_\alpha(t)|^2$ and $e_{\alpha,0}$ is the peak field amplitude.

S1.3 Numerical evaluation by Monte Carlo integration

We use a Monte Carlo integration method to evaluate the expressions in Eq. S12. Generically, this task can be characterised by evaluating the integral I of some function $f(\mathbf{X})$ over some region Ω,

$$I = \int_\Omega f(\mathbf{X}) d\mathbf{X}, \tag{S23}$$

where in general $\mathbf{X}$ is a multidimensional variable and Ω is a correspondingly multidimensional region with volume $V = \int_\Omega d\mathbf{X}$. The premise of Monte Carlo integration is to construct an estimator of this integral

$$I_N = \frac{1}{N} \sum_{i=1}^{N} \frac{f(\mathbf{X}_i)}{p(\mathbf{X}_i)} \tag{S24}$$

where $\mathbf{X}_1, \cdots, \mathbf{X}_N \in \Omega$ are points sampled from a probability distribution $p(\mathbf{X})$ defined over the integration region.[9] The probabilities $p(\mathbf{X}_i)$ in the denominator account for the bias in sampling such that, according to the law of large numbers

$$I = \lim_{N\to\infty} I_N. \tag{S25}$$

With sufficiently large N the Monte Carlo estimate I_N thereby provides a sufficiently good value for I, while a judicious choice of $p(\mathbf{X})$ can speed up the convergence.

The integration region for the multiple convolutions we wish to evaluate in Eq. S12 is composed of infinite intervals. However, the pulse envelope functions $e_\alpha(t)$ are essentially zero beyond a few multiples of the pulse duration and therefore effectively window the integrand, so we only need to sample the integration variables within these envelopes. In particular, we use the following sampling ranges

$$t_4 \in [-L\tau_{p,c},\, L\tau_{p,c}], \tag{S26a}$$

$$\tau_c \in [0,\, L\tau_{p,c}], \tag{S26b}$$

$$\tau_b \in [\max(0, -L\tau_{p,b} + \tau_{\text{enc}}),\, L\tau_{p,b} + \tau_{\text{enc}}], \tag{S26c}$$

$$\tau_a \in [\max(0, -L\tau_{p,a} + \tau_{\text{enc}} + \tau_{\text{IR}}),\, L\tau_{p,a} + \tau_{\text{enc}} + \tau_{\text{IR}}], \tag{S26d}$$

where $\tau_{p,\alpha}$ is the FWHM of pulse α's temporal intensity profile $|e_\alpha(t)|^2$, and L is a multiplier that determines how far out in the profile to sample. Within each of these ranges, the variables are drawn from truncated Gaussian distributions that roughly mimic the field envelopes. Specifically, these distributions are generated from the "parent" Normal distributions $\mathcal{N}(\mu, \sigma)$

$$t_4 : \mathcal{N}(0, \tau_{p,c}/\sqrt{\ln 2}), \tag{S27a}$$

$$\tau_c : \mathcal{N}(0, \tau_{p,c}/\sqrt{\ln 2}), \tag{S27b}$$

$$\tau_b : \mathcal{N}(\tau_{\text{enc}}, \tau_{p,b}/\sqrt{\ln 2}), \tag{S27c}$$

$$\tau_a : \mathcal{N}(\tau_{\text{enc}} + \tau_{\text{IR}}, \tau_{p,a}/\sqrt{\ln 2}), \tag{S27d}$$

which are then each truncated to within the respective ranges in Eq. S26. We note that this sampling strategy, while providing faster convergence than uniformly sampling the ranges in Eq. S26, does not actually follow the distribution of the product of pulse profiles, which would involve correlation among the variables. A more optimized sampling incorporating these correlations may further speed up convergence.

We use the value $L = 2.5$, which was used by Jonas and co-workers in their deterministic numerical integration procedure for calculating 3$^{\text{rd}}$-order signals.[1] We note that using smaller values of L produces faster convergence, as the largest regions of the integrand are being sampled more densely, however significant distortions begin to appear for $L = 1.5$ and lower. The lower range limits of the τ_α in Eq. S26 are constrained to be non-negative to enforce causality, and if the inter-pulse delays and pulse durations are such that any of their upper range limits become negative, the value of the integral is simply set to zero.

For every fixed combination of the inter-pulse delays τ_{enc} and τ_{IR} desired, N samples of the 4 integration variables τ_a, τ_b, τ_c, and t_4 are drawn from their respective distributions, and the Monte Carlo estimates of $\mathcal{N}_m^{(4)}(\tau_{\text{IR}}, \tau_{\text{enc}})$ for $m = \text{I}$ and II are computed via Eq. S24, where $f(\mathbf{X})$ represents the integrand in Eq. S11(b) or (c). In both cases the overall probability $p(\mathbf{X}_i)$ for each sampling point is the product of the four individual probabilities evaluated from the truncated Gaussian distributions. Every sample of the integration variables is first categorized by its ordering (*abc*, *bac*, etc.), which determines which piece of the mixed response functions (Eq. S9) is used to compute the integrand. The correlation functions making up the mixed response functions are expressed analytically in the homogeneous limit with the RWA conjugate field phase factors directly incorporated, and are evaluated numerically for every sample of the integration variables. The pulses electric fields are specified in the frequency domain via Eq. S13, and their envelope functions are computed numerically via FFT. The product of the envelopes is then evaluated by lookup table for each Monte Carlo sample.

S1.3.1 Two-pulse signal

Figure S3 shows an example calculation of the two-pulse signal for the single-oscillator system discussed in Sec. IIIB of Paper I using the same molecular parameters, i.e. a lifetime-broadened mode at $\omega_{10} = 1600$ cm^{-1} with 1 ps lifetime. The electronic dephasing time of the encoding transition is set to $\Gamma_{e1}^{-1} = 10$ fs. We recall that the FEIR response of this system is only composed of population pathways. The pulses are transform-limited with spectra/durations chosen to be roughly representative of the those used in experiment. The IR pulse $E_a = E_b = E_{\text{IR}}$ is set directly on resonance with $\omega_{\text{IR}} = 1600$ cm^{-1} and has $\Delta\omega_{\text{IR}} = 120$ cm^{-1} bandwidth, which produces a transform-limited duration of $\tau_{p,\text{IR}} = 123$ fs. This bandwidth is slightly narrower than the $\Delta\omega_{\text{IR}} = 140$ cm^{-1} used for the coumarin response function simulations in the main text. The visible encoding pulse $E_c = E_{\text{vis}}$ has $\Delta\omega_{\text{vis}} = 50$ cm^{-1} bandwidth resulting in a 297 fs pulse duration, and is tuned such that the encoding transition is directly on resonance.

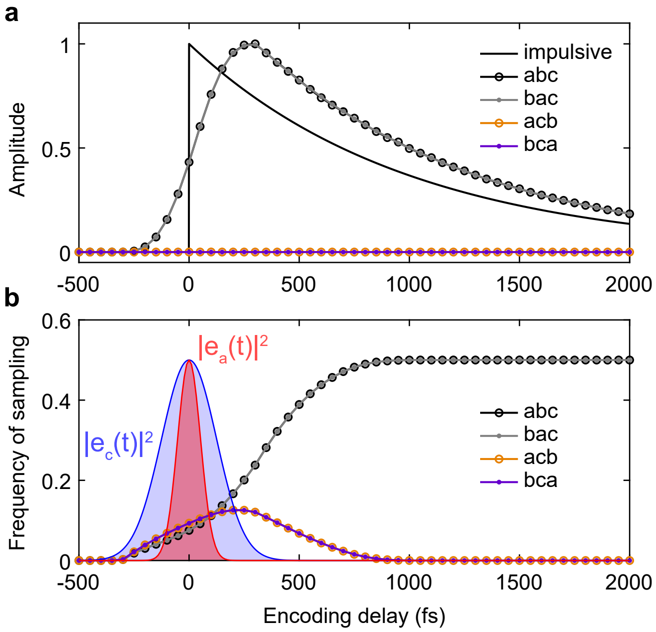

Figure S3: Finite-pulse calculation of the two-pulse signal for a single-oscillator system. (a) Relative amplitude of the abc, bac, acb, and bca time-ordered contributions to the total finite-pulse signal, with the impulsive limit signal shown for reference. (b) Relative frequency of sampling the abc, bac, acb, and bca time-orderings in evaluating the Monte Carlo estimate with $L = 2.5$. The intensity profiles of the IR pulse $|e_a(t)|^2 = |e_b(t)|^2$ and visible pulse $|e_c(t)|^2$ are overlayed at $\tau_{\text{enc}} = 0$.

Figure S3a shows the contributions of the 4 allowed time-orderings abc, bac, acb, and bca overlayed on the impulsive signal, with $N = 5 \times 10^7$ samples used for every τ_{enc} point. Because $\tau_{\text{IR}} = 0$, or equivalently because both IR interactions occur within the same IR pulse profile, the abc and bac contributions are identical within noise. Neither of the misordered IR/Vis contributions acb or bca contribute any amplitude above noise ($\sim 10^{-4}$ times the maximum abc response). The relative frequency of sampling the 4 different time-orderings are shown in Figure S3(b), with the intensity profiles of the IR and visible pulses overlayed at $\tau_{\text{enc}} = 0$ for visual reference. We note that the τ_{enc}-dependent appearance of these relative sampling frequencies is influenced by the multiplier L, and is not indicative of the weight of the different time-orderings in the signal, but merely reflects how often they are sampled by the Monte Carlo algorithm.

The full two-pulse signal is the sum over all time-orderings, and therefore resembles the abc and bac contributions. Overall, the appearance of this finite-pulse signal is consistent with the convolution of the impulsive signal with an instrument response of duration given by the temporal cross-correlation of the IR and visible intensity profiles, $\sqrt{\tau_{p,\text{IR}}^2 + \tau_{p,\text{vis}}^2} = 321$ fs. Namely, the signal rises to roughly half its maximum by $\tau_{\text{enc}} = 0$, and is peaked at $\sim$ 300 fs. Because the pulse cross-correlation is meaningfully shorter than the vibrational lifetime in this case, the decay of the signal beyond the pulse-overlap region is still a good measure of the system's population relaxation kinetics.

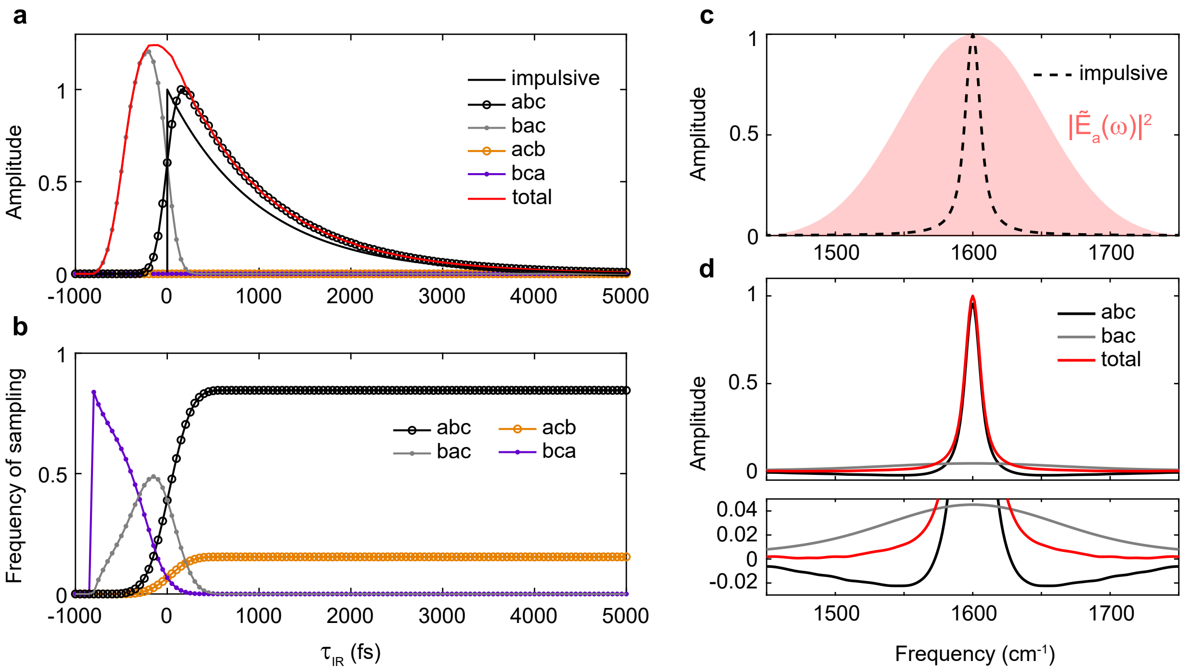

Figure S4: Finite-pulse calculation of the $\tau_{\text{enc}} = 500$ fs three-pulse signal and FEIR spectrum for the same single-mode system as Figure S3. (a) abc, bac, acb, and bca time-ordered contributions, and the total signal overlayed on the impulsive signal. (b) Relative Monte Carlo sampling frequency of the abc, bac, acb, and bca time-orderings. (c) Impulsive FEIR spectrum plotted over the IR pulse spectrum. (d) Total finite-pulse FEIR spectrum and its abc and bac contributions. The lower panel shows magnified detail around the baseline.

S1.3.2 Three-pulse signal and FEIR spectrum

Next we calculate the three-pulse signal and FEIR spectrum of the same system with the same pulses. The encoding delay is fixed at $\tau_{\text{enc}} = 500$ fs, which is beyond the bulk of the pulse-overlap region. As we will show in Section S2, spectra within the pulse-overlap region can be subject to additional lineshape distortions. Figure S4(a) shows the real part of the total three-pulse envelope $\mathcal{N}^{(4)}(\tau_{\text{IR}}, \tau_{\text{enc}})$, its decomposition into the 4 time-orderings, and the impulsive signal envelope (abc ordering only). In this specific case the envelope happens to be fully real because the IR and visible fields have symmetric spectra, are transform-limited, and are exactly on resonance with the symmetric vibrational resonance. As before, the Monte Carlo sampling frequencies of each time-ordering are shown below in Figure S4(b). Because the vibration is lifetime-broadened, i.e. the dephasing and population relaxation rates are the same $\Gamma_{10} = \Gamma_{11}$, the abc contribution to the three-pulse envelope has a similar τ_{IR}-dependence to the τ_{enc}-dependence of the two-pulse signal. As in the two-pulse case, neither of the mixed IR/Vis time-orderings acb or bca contribute any signal amplitude above noise. The bac contribution dominates for negative τ_{IR} but then falls off to zero when E_a starts arriving after E_c for $|\tau_{\text{IR}}| > \tau_{\text{enc}}$. However, a quickly decaying portion of the bac contribution does appear for positive τ_{IR} and will therefore play a role in the spectrum as discussed below.

The spectrum of the IR pulse is shown overlayed on the impulsive FEIR spectrum in Figure S4c. The finite-pulse FEIR spectrum is found by Fourier transformation of the $\tau_{\text{IR}} \geq 0$ portion of the signal. Specifically, the real part of the FFT of the one-sided complex envelope $\mathcal{N}^{(4)}(\tau_{\text{IR}} \geq 0, \tau_{\text{enc}})$

is first calculated, and then shifted up to the carrier frequency ω_{IR}. We note that in general the complex-valued nature of the time-domain envelope ensures that its frequency components can be properly assigned above or below the carrier.[3] Figure S4(d) shows the resulting FEIR spectrum as well as its decomposition into the *abc* and *bac* contributions. As the IR pulse is broadband compared to the vibrational linewidth (~11 cm^{-1}), the spectrum matches the impulsive limit very closely. The contribution of the *abc* ordering on its own almost entirely determines the spectrum. However, it has a small distortion in the form of shallow negative wings along the breadth of the pulse spectrum, as can be seen in a magnified view of the baseline region (lower panel of Figure S4(d)). This spectral distortion is caused by the delayed peak of the *abc* contribution along τ_{IR} due to the finite pulse convolutions. However, the *bac* contribution is a broad positive feature that perfectly cancels out this distortion, resulting in the proper absorptive appearance of the complete spectrum. As we will discuss in Section S2, in the IR/Vis pulse-overlap region the *abc* and *bac* contributions are mis-weighted and no longer add up to give an absorptive lineshape, leading to spectral distortions.

S2 Lineshape distortions during pulse-overlap

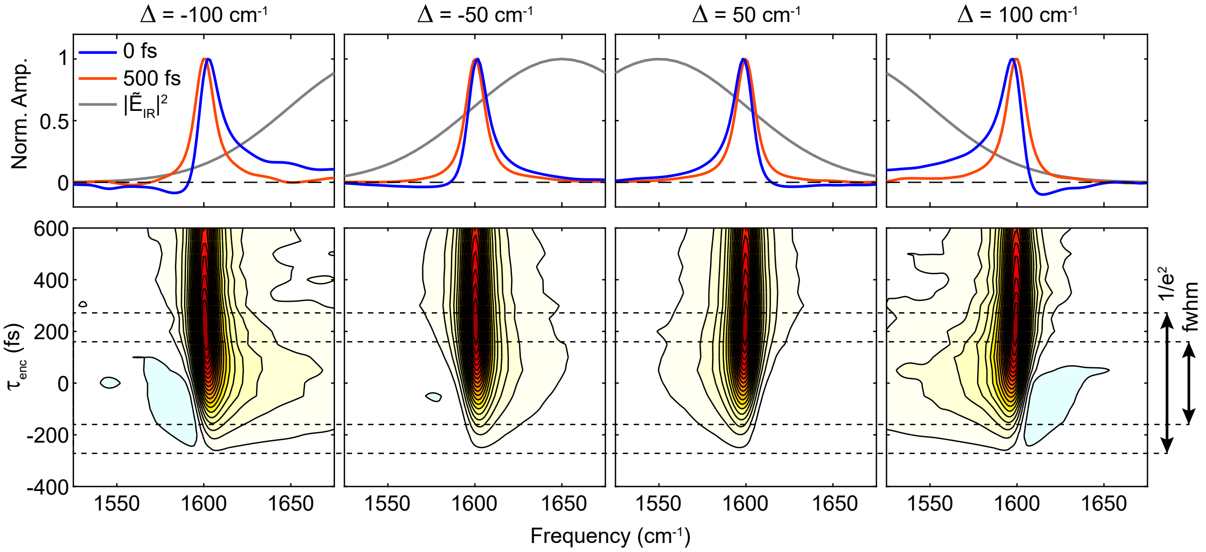

Figure S5: IR/Vis pulse-overlap lineshape phase distortion for a single-mode population feature, and its dependence on the IR-vibrational detuning $\Delta = \omega_{\mathrm{IR}} - \omega_{10}$. The upper panels show the FEIR spectrum at $\tau_{\mathrm{enc}} = 0$ fs and 500 fs overlayed on the IR pulse spectrum. Lower panels show contour plots of the full τ_{enc}-dependent FEIR spectrum, with the FWHM and 1/e^2 full-width of the IR/Vis intensity cross-correlation indicated. Contour spacing is set at 5%.

As mentioned in main text Sec. IIID, additional distortions to FEIR spectra can occur during IR/Vis pulse overlap. Here we demonstrate a specific lineshape distortion to the population features. Figure S5 shows τ_{enc}-dependent FEIR spectra of the single-mode system discussed in Sec. S1.3 with four different IR center frequencies, resulting in IR-vibrational detunings of $\Delta = \omega_{\mathrm{IR}} - \omega_{10}$ = -100, -50, 50, and 100 cm^{-1}. In each case the IR pulse is transform-limited and Gaussian with bandwidth $\Delta\omega_{\mathrm{IR}}$ = 120 cm^{-1}, and the visible pulse is likewise the same as that used previously in Secs. S1.3.1 and S1.3.2. At $\tau_{\mathrm{enc}} = 0$ the vibrational lineshape exhibits a phase twist that depends on the magnitude and sign of Δ. For Δ = -100 cm^{-1}, when the vibrational resonance is deep in the red-wing of the IR pulse spectrum, this phase distortion produces a negative/positive wing on the low/high frequency side of the band, respectively. For smaller $|\Delta|$ this phase twist becomes less extreme, while it switches sign when Δ becomes positive. This lineshape distortion is contained within the pulse overlap region, whose extent is indicated by both the IR/Vis cross-correlation FWHM ($\sqrt{\tau_{p,\mathrm{IR}}^2 + \tau_{p,\mathrm{vis}}^2} = 321$ fs) and $1/e^2$ full-width ($2w = \sqrt{2}\mathrm{FWHM}/\sqrt{\ln 2} = 546$ fs). With these pulses, the spectrum is essentially free of distortion by $\tau_{\mathrm{enc}} = 500$ fs. This type of distortion is likely at play in the carbonyl feature above 1700 cm^{-1} for C337 and C153 (Fig. S14), which are excited by the wing of the IR pulse spectrum.[10]

This apparent phase distortion in the population response is likely related to the improper weighting of the *abc* and *bac* time-ordered contributions discussed in Section S1.3, although a detailed understanding of its origins requires further investigation. Coherence features are also distorted (although not in the same way) during pulse-overlap, as can be seen e.g. in Figure 4(f) of the main text, where the amplitude near the center of the IR pulse spectrum is additionally enhanced. Overall, FEIR spectra for τ_{enc} within pulse-overlap should be approached with caution, although familiarity with the phenomenology of these artifacts should help build confidence in interpreting (or not over-interpreting) early-time data.

S3 Signal processing for three-pulse Fourier transform experiments

As discussed in Paper I, the FEIR signal in a three-pulse experiment has the following components

$$F(\tau_{\mathrm{IR}}, \tau_{\mathrm{enc}}) = F_{12}(\tau_{\mathrm{IR}}, \tau_{\mathrm{enc}}) + F_1(\tau_{\mathrm{IR}} + \tau_{\mathrm{enc}}) + F_2(\tau_{\mathrm{enc}}). \tag{S28}$$

Specifically, $F_1(\tau_{\mathrm{IR}} + \tau_{\mathrm{enc}}) = F_2(\tau_{\mathrm{enc}})$ are two-pulse signals were both IR-vibrational interactions occur with either $\mathbf{E}_1$ or $\mathbf{E}_2$, respectively, while $F_{12}(\tau_{\mathrm{IR}}, \tau_{\mathrm{enc}})$ is the three-pulse signal due to one interaction each with $\mathbf{E}_1$ and $\mathbf{E}_2$ and two with the encoding pulse $\mathbf{E}_3$.

Figure S6(a) shows the full background-subtracted time-domain FEIR signal $F(\tau_{\mathrm{IR}}, \tau_{\mathrm{enc}})$ from the C6 measurement presented in Section IV. The peak of the $F_2(\tau_{\mathrm{enc}})$ component can be seen as a horizontal stripe along $\tau_{\mathrm{enc}} = 600$ fs, while the other two-pulse component $F_1(\tau_{\mathrm{IR}} + \tau_{\mathrm{enc}})$ produces the stripe oriented along the anti-diagonal where $\tau_{\mathrm{IR}} + \tau_{\mathrm{enc}} = 600$ fs. The three-pulse signal can be made out as the rapidly oscillating component along τ_{IR}.

Figure S6(b) shows the 1D slices $F(\tau_{\mathrm{IR}}, \tau_{\mathrm{enc}} = 600\,\mathrm{fs})$, $F(\tau_{\mathrm{IR}} = 0\,\mathrm{fs}, \tau_{\mathrm{enc}})$ (the two-pulse signal measured with the superposed pulse-pair), and $F(\tau_{\mathrm{IR}}, \tau_{\mathrm{enc}} = -600\,\mathrm{fs})$ (only capturing the F_1 two-pulse signal). Comparing these latter two versions of the two-pulse signal shows the 4:1 amplitude ratio expected based on constructive interference (ratio of blue to orange arrow sizes in panel (b)) as referenced in Section IIIA of Paper I. Figure S6(c) shows the FEIR spectrum processed from the three-pulse signal, as described next. The projection of this τ_{enc}-dependent spectrum onto the τ_{enc} axis overlays with the independently measured two-pulse signal, demonstrating the projection-slice relationship between these quantities.

When performing a three-pulse FEIR experiment, an IR reference (from the out of phase output, or dark arm, of the Mach-Zehnder interferometer (MZI)) is collected either immediately before or after collecting the FEIR signal. Figure S7(a)-(c) shows an example of the raw time-domain three-pulse FEIR data with $\tau_{\mathrm{enc}} = 600$ fs with the corresponding IR reference. The F_{tot} level at the far positive end of the τ_{IR} scan range is subtracted off to remove the $F_0 + B$ background and

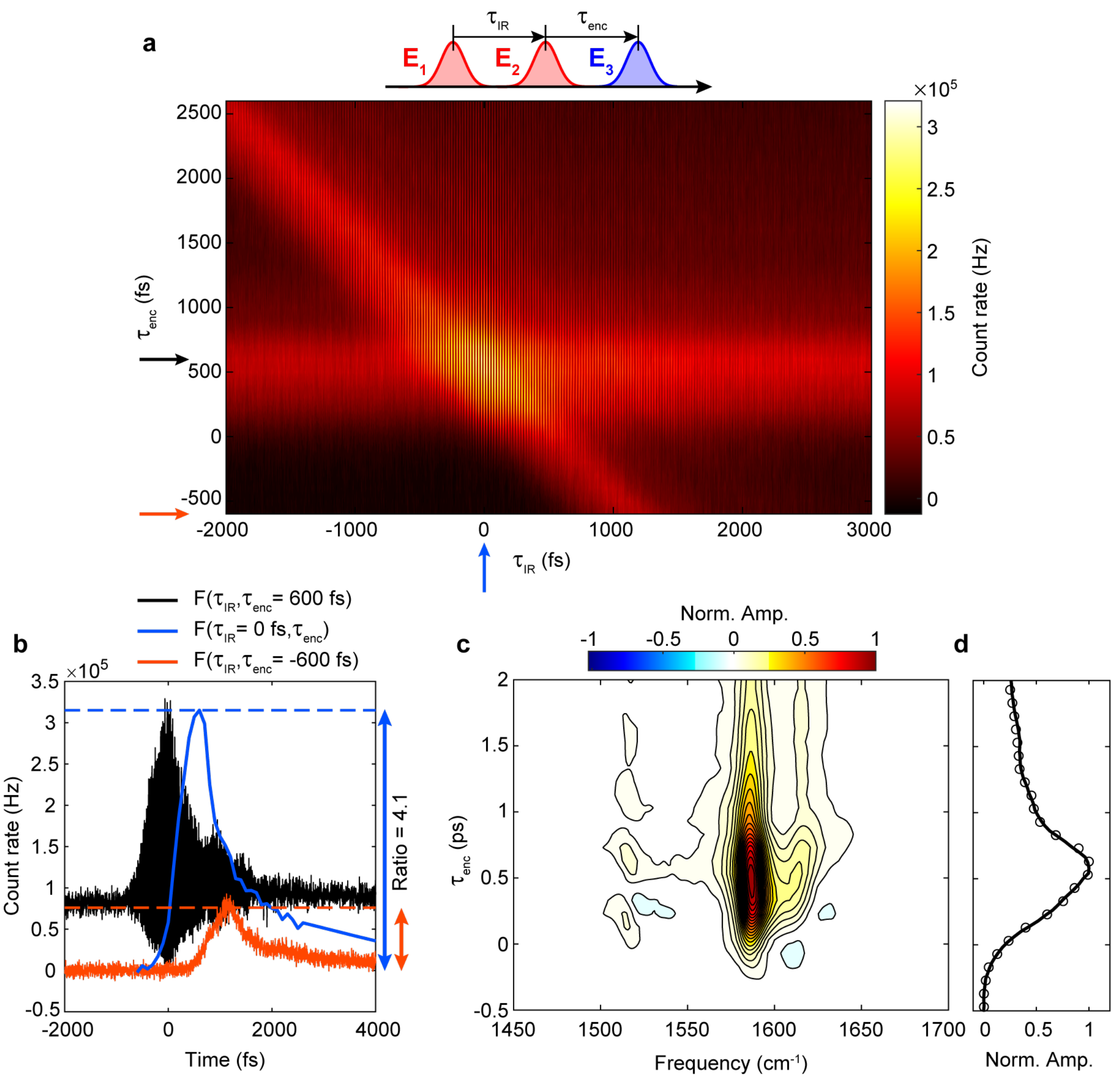

Figure S6: Signal contributions in a three-pulse experiment and projection slice relationship. (a) Background-subtracted FEIR signal $F(\tau_{\text{IR}}, \tau_{\text{enc}})$ from C6. (b) Various 1D slices of the FEIR signal, indicated by color-coded arrows in (a). (c) Processed FEIR spectrum and (d) projection of the spectrum onto the τ_{enc} axis (black circles). The two-pulse signal is overlayed (solid black) to illustrate the projection-slice relationship between these quantities.

constant F_2 two-pulse signal. Next, the phase extracted from the IR reference is used to determine the absolute timing between the IR pulse-pair in a similar manner to pump-probe geometry 2D IR spectroscopy experiments.[11–13] In practice, both FEIR and IR channels are Fourier transformed after having been appropriately apodized, zero-padded, and rotated to an approximate time zero bin in the τ_{IR} axis. The frequency domain FEIR data is divided by the complex phase factor from the IR reference and transformed back to the time domain, where the now correctly assigned negative τ_{IR} data is removed. A final FT of the one-sided data produces the FEIR spectrum as its real part (Figure S7(d)), where the other two-pulse signal F_1 has been filtered to the zero-frequency band. For τ_{enc}-dependent three-pulse experiments, this process is done for each step of τ_{enc} using

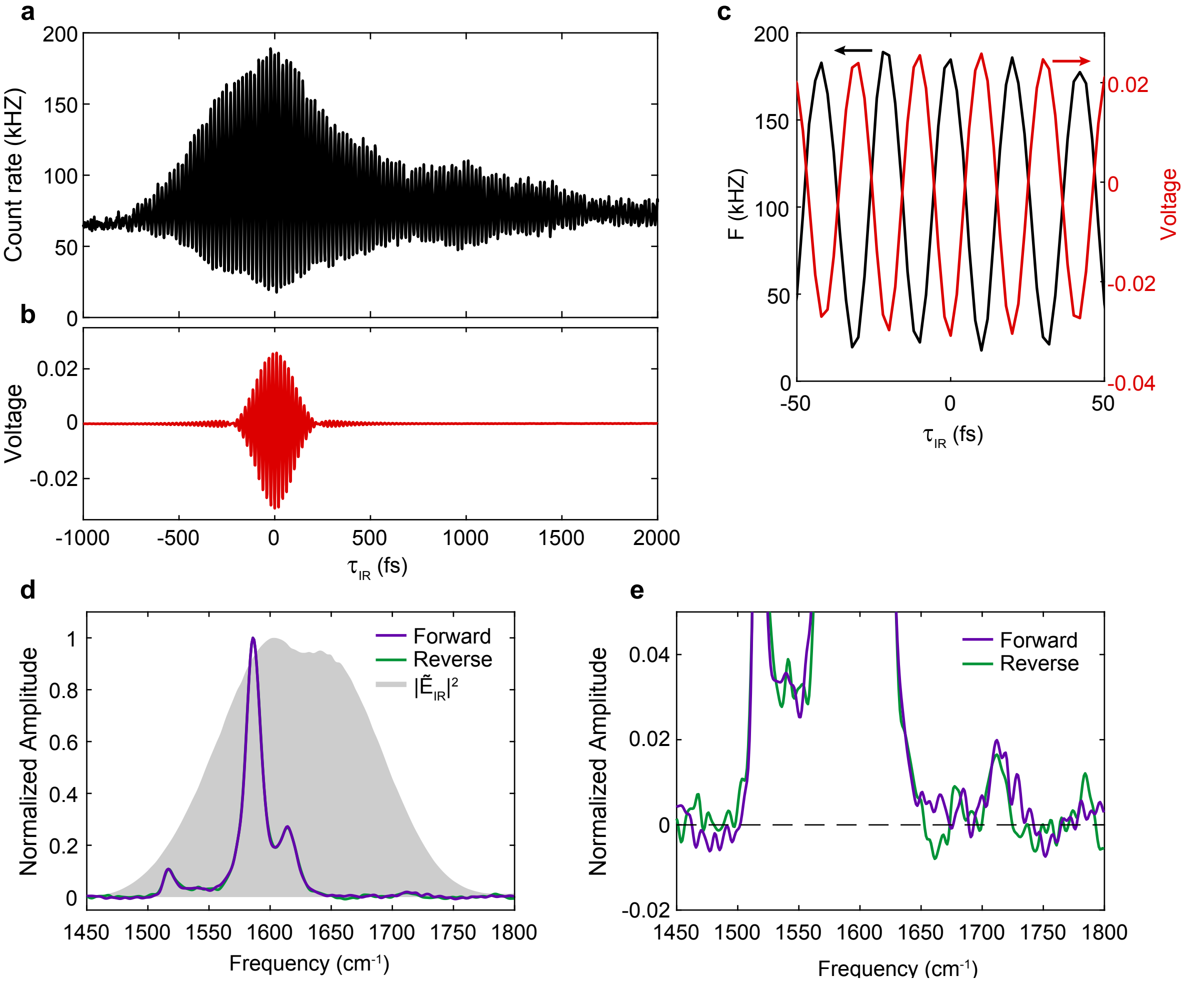

Figure S7: Acquisition and processing of the three-pulse signal to a spectrum. (a) Total count rate F_{tot} in a three-pulse FEIR experiment on C6 at $\tau_{\text{enc}} = 600$ fs and (b) IR reference data from the forward scan direction. A constant offset voltage in (b) has been removed, and the slight asymmetry between the amplitude of fringes above and below the zero level are caused by the onset of mild detector saturation. (c) Detail of the two signals in (a) and (b), showing the π phase-shift from the dark arm of the MZI. (d) Processed FEIR spectra from the forward scan direction (purple), reverse direction (green), and the IR pulse spectrum (gray) processed from the IR reference. (e) Detail of the baseline from the spectra in (d). The black dashed line along the baseline has been added to guide the eye, and the peak at 1712 cm^{-1} with 2% relative amplitude is the weakly FEIR active carbonyl mode.

the same IR reference.

Due to the direction-dependence of continuously-scanned τ_{IR} axes,[10] this FT procedure is performed separately for the forward and reverse directions of stage travel. As shown in Figure S7(e), there may be small residual phase errors in the FEIR spectrum that vary between the two scan directions. In this particular measurement these errors are small enough to be inconsequential (much less than 1% of the total amplitude), however errors at the 1-3% level are also common, and are not always oppositely signed between directions. We suspect this artifact may originate from or at least be exacerbated by the fact that the IR reference is not collected simultaneously with the FEIR data, allowing for instrumental drift (e.g. in the MZI pathlength difference) between acquisitions. The character of this phase error is, however, also consistent with a minor thermal effect.[10] In practice, the forward and reverse spectra are averaged together, which often roughly cancels this effect.

S4 Vibrationally-nonresonant IR + visible two-photon absorption (TPA)

S4.1 Modelling TPA fluorescence in FEIR experiments

Vibrationally-nonresonant TPA is a possible excitation route for generating target population, and therefore represents a potential artifactual contribution to the fluorescence signal in an FEIR experiment. Understanding how this signal artifact appears in the data is correspondingly important for interpreting early-time signals. On the other hand, the nonresonant nature of the TPA response (with respect to the IR or visible pulses individually) means that it reports in a direct way on the temporal pulse characteristics, and therefore has utility as a pulse diagnostic tool for the FEIR spectrometer. Specifically, the TPA response directly reports on the IR/Vis intensity cross-correlation and can therefore be used to map out the experiment's IRF.

From the perspective of the molecular system, this non-degenerate two-photon process involving one IR and one visible photon is essentially instantaneous, occurring within the electronic dephasing time of some 10's of fs. In practice, TPA therefore only occurs during the temporal overlap of the IR and visible pulse electric fields. The language conventionally used is of sequential excitation mediated by a "virtual" state. Formally, this is short-hand for describing the overall transition amplitude as a sum over two-step pathways involving all possible system states as intermediates, which is related to the system's polarizability by a Kramers-Heisenberg formula.[14–17] In density-matrix language, the overall two-photon excitation probability (i.e. the square modulus of the overall transition amplitude) is given by the final target population, and is described to fourth-order in the incident field.[18] As a result, the formal structure for calculating TPA is closely related to our fourth-order response function description of FEIR excitation. In principle, it would be possible to model the TPA contribution along the same lines as the finite-pulse response calculations for the FEIR signal, with the response function suitably replaced by sets of delta functions to reflect the essentially impulsive molecular polarizability response.

However, a simpler approach is to assume that the instantaneous excitation rate is directly proportional to the product of the IR and visible field intensities. This approach is typically adopted to describe the practical phenomenology of how multi-photon or other nonlinear parametric signals depend on the driving fields.[5,19] The final accumulation of target population after the pulse sequence has finished interacting with the sample is then proportional to the time integral

$$\bar{N}^{\mathrm{TPA}} \propto \int_{-\infty}^{\infty} (E_{\mathrm{IR}}(t))^2 (E_{\mathrm{vis}}(t))^2 dt. \tag{S29}$$

With our FEIR pulse sequence the TPA fluorescence signal $S \propto \bar{N}^{\mathrm{TPA}}$ is therefore

$$S(\tau_{\mathrm{IR}}, \tau_{\mathrm{enc}}) = \int_{-\infty}^{\infty} (E_1(t + \tau_{\mathrm{IR}} + \tau_{\mathrm{enc}}) + E_2(t + \tau_{\mathrm{enc}}))^2 (E_3(t))^2 dt. \tag{S30}$$

To evaluate this expression we break the real-valued fields into their positive and negative frequency components as before in Section S1.1. Invoking the RWA, we only keep the terms where the carrier phase oscillations between the four fields cancel,

$$\begin{aligned} S(\tau_{\text{IR}},\tau_{\text{enc}}) &= \int_{-\infty}^{\infty}(E_1^+E_1^- + E_2^+E_2^- + E_1^+E_2^- + E_1^-E_2^+)(E_3^+E_3^-)dt \\ &= S_1(\tau_{\text{IR}}+\tau_{\text{enc}}) + S_2(\tau_{\text{enc}}) + S_{12}(\tau_{\text{IR}},\tau_{\text{enc}}), \end{aligned} \tag{S31a}$$

where

$$S_1(\tau_{\text{IR}}+\tau_{\text{enc}}) = \frac{1}{4}\int_{-\infty}^{\infty}\mathcal{E}_1^2(t+\tau_{\text{IR}}+\tau_{\text{enc}})\mathcal{E}_3^2(t)dt, \tag{S31b}$$

$$S_2(\tau_{\text{enc}}) = \frac{1}{4}\int_{-\infty}^{\infty}\mathcal{E}_2^2(t+\tau_{\text{enc}})\mathcal{E}_3^2(t)dt, \tag{S31c}$$

$$S_{12}(\tau_{\text{IR}},\tau_{\text{enc}}) = \frac{1}{2}\text{Re}\Big\{e^{-i\omega_{\text{IR}}\tau_{\text{IR}}}\int_{-\infty}^{\infty}\mathcal{E}_1(t+\tau_{\text{IR}}+\tau_{\text{enc}})\mathcal{E}_2(t+\tau_{\text{enc}})\mathcal{E}_3^2(t)e^{i[\phi_{\text{IR}}(t+\tau_{\text{IR}})-\phi_{\text{IR}}(t)]}dt\Big\}. \tag{S31d}$$

Here we have used the notation for temporal pulse amplitude and phase introduced in Section S1.2. Specifically, $\phi_{\text{IR}}(t)$ is the temporal phase of the IR pulse, which is assumed to be the same for both copies E_1 and E_2. Importantly, the TPA signal is not sensitive to the phase of the visible pulse E_3, which can be interpreted as a consequence of the bra- and ket-side pair of light-matter interactions occurring within its envelope. The subscripts labelling the different contributions in Eq. S31 indicate their dependence on the IR pulses in an analogous way to our notation for the different FEIR signal contributions in Eq. S28 and Sec. IIIA of Paper I, i.e. S_1 depends on E_1 but not E_2, while S_{12} depends on both. We note the clear similarity between these contributions to the TPA signal versus those for FEIR. Specifically, the two-pulse and three-pulse contributions are related among themselves by

$$S_{12}(\tau_{\text{IR}}=0,\tau_{\text{enc}}) = 2S_2(\tau_{\text{enc}}) = 2S_1(\tau_{\text{enc}}), \tag{S32}$$

as can be verified directly from the expressions in Eq. S31.

Figure S8 shows a numerical calculation of the full three-pulse-resolved TPA signal $S(\tau_{\text{IR}},\tau_{\text{enc}})$ as well as slices along τ_{enc} and τ_{IR}, for the transform-limited Gaussian IR and visible pulses similar to those used in the response function calculations (see figure caption). The three-pulse contribution S_{12} is responsible for the interferometric oscillation along τ_{IR}, while the two-pulse contributions S_1 and S_2 form the cross-shaped pattern intersecting at the origin.

It is worth considering the similarities and differences between this three-pulse-resolved TPA signal and various types of pulse characterization techniques using parametric nonlinear sample response, e.g. interferometric autocorrelation, or the various flavors of frequency-resolved optical gating.[5,19] The trace $S(\tau_{\text{IR}},\tau_{\text{enc}}=0)$ (Figure S8(b)) qualitatively resembles an interferometric autocorrelation, with the important differences that the intensity ratio of peak to baseline is 4:1, rather than 8:1, and the oscillating component only has frequency content around ω_{IR}, and not also at $2\omega_{\text{IR}}$. These differences arise because the TPA signal is only quadratic in E_{IR}, rather than quartic in the case of the interferometric autocorrelation. The trace $S(\tau_{\text{IR}}=0,\tau_{\text{enc}})$ (Figure S8(c)) is formally the IR/Vis intensity cross-correlation, which can also be seen explicitly in the expression Eq. S31(c) in conjunction with Eq. S32. This cross-correlation represents the IRF of an FEIR experiments, and its width is therefore a practical measure of the time-resolution. In a two-pulse FEIR measurement, the TPA signal (if present) therefore appears as a spike riding on top of the FEIR signal at $\tau_{\text{enc}} =$

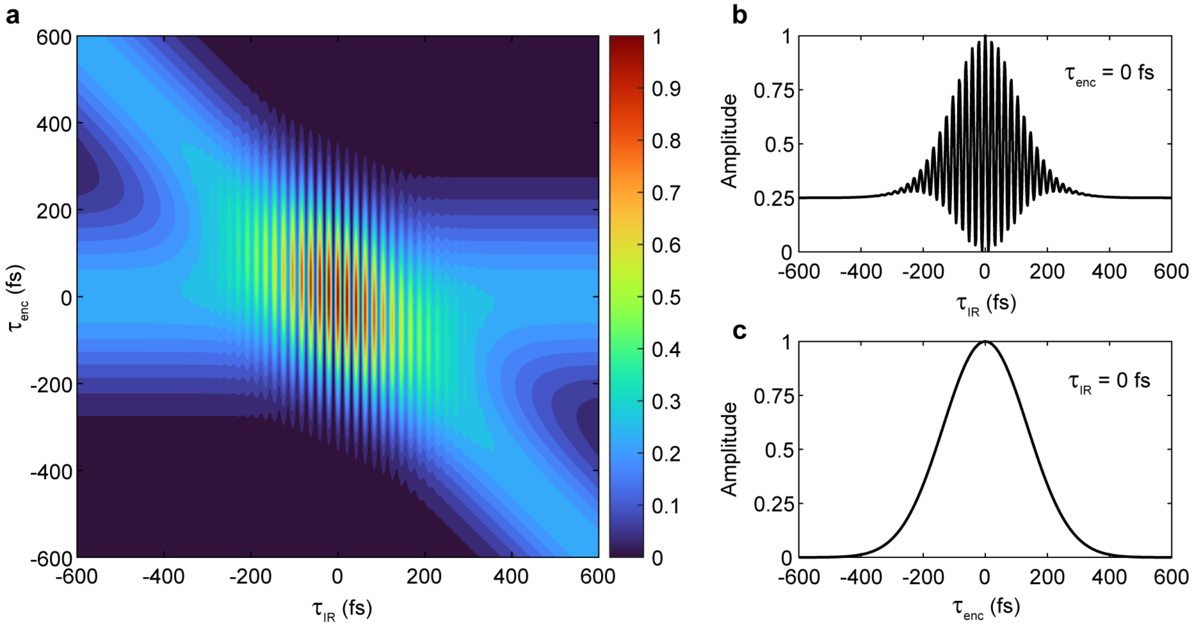

Figure S8: Appearance of the three-pulse-resolved TPA signal in the time-domain. The IR and visible pulses are transform-limited and Gaussian with $\Delta\omega_{\mathrm{IR}} = 120$ cm^{-1} ($\tau_{p,\mathrm{IR}} = 123$ fs), and $\Delta\omega_{\mathrm{vis}} = 50$ cm^{-1} ($\tau_{p,\mathrm{vis}} = 297$ fs). (a) Fully-resolved signal $S(\tau_{\mathrm{IR}}, \tau_{\mathrm{enc}})$, (b) the slice $S(\tau_{\mathrm{IR}}, \tau_{\mathrm{enc}} = 0)$, and (c) the slice $S(\tau_{\mathrm{IR}} = 0, \tau_{\mathrm{enc}})$.

0, and indicates the pulse-overlap region.

S4.2 Frequency-resolved TPA signal and dependence on pulse durations and IR spectral phase

Next, we examine the behavior of the TPA signal in the frequency-domain, i.e. as it would appear when measuring FEIR spectra with the three-pulse experiment. From a pulse diagnostic standpoint, more information about the IR spectral phase can be gleaned from this frequency-domain representation of the TPA signal. The three-pulse-resolved TPA signal is processed in the same way as three-pulse FEIR data, i.e. the spectrum is the real part of the one-sided Fourier transform of $\tau_{\mathrm{IR}} > 0$ data

$$S^{\mathrm{TPA}}(\omega, \tau_{\mathrm{enc}}) = \mathrm{Re}\int_0^\infty S_{12}(\tau_{\mathrm{IR}}, \tau_{\mathrm{enc}}) e^{i\omega\tau_{\mathrm{IR}}} d\tau_{\mathrm{IR}}. \tag{S33}$$

Just like the case for FEIR signals, a projection-slice relation connects the projection of the frequency-resolved TPA signal onto the encoding delay to the IR/Vis intensity cross-correlation

$$\begin{aligned}\int_{-\infty}^{\infty} S^{\mathrm{TPA}}(\omega, \tau_{\mathrm{enc}}) d\omega &= S_{12}(\tau_{\mathrm{IR}} = 0, \tau_{\mathrm{enc}}) \\ &= 2S_1(\tau_{\mathrm{enc}}) = 2S_2(\tau_{\mathrm{enc}}) = \frac{1}{2} S(\tau_{\mathrm{IR}} = 0, \tau_{\mathrm{enc}}).\end{aligned} \tag{S34}$$

Figure S9 displays contour surface representations of $S^{\mathrm{TPA}}(\omega, \tau_{\mathrm{enc}})$ for a variety of different IR and visible pulse characteristics. Figure S9(a) shows the case corresponding to the time-domain data

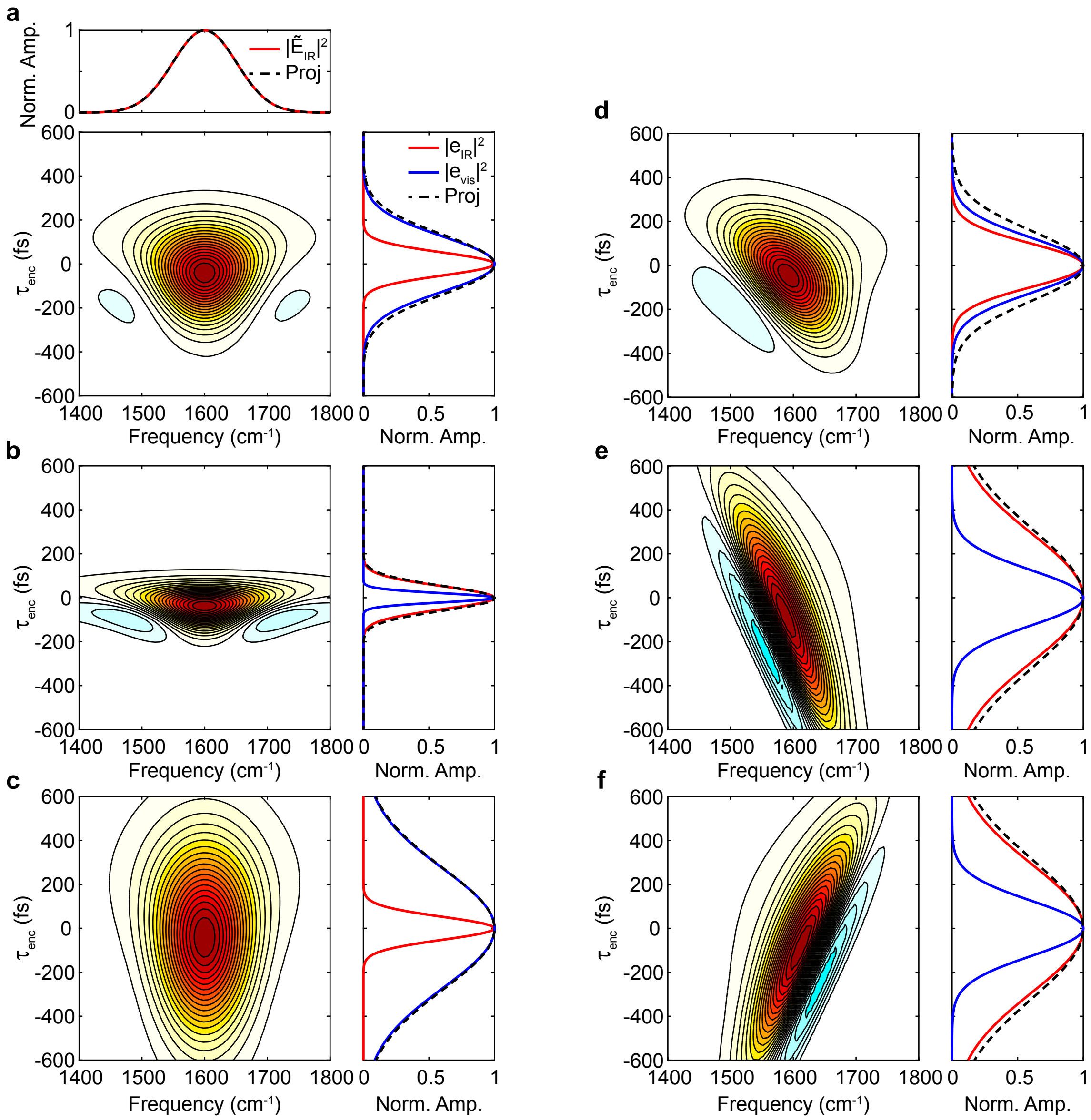

Figure S9: Frequency-resolved TPA signals $S^{\mathrm{TPA}}(\omega, \tau_{\mathrm{enc}})$ with corresponding IR and visible temporal intensity profiles and cross-correlations for a variety of relative pulse durations and values of $\gamma_{\mathrm{IR},2}$. In all cases the IR spectrum is Gaussian with $\omega_{\mathrm{IR}} = 1600$ cm^{-1} and $\Delta\omega_{\mathrm{IR}} = 120$ cm^{-1}. In (a)-(c) both pulses are transform-limited with $\tau_{p,\mathrm{IR}} = 123$ fs and (a) $\Delta\omega_{\mathrm{vis}} = 50$ cm^{-1} ($\tau_{p,\mathrm{vis}} = 297$ fs), (b) $\Delta\omega_{\mathrm{vis}} = 300$ cm^{-1} ($\tau_{p,\mathrm{vis}} = 49$ fs), and (c) $\Delta\omega_{\mathrm{vis}} = 23$ cm^{-1} ($\tau_{p,\mathrm{vis}} = 640$ fs). The top panel of (a) shows the projection of the TPA signal onto the ω-axis overlayed on the IR spectrum. (d)-(f) use the same spectra as (a), with a transform-limited visible pulse but chirped IR of (d) $\gamma_{\mathrm{IR},2} =$ -8700 fs^2 ($\tau_{p,\mathrm{IR}} = 232$ fs), (e) $\gamma_{\mathrm{IR},2} =$ -30,000 fs^2 ($\tau_{p,\mathrm{IR}} = 689$ fs), and (f) $\gamma_{\mathrm{IR},2} =$ 30,000 fs^2 ($\tau_{p,\mathrm{IR}} = 689$ fs).

in Figure S8, i.e. transform-limited pulses with spectral bandwidth representative of our current experiments. The overall frequency extent of the signal follows the IR pulse spectrum, and as shown in the upper panel, the projection of $S^{\mathrm{TPA}}(\omega, \tau_{\mathrm{enc}})$ onto the ω-axis in fact exactly reproduces the IR pulse spectrum. This equality between the ω-projection and IR spectrum holds for all the cases shown in Figure S9, and is therefore not shown for the other cases.

The projection onto the τ_{enc}-axis, i.e. the IR/Vis cross-correlation, is shown on the right panel superimposed on the IR and visible temporal intensity profiles. While the IR/Vis cross-correlation is symmetric in τ_{enc}, the shape of the TPA spectrum varies asymmetrically in τ_{enc}, with small negative side lobes for $\tau_{\mathrm{enc}} < 0$, switching to exaggerated positive wings for $\tau_{\mathrm{enc}} > 0$. Figures S9(b) and (c) show cases where the IR pulse is the same as in (a), but with a transform-limited visble pulse that is alternately much shorter ($\Delta\omega_{\mathrm{vis}}$ = 300 cm^{-1}, $\tau_{p,\mathrm{vis}}$ = 49 fs), or much longer ($\Delta\omega_{\mathrm{vis}}$ = 23 cm^{-1}, $\tau_{p,\mathrm{vis}}$ = 640 fs), respectively. When the visible pulse is significantly shorter than the IR (Figure S9(b)), the magnitude of this asymmetry is more significant (e.g. evident from the deeper negative lobes), while in the opposite scenario (Figure S9(c)) the asymmetry is less pronounced. This asymmetric τ_{enc}-evolution may have a physcial interpretation along similar lines to that of the pulse-overlap lineshape distortion to FEIR spectra discussed previously in Section S2.

The effect of second-order dispersion ($\gamma_{\mathrm{IR},2}$, Eq. S18), or chirp, on the IR pulse is demonstrated in Figures S9(d)-(f). These three cases use the same IR and visible pulse spectra as in (a), and the visible remains transform-limited. Figure S9(d) shows the case of $\gamma_{\mathrm{IR},2}$ = -8700 fs^2, which produces a duration of 232 fs duration, which is similar to the IR pulse used in experiment (with slightly less bandwidth). The effect of this dispersion is to tilt the spectral feature in the ω-τ_{enc} plane, and roll its phase asymmetrically to one side of ω_{IR}. The direction of this tilt and asymmetry is consistent with the sign of the $\gamma_{\mathrm{IR},2}$, in this case a negative sign corresponding to a "down-chirp" where the high frequencies precede the low frequencies within the envelope. This sensitivity to the sign of $\gamma_{\mathrm{IR},2}$ is demonstrated in more extreme circumstances in Figures S9(e) and (f), where the tilt and asymmetry are flipped when switching between $\gamma_{\mathrm{IR},2}$ = -30,000 fs^2 and 30,000 fs^2, respectively. In principle, evidence of higher-order IR spectral dispersion could be inferred from the frequency-resolved TPA signal, although their characteristic signatures are more complicated. For example, third-order dispersion contributes a triangular horn-shaped pattern (not shown).

Overall, we have seen how vibrationally-nonresonant TPA can manifest in FEIR measurements. Specifically, the TPA response exists within the IR/Vis pulse-overlap region, and can therefore potentially obscure the interpretation of the FEIR data at the earliest encoding delays. In two-pulse experiments, the TPA response is exactly the IR/Vis intensity cross-correlation, and appears as a spike at $\tau_{\mathrm{enc}} = 0$. In FEIR spectra derived from three-pulse measurements, the TPA response spans the IR pulse spectrum as would be expected for a nonresonant process, although the τ_{enc}-dependence is sensitive the pulses' relative duration and the IR spectral phase. Because the TPA response effectively maps out the pulse-overlap region, it can be used to characterize the temporal pulse characteristics and provides a direct measure of the FEIR spectrometer's instrument response function as demonstrated next in Sec. S5.2.

S4.3 Presence of TPA artifacts in coumarin experiments

Because the resonance conditions for FEIR excitation are automatically the same as that for IR + visible TPA, a natural question of great practical importance is under what conditions will the TPA response be present, and how large will it be relative to the proper FEIR signal? The strength of the TPA response is presumably connected to the molecular polarizability, and might correlate with the degenerate two-photon cross-section of the molecule's electronic transition, which have often been characterized for popular fluorophores. In cases where the FEIR activity of vibrations under investigation are small, it might be expected that the relative size of the TPA response could be significant.

A clear example of a strong TPA artifact is in the FEIR measurements on the C337 nitrile discussed in main text Sec. VA. In this case, the TPA signal is likely prominent because the nitrile FEIR activity is small, although the strength of the non-degenerate two-photon cross-section with these resonance conditions could also be particularly large. We note that the additional Fano-like phase distortion to the vibrational resonance within the TPA signal is not explained by the theory presented here and requires further investigation.

In our experiments on the high frequency coumarin ring and carbonyl vibrations the true FEIR response is dominant and it is not clear how much TPA signal is present in all cases. The two-pulse signals from the full set of these experiments are shown in main text Fig. 1, and the τ_{enc}-dependent spectra are shown in Sec. S6. The cases in which the two-pulse signal peaks at $\tau_{\text{enc}} = 0$ ps (C314, C337, C153, C343, C334) also show to varying degree a broad spectral feature roughly spanning the pump spectrum during pulse overlap, both of which are consistent with a TPA signal of sufficient strength to be competitive with the FEIR response. The presence of this potential TPA contribution in the C343 measurement was mentioned in main text Sec. VB. The signal brightness analysis conducted previously in Ref. [20] used the two-pulse signal amplitude averaged between $\tau_{\text{enc}} = 0.4$ and 0.8 ps to avoid any contributions from TPA.

On the other hand, the remaining coumarins investigated (C30, C6, C7, C525, C545) do not show any significant evidence of TPA contributions, indicting that the FEIR response is comparatively much stronger, and the τ_{enc}-dependent shape of their signals are well described by response function simulations within the pulse-overlap region.

S5 Temporal pulse characterization and instrument response

S5.1 IR pulse characterization by interferometric autocorrelation

The IR pulse duration was characterized by interferometric autocorrelation (IAC) in a 0.5 mm $AgGaS_2$ (AGS) crystal at the sample position. The resulting SHG signal is collected through the microscope with a reflective Schwartzchild replacing the refractive objective used for FEIR measurements and a pair of removable mirrors directing the transmitted IR beam to an photovoltaic MCT detector. Depending on the IR center frequency ω_{IR}, different materials are placed in front of the detector as transmission filters to block the fundamental while passing the SHG. For $\omega_{\text{IR}} \sim 3$ μm clear acrylic is used, for ω_{IR} between 4 and 5 μm 10 mm of N-BK7, and for $\omega_{\text{IR}} > 5.5\mu$m two $\sim$1 mm glass microscope slides. 1 mm of CaF_2 is included in the optical path before the AGS crystal to account for transmission into the sample cell.

Figure S10 shows the spectra and IACs for IR pulses used for the C6 and C343 experiments at $\omega_{\text{IR}} = 1620$ cm^{-1} and the C337 nitrile experiments at $\omega_{\text{IR}} = 2235$ cm^{-1}. The IAC data is shifted and scaled so that the lowest fringe falls to zero and the long-time baseline is unity. The zero frequency band of the data is the intensity autocorrelation (IA),[5] which is extracted by a Fourier filter. We use the FWHM of the temporal pulse intensity profile as a definition of pulse duration $\tau_{\text{p, IR}}$. Assuming a Gaussian profile, the pulse duration, taken as FWHM temporal intensity envelope, is related to

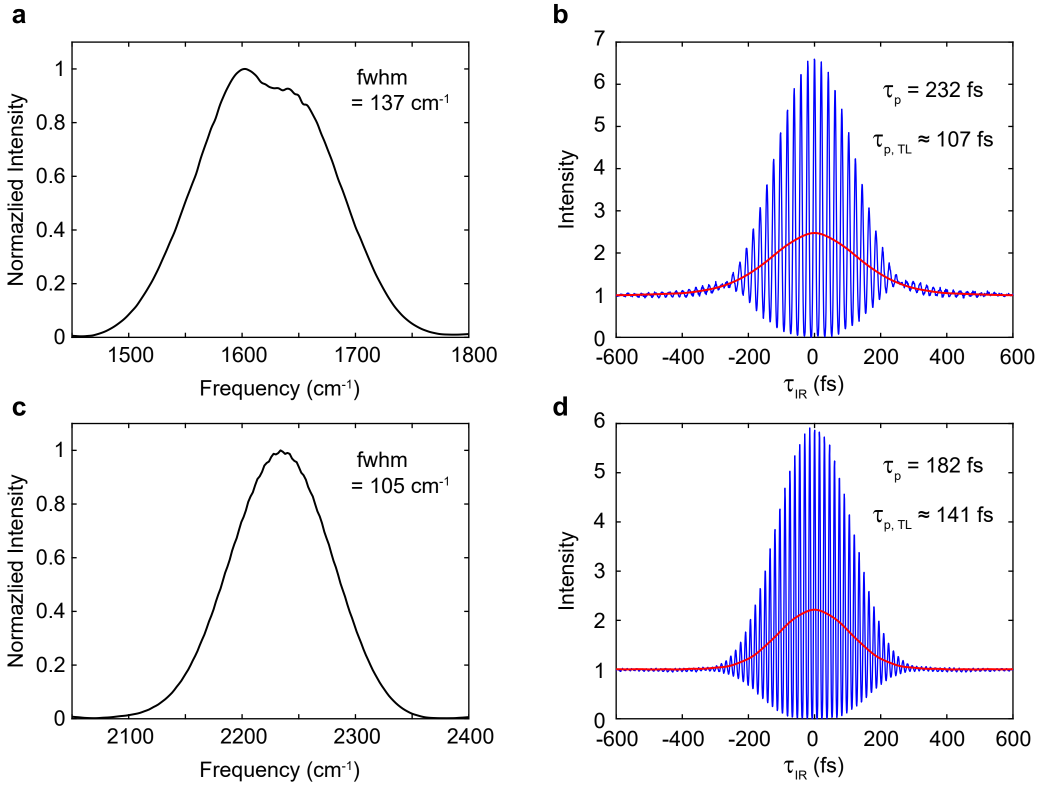

Figure S10: IR pulse spectrum and interferometric autocorrelation (IAC) at (a)-(b) $\omega_{\text{IR}} = 1620$ cm-1 (6.17 μm) and (c)-(d) $\omega_{\text{IR}} = 2235$ cm-1 (4.47 μm). In (b) and (d) the extracted IA (red) is shown over the IAC (blue).

the FWHM of the IA by $\tau_{\text{p}} = \tau_{\text{IA}}/\sqrt{2}$. We use this relation to report the pulse duration from a Gaussian fit of the recovered IA.

For the 6 μm pulse, the resulting 232 fs IR pulse duration (transform limit of 107 fs) is consistent with the dispersion that results from the summed GVD of materials in the optical path. This includes the 4 mm thick LGS OPA crystal, BaF_2 collimating lens, and two 1 mm thick Germanium windows in the mid-IR OPA, the ZnSe beamsplitters in the interferometer, the ZnSe asphere in the FEIR microscope, and 1 mm CaF_2 bottom sample window. The 4.5 μm pulse is closer to transform-limited, with a 182 fs duration (transform limit of 141 fs), due to the lower combined dispersion from these materials at this shorter wavelength and smaller bandwidth over which dispersion can play a role.

S5.2 IR/Vis temporal pulse overlap characterized by TPA

We characterize the effective temporal instrument response function (IRF) of the FEIR experiment with fluorescence excited by TPA as introduced in Sec. S4. With independent knowledge of the IR pulse characteristics, e.g. by IAC, the visible pulse duration can therefore be backed out. At minimum, a fluorophore that can be used for this purpose must exhibit IR + Vis two-photon electronic resonance, which operationally is automatically satisfied for the electronic pre-resonance condition used for FEIR. However, it must also not contain any FEIR active vibrations (or better yet, no vibrations at all) in resonance with the IR spectrum. Additionally, the molecule must have a non-vanishing two-photon cross-section. In practice, this second criterion is difficult to achieve in the 6 μm region, where most electronically-conjugated molecules have C=C ring stretching vibrations. Using TPA to characterize the IRF for 6 μm experiments therefore remains a currently unsolved problem. To characterize the visible pulse duration, we therefore employ the 4.5 μm IR pulse used for the nitrile experiments, which lies in the typical IR clear window of organic molecules (i.e. those lacking nitrile, azide or other specialized "vibrational probe" groups).

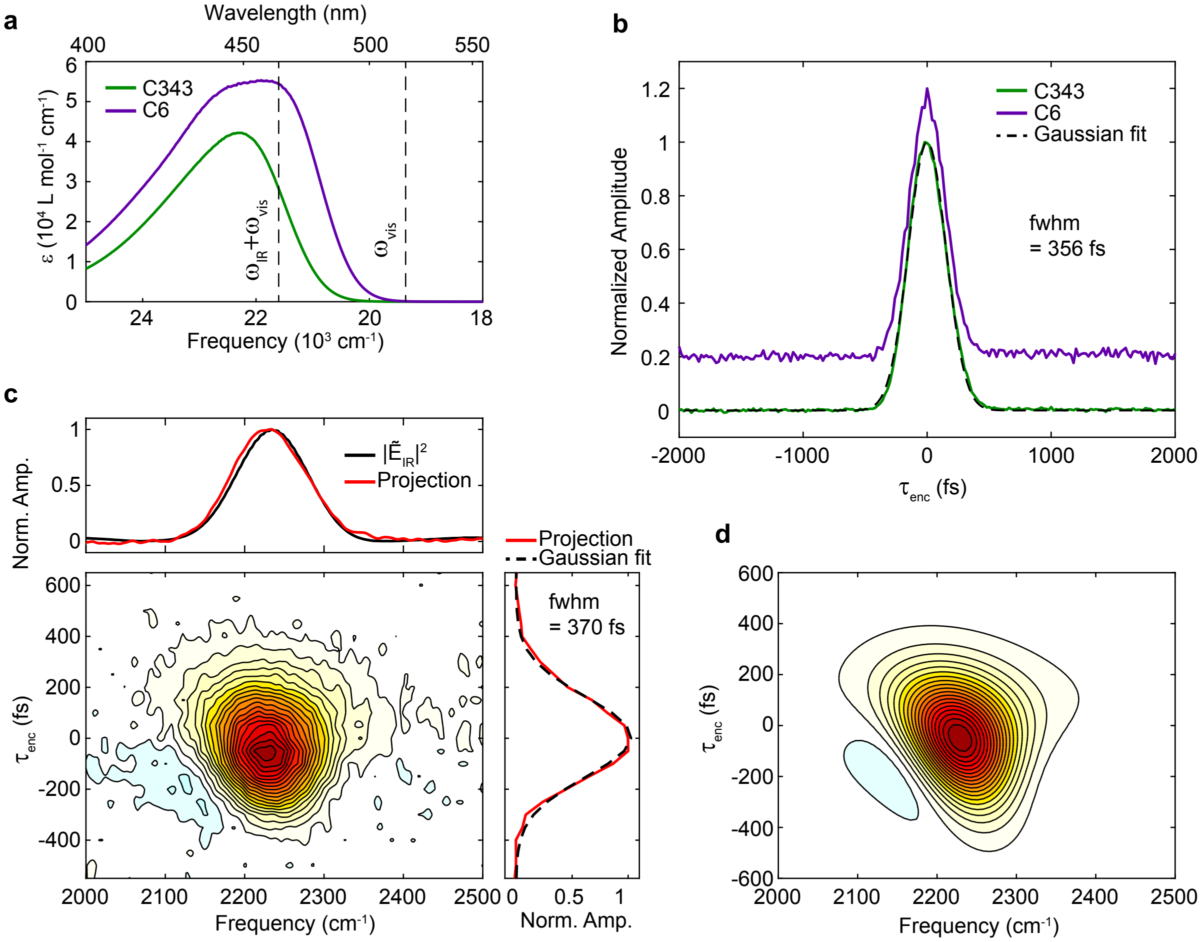

Figure S11: TPA signals from C343 and C6 with vibrationally off-resonant IR pumping. (a) Electronic absorption spectra for C343 and C6 indicating resonance conditions for $\omega_{\mathrm{IR}} = 2235$ cm^{-1} (4.47 μm). (b) Background-subtracted, normalized two-pulse transients for C6 and C343. The two signals have been offset for clarity. A Gaussian fit yielding a FWHM of 356 fs is shown for C343. (c) Frequency-resolved TPA signal from C343. The projection of the surface onto the frequency axis is shown overlayed on the IR pulse spectrum, while the projection onto the τ_{enc} axis is shown with a Gaussian fit yielding a FWHM of 370 fs. (d) Calculation of frequency-resolved TPA signal with using a Gaussian IR pulse spectrum with second-order dispersion consistent with the experimental IAC, and a transform-limited 315 fs Gaussian visible pulse.

Figure S11 shows the pure TPA signals from coumarins 6 and 343 (C343) using the 4.5 μm IR pulse. Neither of the coumarins have any vibrations within its bandwidth, while they both exhibit good electronic resonance with the sum frequency $\omega_{\mathrm{IR}} + \omega_{\mathrm{vis}}$ (Figure S11(a)). Background-subtracted two-pulse transients for both molecules are shown in Figure S11(b), which are symmetric in τ_{enc}

and fit well to Gaussians that decays fully to zero, indicative of a nonresonant pulse-overlap signal. The frequency-resolved signal for C343 is shown in Figure S11(c). Its projection onto the frequency axis matches well with the IR pulse spectrum, as predicted for the frequency-resolved TPA signal in Sec. S4. Gaussian fits to the two-pulse signal and the projection of the frequency-resolved signal onto the τ_{enc} axis yield FWHM values of 356 and 370 fs, respectively. Taking these values to represent the FWHM of the IR/Vis intensity cross-correlation, and using the IR pulse duration from the IAC, we back out the visible pulse duration of $\tau_{\text{p,vis}} = \sqrt{356^2 - 182^2} = 306$ fs or 322 fs for the longer or shorter measurements, respectively. We take the average value of 315 fs as our measure of the visible pulse duration. Figure S11(d) shows a calculation of the frequency-resolved TPA signal using a Gaussian IR pulse spectrum with second-order dispersion consistent with the experimental IAC, and a transform-limited 315 fs Gaussian visible pulse, yielding good agreement with features in the TPA spectrum including the shallow negative wing on the red side of the pump indicative of mild IR down-chirp.

S6 Coumarin series τ_{enc}-dependent FEIR data with $\omega_{\text{IR}} = 1620$ cm^{-1}

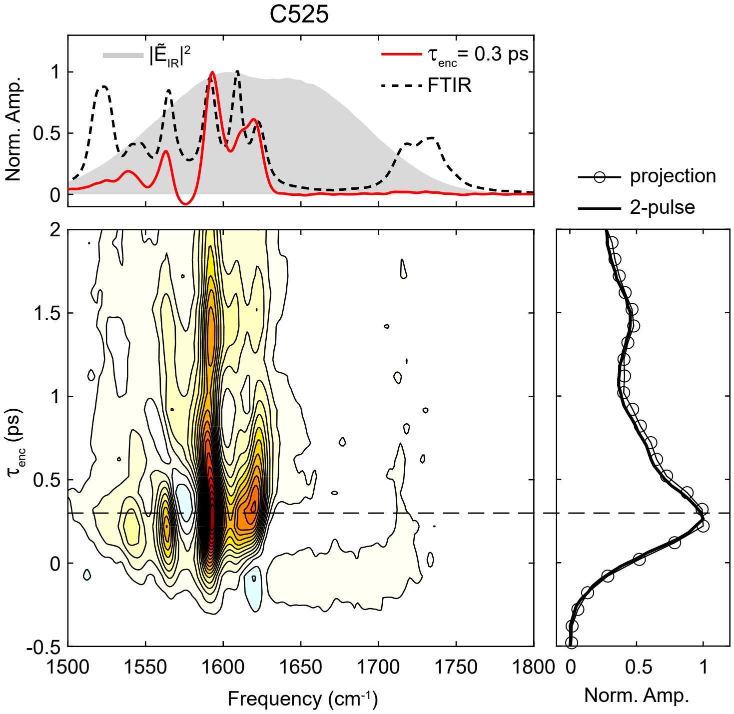

Figure S12: C525 τ_{enc}-dependent FEIR data. Top panel: FTIR spectrum (dashed black), IR pulse spectrum (gray), and FEIR spectrum at the indicated encoding delay. Center panel: τ_{enc}-dependent FEIR spectrum. Contour spacing is set at 5%. Right panel: Experimental two-pulse signal (solid) and τ_{enc}-projection of the spectrum (circles). The encoding delay used for the FEIR spectrum in the top panel is indicated by a dashed line across the central and right panels.

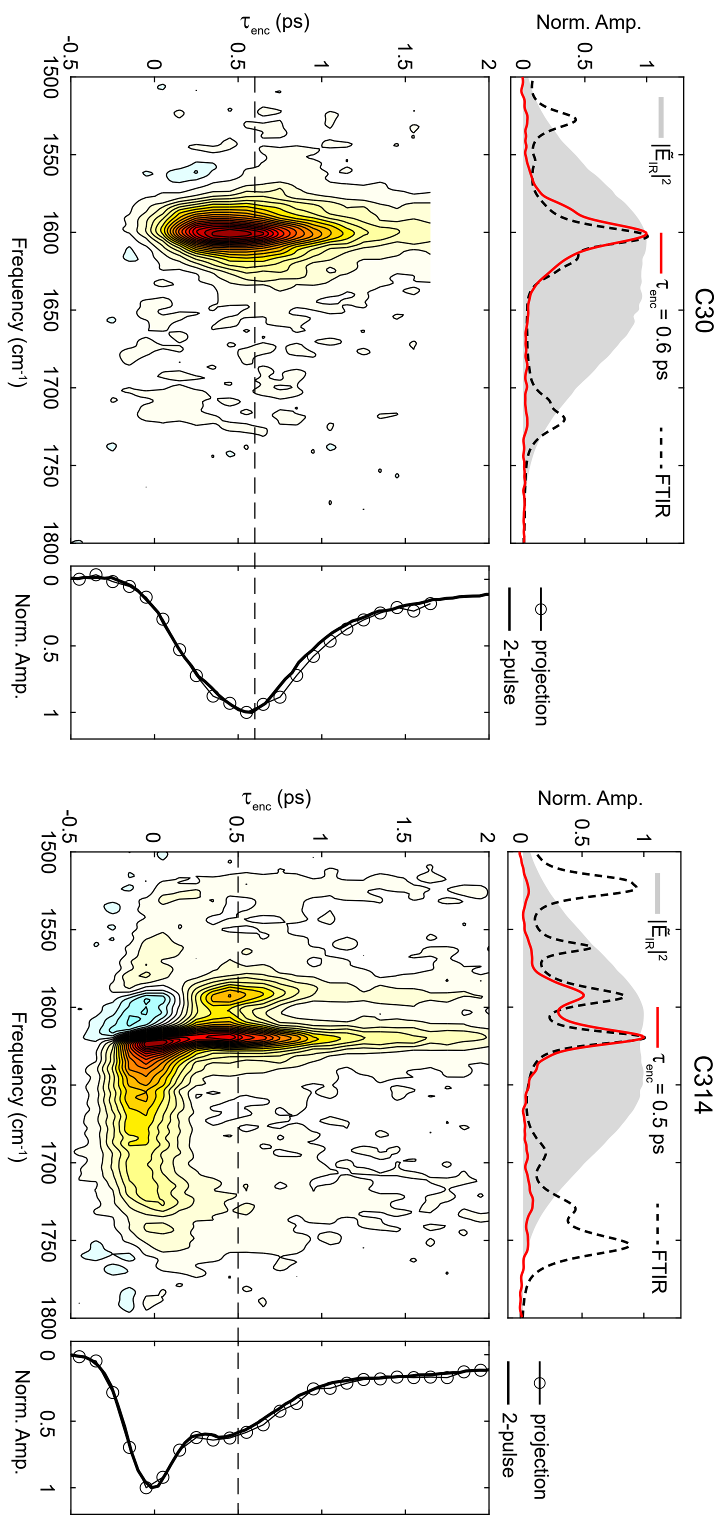

Figure S13: C30 and C314 experimental τ_{enc}-dependent FEIR data. All panels are analogous to Figure S12.

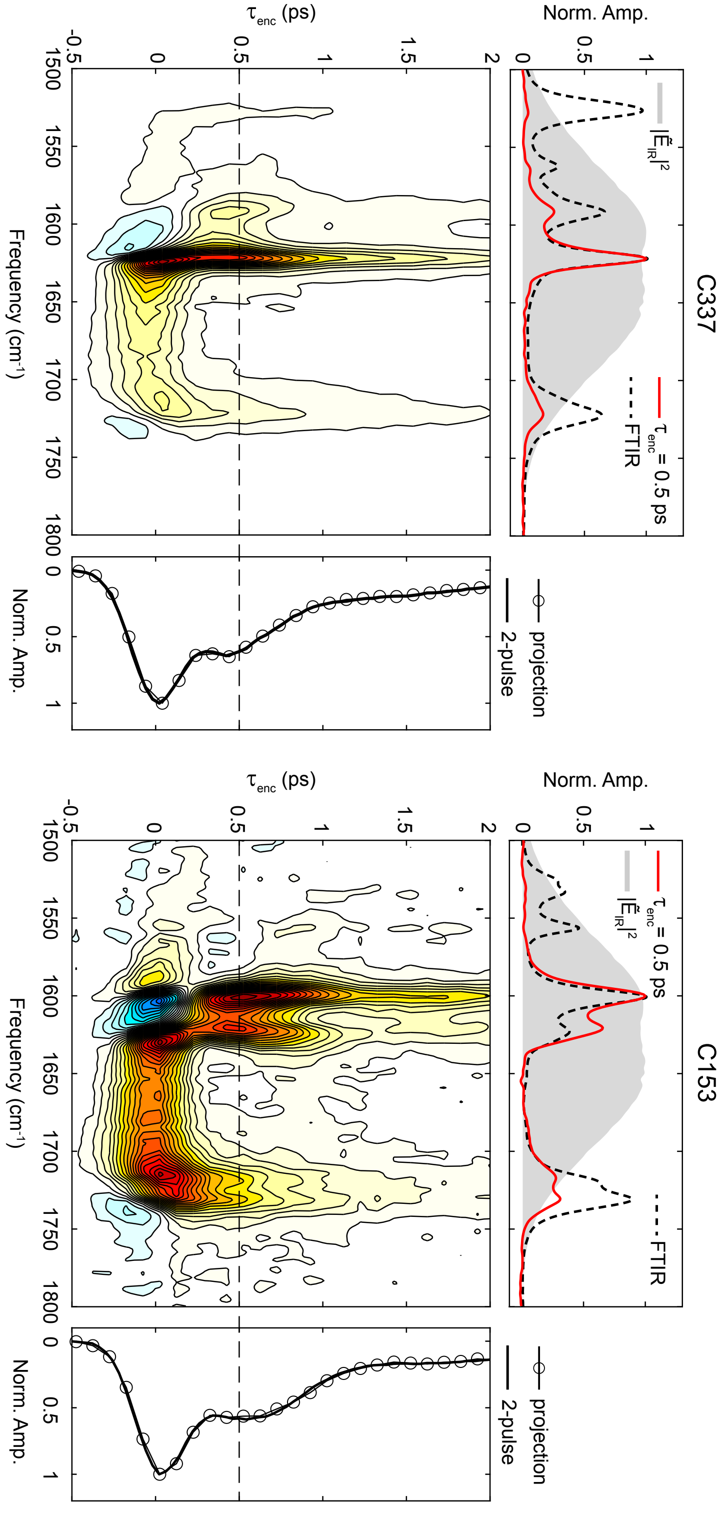

Figure S14: C153 and C337 experimental τ_{enc}-dependent FEIR data. All panels are analogous to Figure S12.

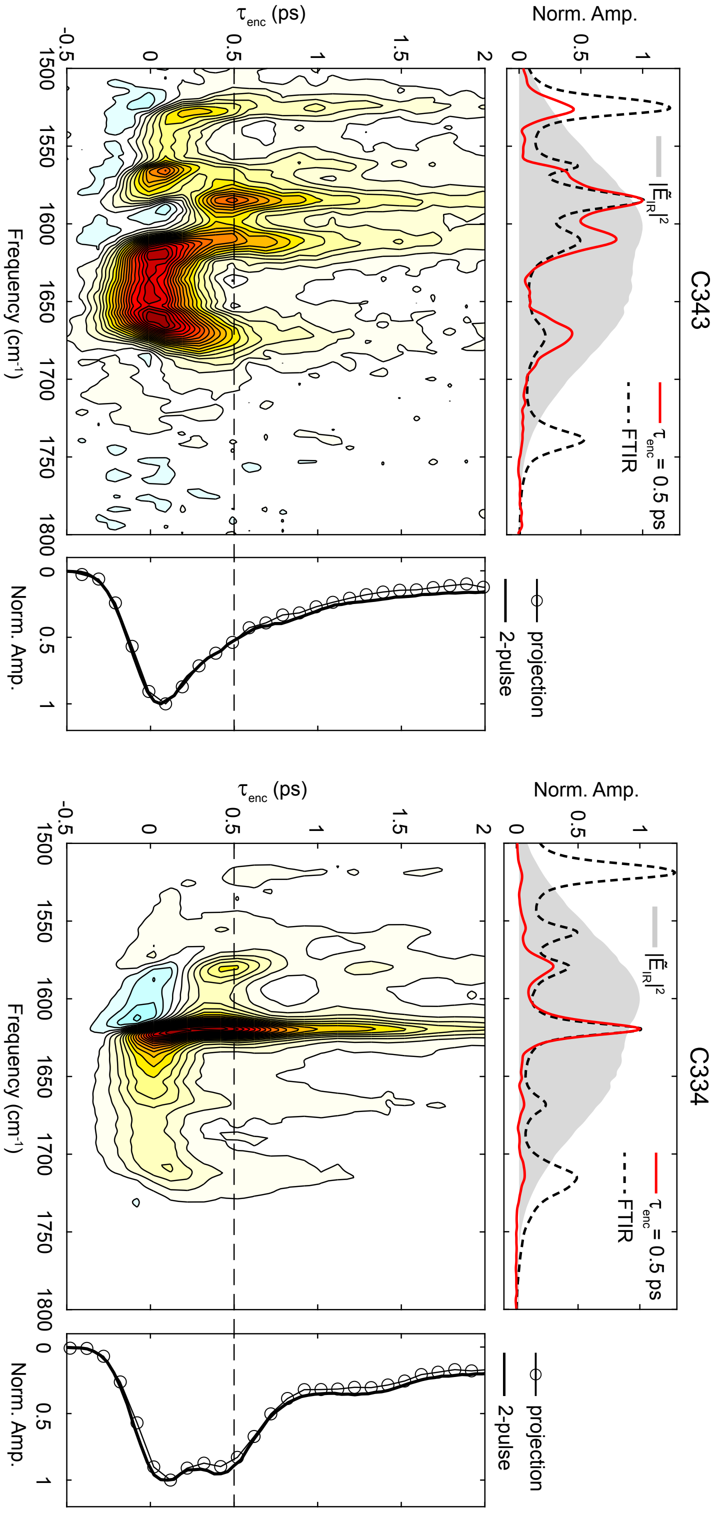

Figure S15: C343 and C334 experimental $\tau_{\rm enc}$-dependent FEIR data. All panels are analogous to Figure S12. The $\tau_{\rm enc}$-dependent FEIR spectrum of C343 in main text Fig 11(c) is from a different measurement using a slightly more red-shifted IR pulse spectrum.

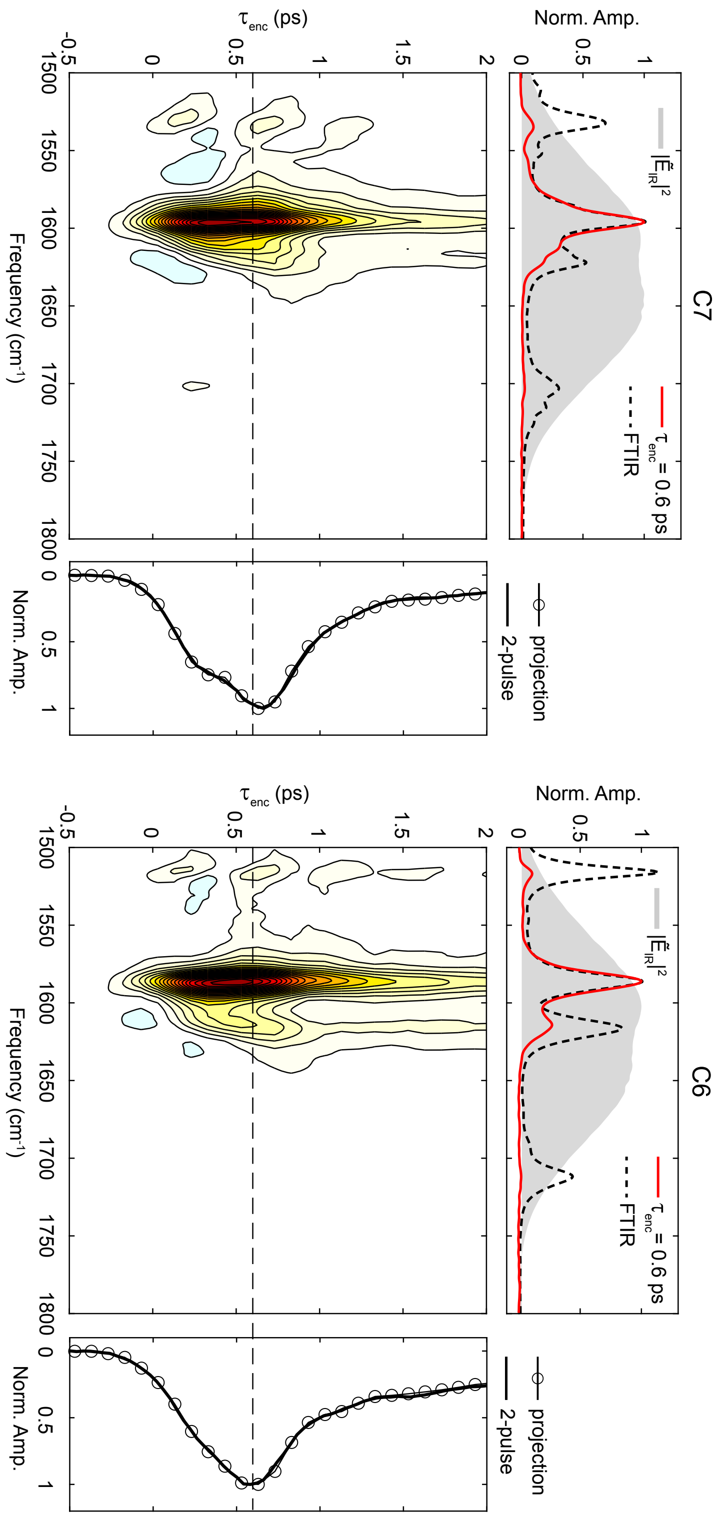

Figure S16: C7 and C6 experimental τ_{enc}-dependent FEIR data. All panels are analogous to Figure S12.

S7 Fitting of C6 and C343 FTIR spectra

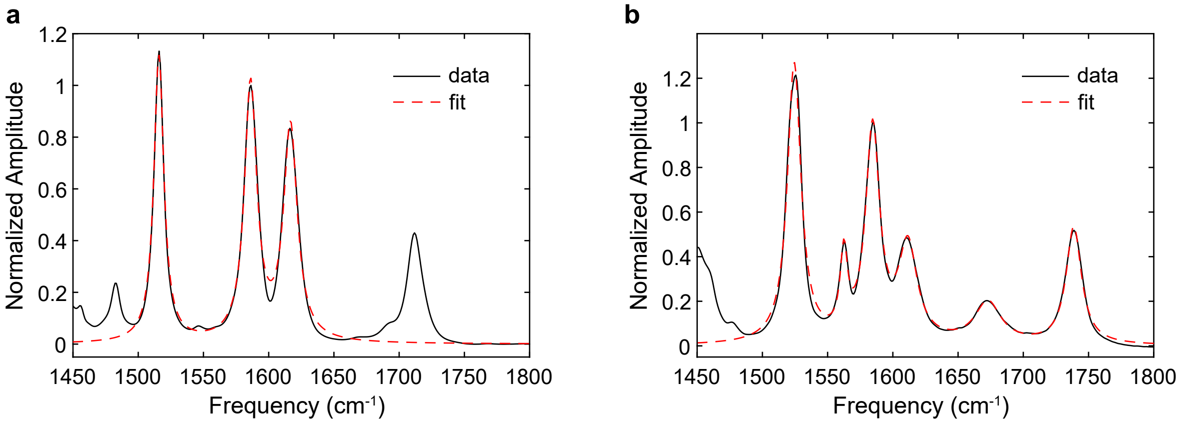

Figure S17: Normalized FTIR absorption spectrum (black) and Lorentzian fit (dashed red) for (a) C6 and (b) C343.

Normalized FTIR spectra are fit to a sum of n Lorentzian functions of the form

$$L_i(\omega) = \frac{a_i b_i}{(\omega - c_i)^2 + b_i^2}, \tag{S35}$$

with $n = 3$ for C6 (Fig. S17(a)) and $n = 6$ for C343 (Fig. S17(b)). For the i^{th} mode the extracted frequency is $\omega_{10} = c_i$, the transition dipole moment is $\mu_{10} = \sqrt{a_i}$, and dephasing rate is $\Gamma_{10} = 2\pi c_0 b_i$ where c_0 is the speed of light (in cm/fs for ω in cm^{-1} and Γ_{10} in fs^{-1}). The set of μ_{10} are then scaled relative to the largest in the set. These extracted parameters are listed in main text Tables II and III for C6 and C343, respectively.

S8 C6 DFT-calculated transition dipole orientations

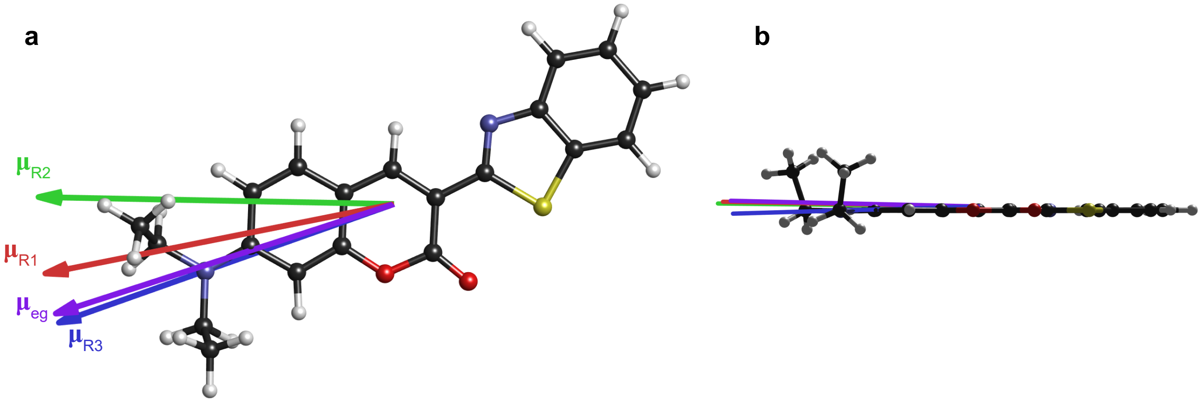

Figure S18: Transition dipole unit vectors for the 3 normal modes and the electronic transition of C6 used in the calculation of main text Section IV, viewed (a) front-on and (b) side-on to the coumarin core.

S9 Calculated C6 FEIR spectra with flipped ν_{R1} FC factor sign

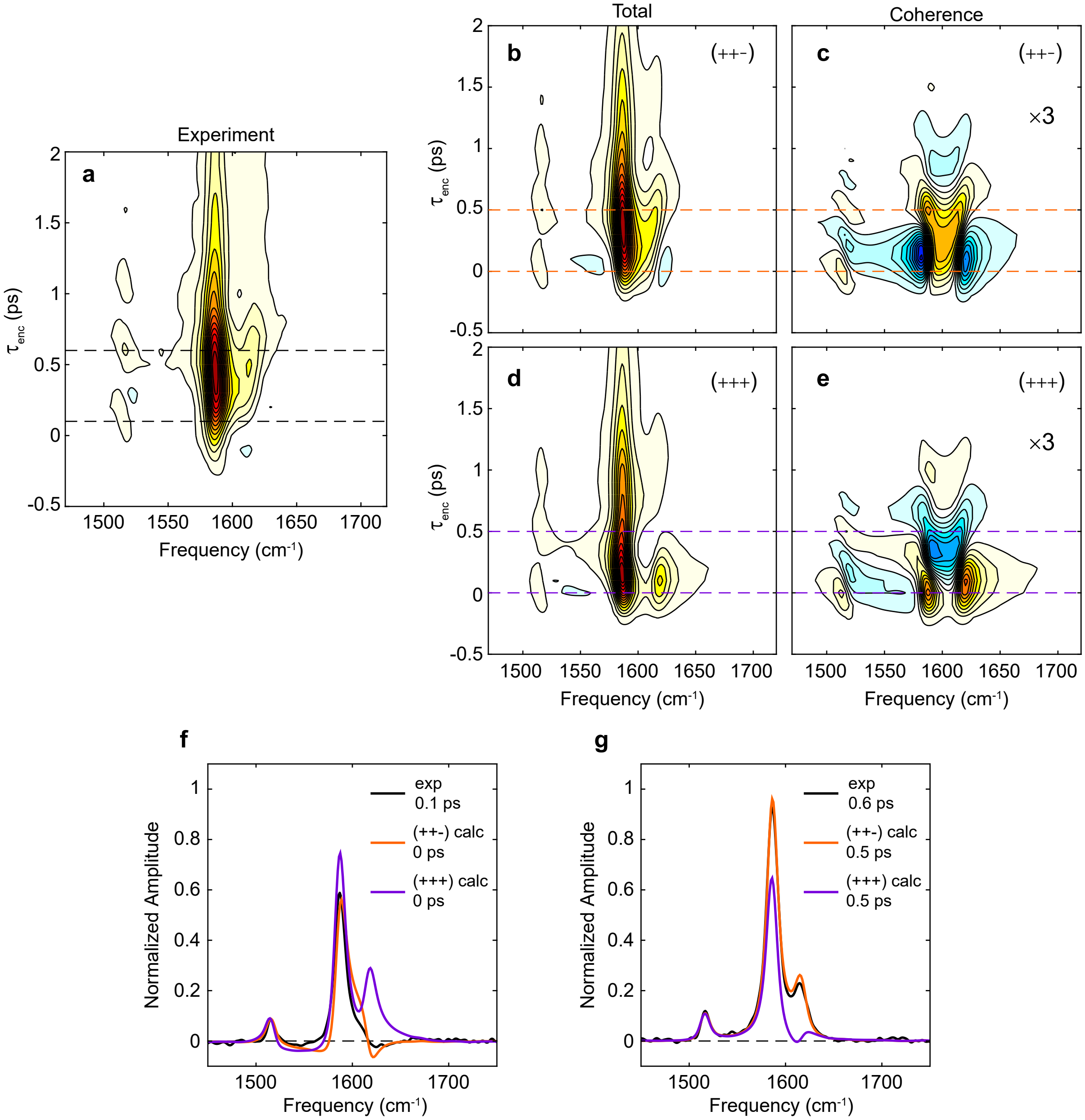

Figure S19: Comparison of simulated τ_{enc}-dependent FEIR spectra of C6 with negative (as in main text Section IV) and positive ν_{R2}-ν_{R1} coherence sign. (a) Experimental τ_{enc}-dependent spectrum. Simulated τ_{enc}-dependent (b) total spectrum and (c) coherence contribution using FC factor signs of $(+,+,-)$ for $(\nu_{\mathrm{R3}},\nu_{\mathrm{R2}},\nu_{\mathrm{R1}})$ (same as main text Section IV). (d) and (e) are analogous to (b) and (c) but with the ν_{R1} sign flipped, yielding FC factor signs of $(+,+,+)$. (f) Comparison of experimental, simulated $(+,+,-)$, and simulated $(+,+,+)$ spectra at $\tau_{\mathrm{enc}} = 0.1$ ps, 0 ps, and 0 ps, respectively. (g) Comparison of experimental, simulated $(+,+,-)$, and simulated $(+,+,+)$ spectra at $\tau_{\mathrm{enc}} = 0.6$ ps, 0.5 ps, and 0.5 ps, respectively. In (a)-(e) contouring is set at 6.7% intervals, and (c) and (e) have been scaled by a factor of 3 for better visualization of the smaller amplitude.

S10 C343 DFT normal modes

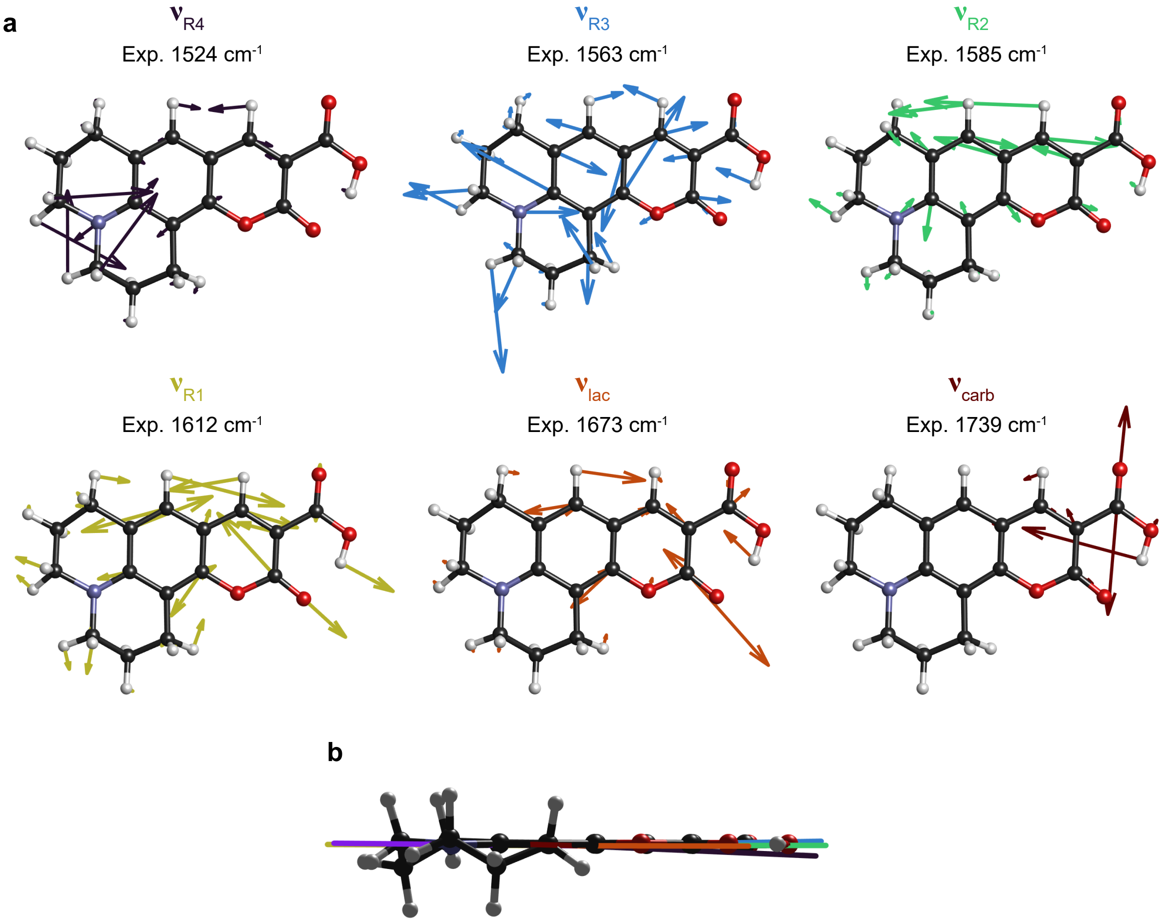

Figure S20: (a) Atomic displacements for the 6 normal modes of C343 used in the calculation of main text Section VB. (b) Transition dipole unit vectors for the 6 normal modes (same color coding) and the electronic transition (purple) viewed with the coumarin core side-on.

Mode	$\langle 0^e \vert 1^g \rangle$ (DFT)	$\langle 0^e \vert 1^g \rangle$ (adjusted)
ν_{R4}	0.0839	0.075
ν_{R3}	0.1156	0.075
ν_{R2}	-0.0309	-0.075
ν_{R1}	-0.0904	-0.085
ν_{lac}	-0.2552	-0.25
ν_{carb}	0.0594	0.06

Table S2: DFT calculated and adjusted values of the FC factors for the 6 modes in the C343 simulation

S11 C343 coherence and population features

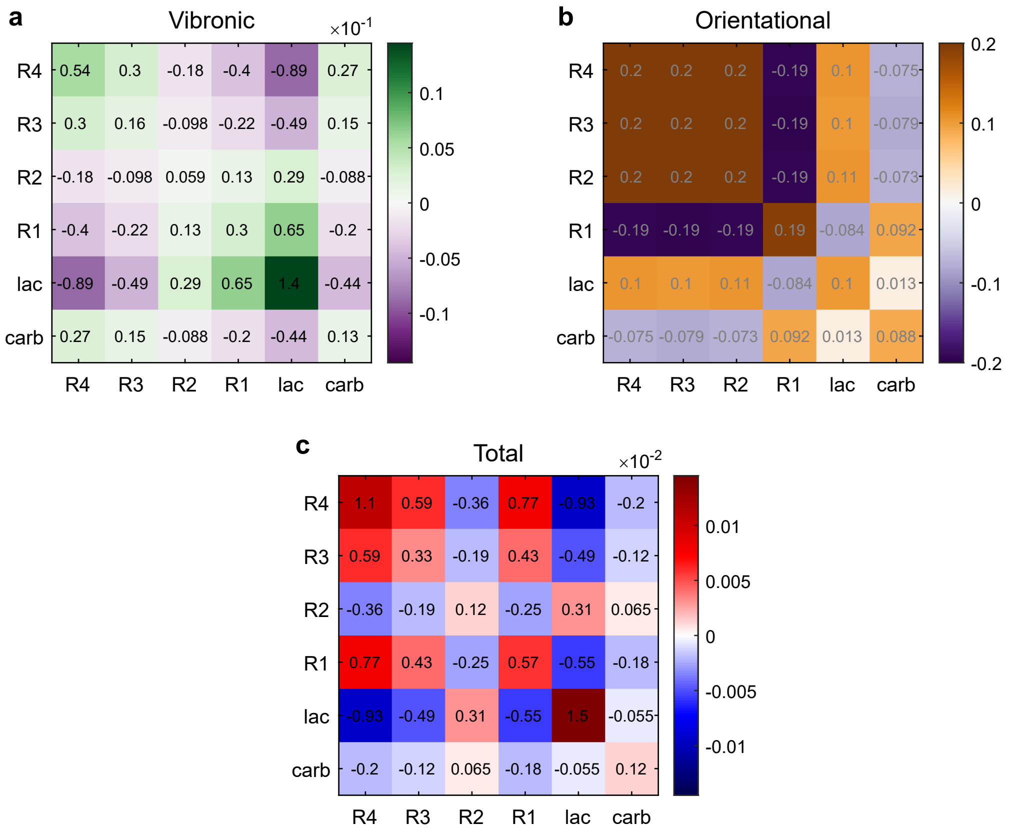

Figure S21: Vibronic and orientational contributions to pathway amplitudes in the C343 response function calculation. Amplitudes are represented on an $n \times n$ grid where $n = 6$ is the number of modes, with the row (i) and column (j) index indicating the modes involved in the first two interactions in each pathway. Population pathways (both interactions with the same mode $i = j$) are on the diagonal, while coherence pathways ($i \neq j$) are off-diagonal. Paired coherence pathways are reflected across the diagonal (exchanging i and j) with identical amplitudes. C_1 and C_2 pathways have identical amplitudes, and we ignore C_3 pathways. (a) The vibronic component $\mu_{i0}\mu_{j0}\langle 0^e|1_i^g\rangle\langle 0^e|1_j^g\rangle$, (b) the orientational component $Y_{ZZZZ}^{\boldsymbol{\sigma\sigma\mu_{j0}\mu_{i0}}}$ (Eq. 32(a) in Paper I) where $\boldsymbol{\sigma}$ is the electronic transition dipole unit vector, and (c) the total amplitude given by their product.

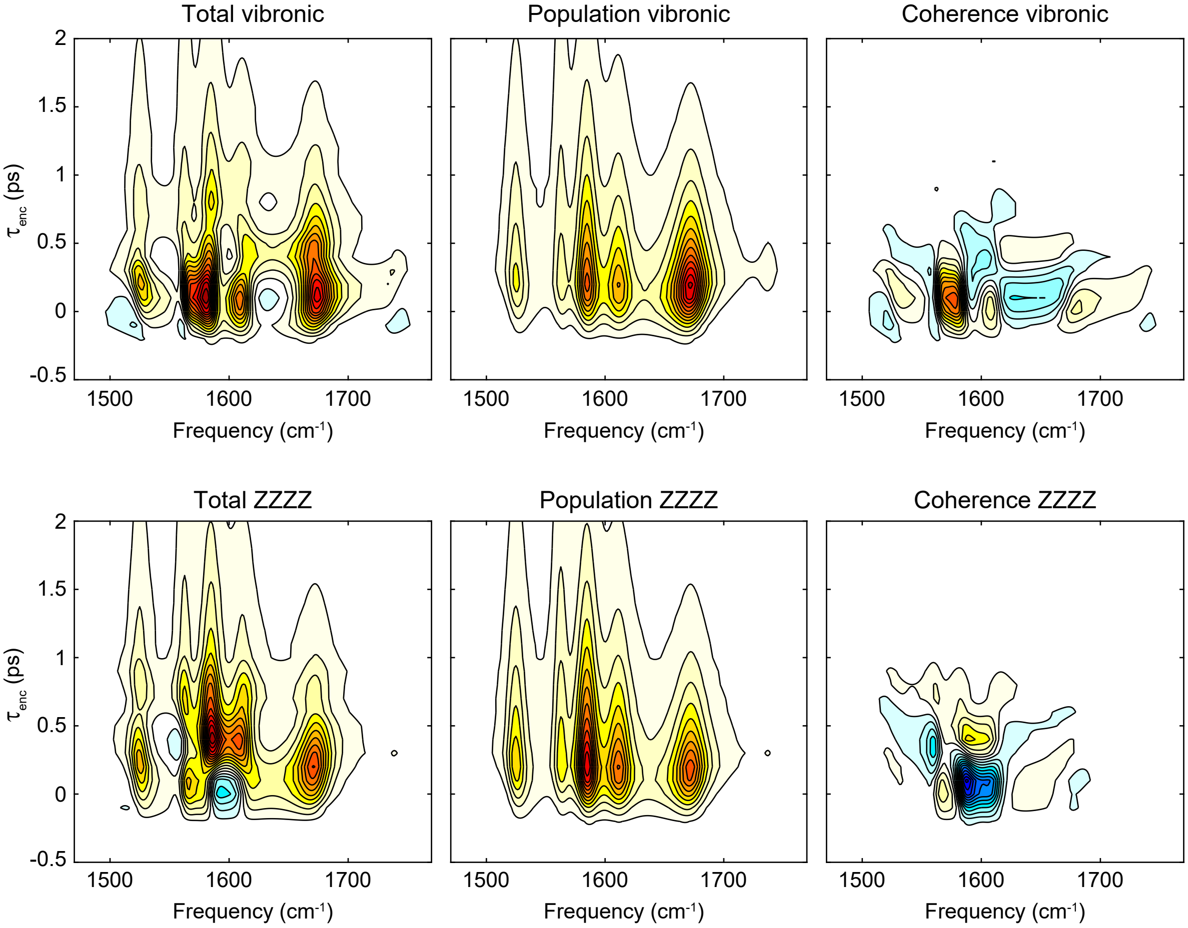

Figure S22: Population and coherence contributions to the calculated vibronic-only (top row) and $ZZZZ$ (bottom row) τ_{enc}-dependent FEIR spectrum of C343. Contouring is set at 5% intervals, and the population and coherence amplitudes add up to the total spectrum amplitude. The coherence contribution is heavily reshaped by the inversion of signs of the coherences involving ν_{R1} produced by the orientational factor evident in Fig. S22(b). The relative intensities of the population features are also re-weighted.

S12 Effect of chirped IR pulses in C6 and C343 simulations.

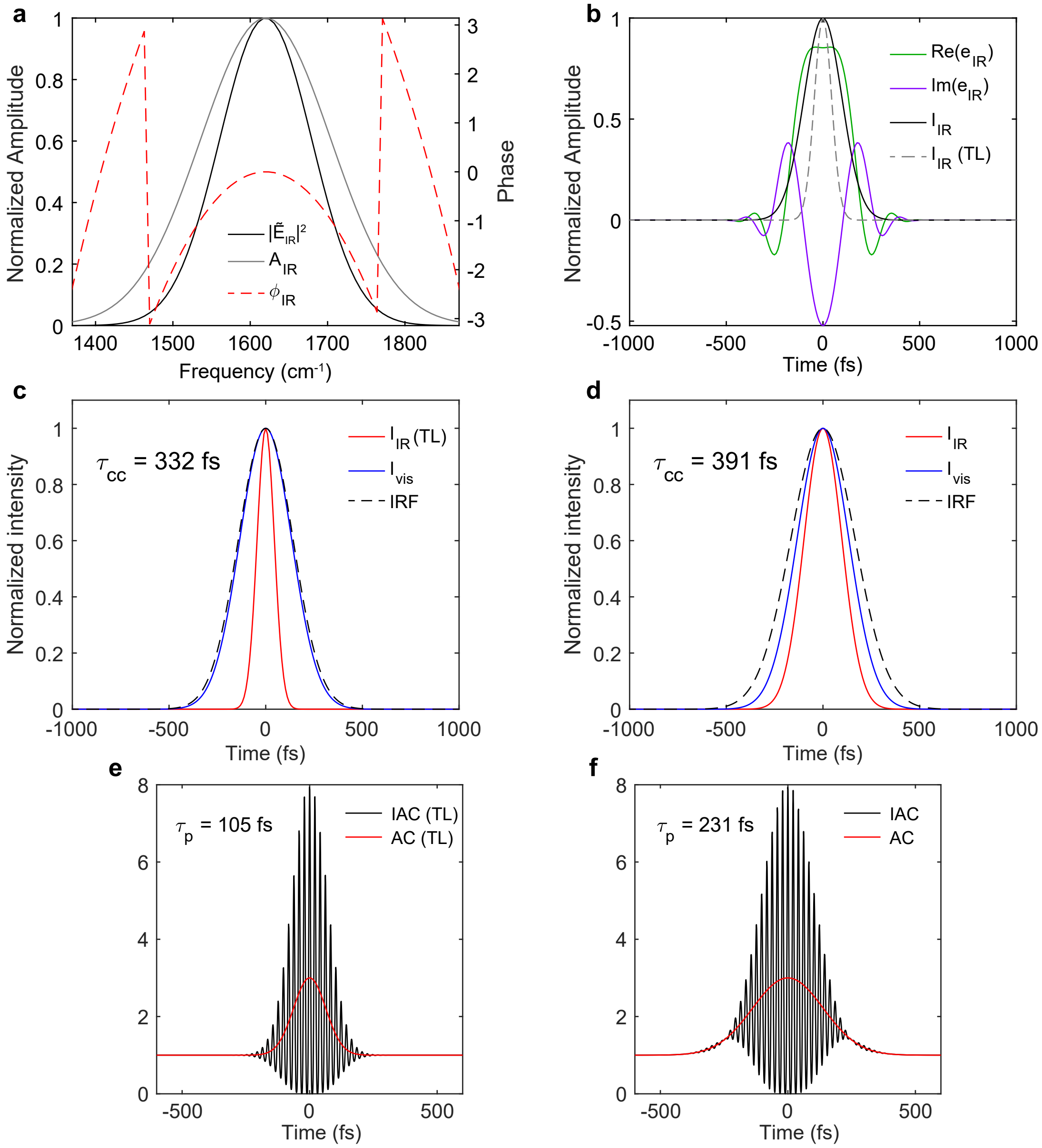

Figure S23: Transform-limited (TL) and chirped IR pulse characteristics used in the response function simulations. (a) Spectrum, spectral amplitude, and spectral phase of the IR pulse (definitions in Sec. S1.2). The phase shown is for the chirped case with γ_2 = -7800 fs^2, while the TL case has a uniform phase of zero. (b) Real (green) and imaginary (purple) parts of the chirped pulse's time-domain envelope $e_{\mathrm{IR}}(t)$, its resulting intensity profile $I_{\mathrm{IR}} = |e_{\mathrm{IR}}(t)|^2$ (black), and the intensity profile in the TL case (dashed grey). (c)-(d) IR and visible intensity profiles and the IRF (IR/Vis intensity cross-correlation) for the TL and chirped cases, respectively. The IRF duration τ_{cc} is indicated, and in both cases the visible pulse remains TL. (e)-(f) IR interferometric autocorrelation (IAC) and intensity autocorrelation (AC) for the TL and chirped cases, respectively. Pulse durations are indicated, which for the chirped case roughly match the experimentally measured duration (cf. Fig. S10(b)).

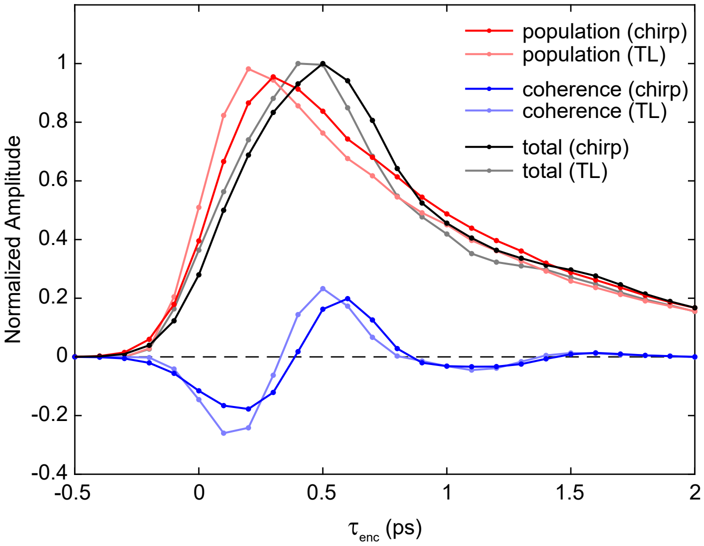

Figure S24: Comparison of calculated two-pulse FEIR signals for C6 using a TL and chirped IR pulse (from Fig. S23). In both cases the total signal (black, population contribution (red), and coherence contribution (blue) are shown. The TL case (same data as main text Fig. 8(b)) is plotted with half-saturated colors, while the chirped IR case uses fully-saturated colors. The peak of the total signal is shifted to longer τ_{enc} by about $\sim$70 fs for the chirped case.

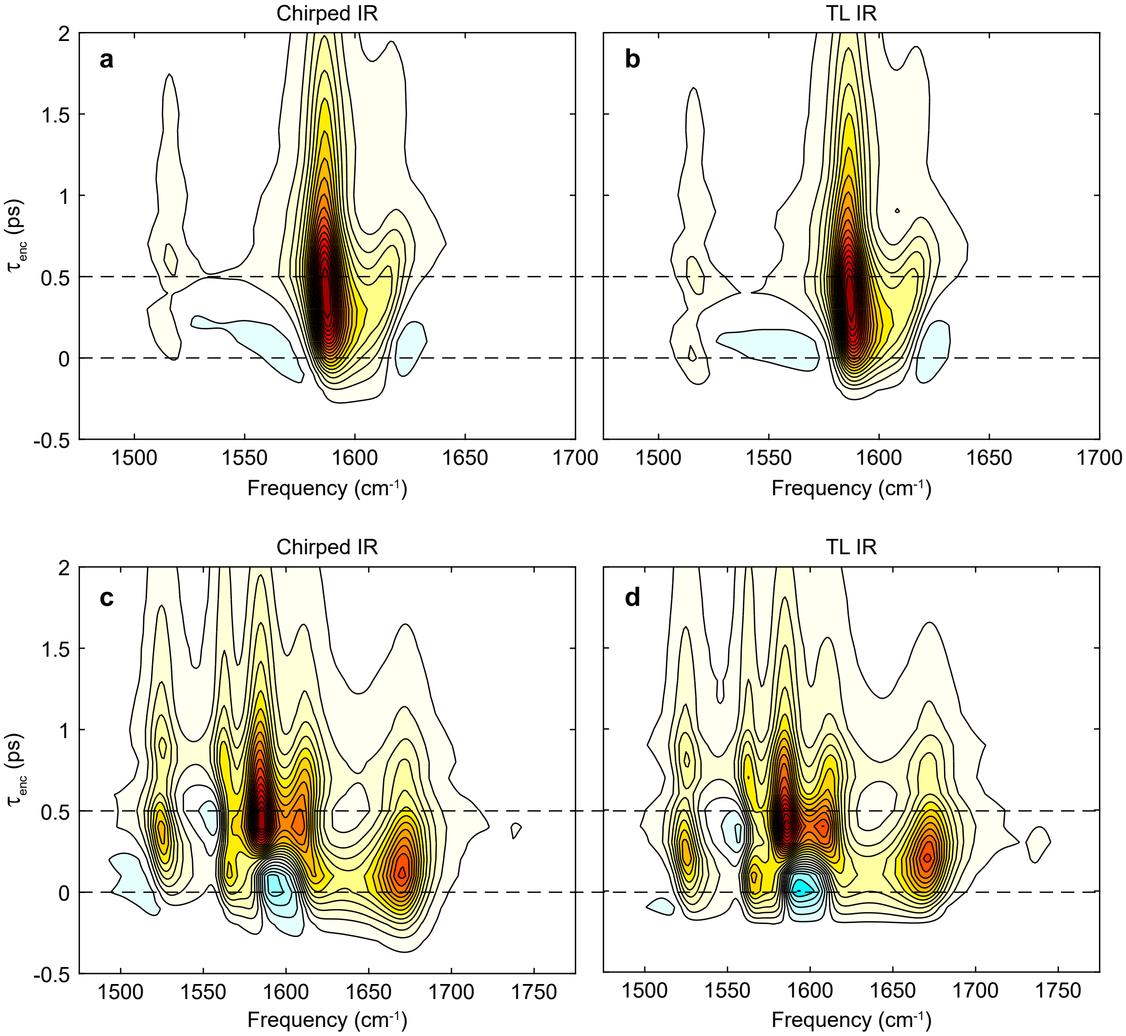

Figure S25: Comparison of calculated τ_{enc}-dependent FEIR spectra with the chirped IR pulses from Fig. S23 (left column) and TL pulses (right column) for C6 (top row) and C343 (bottom row). Dashed lines indicate $\tau_{\mathrm{enc}} = 0$ ps and $\tau_{\mathrm{enc}} = 0.5$ ps to aid in lining up the evolution of various features. Overall, the effect of this dispersion is to delay features on the red side of the pulse spectrum while advancing those on the blue side, creating a "tilted" appearance to the τ_{enc}-dependent spectra. As in the related case of the frequency-resolved TPA signal discussed in Sec. S4, this effect is consistent with the negative sign of $\gamma_{\mathrm{IR},2}$ resulting in a down-chirp where the redder frequencies lag behind the bluer. This "tilting" behavior in the chirped simulations matches well with the experimental spectra in main text Figs. 7(b) and 11(b), but is a rather subtle effect for the magnitude of $\gamma_{\mathrm{IR},2}$ considered.

References

(1) Gallagher Faeder, S. M.; Jonas, D. M. Phase-resolved time-domain nonlinear optical signals. *Phys. Rev. A* **2000**, *62*, 033820, DOI: `10.1103/PhysRevA.62.033820`.

(2) Marshall, A. G.; Verdun, F. R., *Fourier transforms in NMR, optical, and mass spectrometry: a user's handbook*; Elsevier: 1990.

(3) Albrecht, A. W.; Hybl, J. D.; Gallagher Faeder, S. M.; Jonas, D. M. Experimental distinction between phase shifts and time delays: Implications for femtosecond spectroscopy and coherent control of chemical reactions. *J. Chem. Phys.* **1999**, *111*, 10934–10956, DOI: `10.1063/1.480457`.

(4) Shim, S.-H.; Zanni, M. T. How to turn your pump–probe instrument into a multidimensional spectrometer: 2D IR and Vis spectroscopies via pulse shaping. *Phys. Chem. Chem. Phys.* **2009**, *11*, 748–761, DOI: `10.1039/B813817F`.

(5) Diels, J.-C.; Rudolph, W., *Ultrashort Laser Pulse Phenomena*; Elsevier: 2006.

(6) Mandel, L.; Wolf, E., *Optical Coherence and Quantum Optics*; Cambridge university press: 1995.

(7) Boashash, B. Estimating and interpreting the instantaneous frequency of a signal. I. Fundamentals. *Proc. IEEE* **1992**, *80*, 520–538, DOI: `10.1109/5.135376`.

(8) Mandel, L. Complex Representation of Optical Fields in Coherence Theory. *J. Opt. Soc. Am.* **1967**, *57*, 613–617, DOI: `10.1364/JOSA.57.000613`.

(9) Caflisch, R. E. Monte carlo and quasi-monte carlo methods. *Acta numerica* **1998**, *7*, 1–49.

(10) Whaley-Mayda, L. Fluorescence-Encoded Infrared Spectroscopy for Single-Molecule Vibrational Investigation in Solution, phdthesis, University of Chicago, 2022.

(11) DeFlores, L. P.; Nicodemus, R. A.; Tokmakoff, A. Two-dimensional Fourier transform spectroscopy in the pump-probe geometry. *Optics Letters* **2007**, *32*, 2966–2968, DOI: `10.1364/OL.32.002966`.

(12) Helbing, J.; Hamm, P. Compact Implementation of Fourier Transform Two-Dimensional IR Spectroscopy without Phase Ambiguity. *J. Opt. Soc. Am. B* **2011**, *28*, 171–178, DOI: `10.1364/JOSAB.28.000171`.

(13) De Marco, L. The molecular dynamics of hydrogen-bonding explored with broadband two dimensional infrared spectroscopy, phdthesis, MIT, 2016.

(14) Göppert-Mayer, M. Über Elementarakte mit zwei Quantensprüngen. *Annalen der Physik* **1931**, *401*, 273–294, DOI: `https://doi.org/10.1002/andp.19314010303`.

(15) Peticolas, W. L. Multiphoton Spectroscopy. *Annu. Rev. Phys. Chem.* **1967**, *18*, 233–260, DOI: `10.1146/annurev.pc.18.100167.001313`.

(16) Craig, D. P.; Thirunamachandran, T., *Molecular Quantum Electrodynamics: an Introduction to Radiation-Molecule Interactions*; Courier Corporation: 1998.

(17) Schatz, G. C.; Ratner, M. A., *Quantum Mechanics in Chemistry*; Courier Corporation: 2002.

(18) Raymer, M. G.; Landes, T.; Marcus, A. H. Entangled two-photon absorption by atoms and molecules: A quantum optics tutorial. *J. Chem. Phys.* **2021**, *155*, 081501, DOI: `10.1063/5.0049338`.

(19) Weiner, A., *Ultrafast Optics*; Wiley Series in Pure and Applied Optics; Wiley: 2011.

(20) Whaley-Mayda, L.; Guha, A.; Tokmakoff, A. Resonance conditions, detection quality, and single-molecule sensitivity in fluorescence-encoded infrared vibrational spectroscopy. *J. Chem. Phys.* **2022**, *156*, 174202, DOI: `10.1063/5.0088435`.